An efficient multi-layer boundary element method for direct computation of sound propagation in shallow water environments

by

Chengxi Li

Submitted to the Department of Mechanical Engineering
in partial fulfillment of the requirements for the degree of

Doctor of Philosophy in Mechanical Engineering

at the

MASSACHUSETTS INSTITUTE OF TECHNOLOGY

February 2019

Signature redacted

Author .....
Department of Mechanical Engineering
October 17 2018

Signature redacted

Certified by... .....
Yuming Liu
Senior Research Scientist
Thesis Supervisor

Signature redacted

Accepted by ....
Nicolas Hadjiconstantinou
Chairman, Department Committee on Graduate Theses

An efficient multi-layer boundary element method for direct computation of sound propagation in shallow water environments

by

Chengxi Li

Submitted to the Department of Mechanical Engineering
on October 17 2018, in partial fulfillment of the
requirements for the degree of
Doctor of Philosophy in Mechanical Engineering

Abstract

The objective of this thesis is to develop and apply efficient three-dimensional (3D) direct simulation capabilities for underwater sound field predictions in shallow water environments. Despite the large number of theoretical and experimental studies, direct numerical simulation of the shallow water acoustic field is still challenging due to environmental complexities and large computation cost involved.

In this thesis, we develop a highly efficient O(NlogN) multi-layer boundary-element method, PFFT-BEM, for direct numerical simulation of acoustic propagation and scattering in shallow water environment. This method utilizes a Pre-corrected Fast Fourier Transform (PFFT) approach to accelerate the boundary-element method and reduce the computational efforts from O($N^{2\sim3}$) to O(NlogN) where N is the total number of boundary unknowns. PFFT-BEM is capable of accounting for complex topography, inhomogeneity of water properties, and dynamic environments associated with realistic coastal conditions. With the O(NlogN) efficiency and linear scalability on massively parallel high-performance computing platforms, we first conduct multi-layer 3D simulations benchmarking low-mid frequency acoustics over kilometer ranges against available theoretical results and field experiments. We then apply large-scale PFFT-BEM simulations to investigate two underwater acoustics problems which are of scientific interest and practical importance: (1) 3D sound scattering from rough ocean surface; (2) 3D sound propagation and scattering around underwater seamount(s).

For the 3D rough surface scattering problem, several approximation models have been proposed such as the perturbation theory and Kirchhoff approximation. These approximation models provide fast predictions of statistics for the acoustics scattering necessary for predicting the scattering effects and reverberations from the rough surfaces. The validities of these models need to be assessed by direct numerical methods. However, most existing direct numerical studies regarding the validity regions of the approximation models are limited to the 2D rough surface scattering problem.

We apply direct PFFT-BEM computations to study the 3D rough surface scattering problem with a Gaussian roughness spectrum. We examine the accuracy of the approximation model results through comparisons with direct numerical simulation results by 3D PFFT-BEM with a Monte Carlo technique. We identify and quantify the 3D validity regions of the approximation models as a function of the surface roughness and correlation length. We characterize and quantify the importance of 3D scattering effects on the validities of different approximation models. Moreover, we find that both perturbation theory and Kirchhoff approximation become inaccurate for 3D scattering problems with low grazing angles.

For the problem of 3D sound propagation/scattering around underwater seamount(s), we investigate the effects of seamount geometry and sound source frequencies on the sound scatterings by the seamount using 3D PFFT-BEM simulations. In particular, we investigate the backscattering, blocking and 3D scattering effects due to the presence of the seamount. We find that the acoustics scattering effects by the seamount have a strong dependence on the source frequency, and small variations in seamount geometry (such as seamount height and cross section shape) can induce significant changes in the acoustics scattering field.

Thesis Supervisor: Yuming Liu
Title: Senior Research Scientist

Acknowledgments

I would like to gratefully acknowledge the help and support of my advisor Dr. Yuming Liu, whose guidance and insight truly inspired me throughout the past six years to complete this work. He gave me the great opportunities to study various interesting topics in both hydrodynamics and ocean acoustics, and guided me with patient and encouragement. I cannot thank him enough for all his supports and guidance.

Prof. Dick K. P. Yue will always be a role model in my academic career. He is exceptional in mentorship: his way of proposing new problems and motivating you, his way of giving examples and constant passion in solving new challenges provide encouragement and guidance for me through my days in MIT. His insightful suggestions and ideas led me to complete the work presented in this thesis. I would like to express my great gratitude to Prof. Nicholas Makris for giving me valuable advices during my committee meetings and for his excellent teaching in my ocean acoustics class.

I would also like to acknowledge Dr. Bryce Campbell who provided inspiring ideas and guidance. Thanks to all the people outside MIT with whom we collaborated or from whom I received technical and scientific advice and help. I also gratefully acknowledge funding support from the Office of Naval Research (ONR), and Department of Defence High performance computing mordernization program for support, help, and use of equipment. Thanks to all my dear friends in MIT.

Thanks to my family: my parents, my parents-in-law, my wife and my children. Special thanks to my wife, Jieyan Chen, for her incredible supports and sacrifices.

Finally, I would like to leave the remaining space in memory of my beloved grandma, Zebi Zhang, who is now rest in peace in heaven. You will be missed and remain in my heart.

Contents

1 Introduction **23**

1.1 Motivation 23

1.2 Thesis contribution 29

1.3 Thesis organization 30

2 Mathematical formulation and implementation of pre-corrected FFT-accelerated boundary element method for shallow water acoustics **33**

2.1 Formulation of multi-layer boundary element method 34

2.2 Formulation of pre-corrected fast Fouier transform method 38

2.3 Accuracy dependence on numerical parameters 44

2.4 Determination of preconditioner 48

2.5 PFFT-BEM scalability on numbers of processors and unknowns . . . 51

2.6 Concluding remarks 53

3 Numerical validation/benchmark of the PFFT-BEM method **55**

3.1 Comparison with existing analytical and numerical results 56

3.1.1 Pekeris waveguide 56

3.1.2 Acoustical Society of America (ASA) wedge 59

3.1.3 3D Gaussian canyon 64

3.2 Comparison with experimental results 66

3.2.1 Prediction of 4D sound scattering by traveling internal waves . 66

3.2.2 Prediction of 3D sound scattering in the mouth of the Columbia river 70

3.3 Concluding remarks 78

4 Study on the 3D scattering by rough surface 81

4.1 Introduction 82

4.2 Mathematical formulations 84

4.2.1 Boundary-value problem for plane wave scattering 84

4.2.2 Incident wave field 86

4.2.3 Scattering strength 87

4.2.4 Random surface generation 87

4.3 Approximate models 89

4.3.1 Kirchhoff approximation 89

4.3.2 Perturbation theory 91

4.4 Results and discussions 92

4.4.1 Test for convergence of domain size 94

4.4.2 Comparison with 2D direct numerical simulation results . . . 94

4.4.3 The validity regions of 3D perturbation theory and Kirchhoff approximation 96

4.4.4 Comparison between 2D and 3D validity regions 102

4.4.5 Effects of low grazing angles 107

4.5 Concluding remarks 111

5 Study on 3D sound field around underwater seamount 113

5.1 Validation against coupled mode method 115

5.2 Effects of seamount geometries on acoustic scatterings 116

5.2.1 Seamount height 118

5.2.2 Seamount cross section shape 122

5.3 Difference between low frequency and higher frequency scattering by the underwater seamount 129

5.4 Seamounts with realistic environment/geometry 132

5.4.1 Prediction of 3D (spatial) sound scattering due to presence of a seamount in New Jersey continental shelf 132

5.4.2 Prediction of 3D (spatial) sound scattering due to double seamount 134
5.5 Concluding remarks 139

6 Conclusion and future works **141**
6.1 Conclusion 141
6.2 Future works 143

List of Figures

2-1 Schematic of multi-layer model with a total number $I = 3$ layers. . . . 35

2-2 Geometry of the Pekeris waveguides [Jensen et al., 2011]: a $20Hz$ point source is located at z=36m. The depth of the upper water column $H = 100m$ with an infinite depth in the bottom layer. The water column has a density $\rho_1 = 1g/cm^3$ and sound speed $c_1 = 1500m/s$ while $\rho_2 = 1.8g/cm^3$ and $c_2 = 1800m/s$ in the bottom layer 45

2-3 (a) Normalized average interpolation errors ϵ between PFFT-BEM and conventional BEM on different surfaces as a function of d/h. (b) Comparison of operation count per iteration step of PFFT-BEM using linear (β=1) and quadratic (β=2) interpolation function as a function of N. 47

2-4 Normalized average $\epsilon_{average}$ and maximum ϵ_{max} errors of the pressure at $z = 46m$ of the Pekeris waveguide obtained using the PFFT-BEM as a function of $\lambda/\Delta l$. The slopes κ are approximately equals to -2 for both the maximum and averaged errors shown. 48

2-5 GMRES residual [Saad and Schultz, 1986] as a function of iteration number for the (a) Pekeris waveguide problem with size of $1km \times 1km \times 100m$, (b) Pekeris waveguide problem with size of $25km \times 15km \times 100m$. The results are obtained: without a preconditoner, with Jacobian diagonal preconditioner and MN precondtioner with neighboring meshes $N_m = 2, 4$. 50

2-6 CPU scaling for the Pekeris waveguide and fixed $N = 7 \times 10^6$, with increasing processors counts, using PFFT-BEM. 51

2-7 (a) Comparison of memory requirement of PFFT-BEM method (slope $\kappa \sim 1$) and conventional BEM (slope $\kappa \sim 2$) as a function of N. (b) Comparison of operation count per iteration step of PFFT-BEM method (slope $\kappa \sim 1$) and conventional BEM (slope $\kappa \sim 2$) as a function of N. 52

3-1 (a) Tranmission Loss (TL) at $z = 46m$ for $20Hz$ point source at 36m depth in the Pekeris waveguide: comparison between theoretical predictions[Jensen et al., 2011] and PFFT-BEM. (b) Contours of transmission loss vs. depth and range for $20Hz$ point source at $36m$ depth in the Pekeris waveguide 57

3-2 Shallow water summer sound profile with a gradient region at 20m$\sim$40m. 58

3-3 Tranmission Loss (TL) at z=70m for 60 Hz point source at 70m depth in the Pekeris waveguide with summer sound profile: comparison among PFFT-BEM results with different number of layers. 58

3-4 Geometry of the underwater ASA wedge, slope angle $\pi/63$. A 25Hz point source is located at (x,y,z)=(0,0,100m). The wedge meets the free surface (z=0) at y=-4000m. 60

3-5 (a) TL along the $x-$axis at $z = 30m$ for ASA wedge: comparison between theoretical predictions by Deane and Buckingham [1993] and 3D direct simulations by PFFT. (b) TL obtained using PFFT-BEM on the $x - y$ plane at $z = 30m$. Case 1: source frequency $f = 25Hz$ with two water layers and both having the same density, $\rho = 1g/cm^3$, but different sound speeds, $c_1 = 1500m/s$, $c_2 = 1700m/s$. The bottom layer has a medium attenuation $\alpha = 0.5dB/\lambda$. 61

3-6 (a) TL along the $x-$axis at $z = 30m$ for ASA wedge: comparison between theoretical predictions by Deane and Buckingham [1993] and 3D direct simulations by PFFT. (b) TL obtained using PFFT-BEM on the $x - y$ plane at $z = 30m$. Case 1: source frequency $f = 25Hz$with upper water layer having $\rho_1 = 1g/cm^3$, $c_1 = 1500m/s$, on top of a soil bottom with $\rho_2 = 1.5g/cm^3$, $c_2 = 1700m/s$. The bottom layer has a medium attenuation $\alpha = 0.5dB/\lambda$. 62

3-7 TL along the $x-$axis at $z = 30m$ for ASA wedge: comparison between theoretical predictions by Deane and Buckingham [1993] and 3D direct simulations by PFFT. (b) TL obtained using PFFT-BEM on the $x-y$ plane at $z = 30m$. Case 3: source frequency $f = 75Hz$ with upper water layer having $\rho_1 = 1g/cm^3$, $c_1 = 1500m/s$, on top of a soil bottom with $\rho_2 = 1.5g/cm^3$, $c_2 = 1700m/s$ and a medium attenuation $\alpha = 0.5dB/\lambda$. 63

3-8 The geometry of the Gaussian canyon used in the present study with upper water layer having $\rho_1 = 1g/cm^3$, $c_1 = 1500m/s$, on top of a soil bottom with $\rho_2 = 1.5g/cm^3$, $c_2 = 1700m/s$ and a medium attenuation $\alpha = 0.5dB/\lambda$. 64

3-9 (a) TL along the $y-$axis at $z = 35m$ for Gaussian canyon: comparison between longitudinal invariant FEM predictions [Isakson et al., 2014] and 3D direct simulations by PFFT-BEM. (b) TL obtained using PFFT-BEM on the $x - y$ plane at $z = 30m$. 65

3-10 (a) Field experiment arrangement of the source/receiver and their relative position with respect to the internal wave fronts [Badiey et al., 2005] (b) Parameters of PFFT-BEM simulation (oblique sea condition): upper water layer with ρ_1=$1.024g/cm^3$, c_1=$1530m/s$, lower water layer with ρ_2=$1.0257g/cm^3$, c_2=$1480m/s$ and the bottom layer with ρ_b=$1.8g/cm^3$, c_b=$1750m/s$ and α=0.4375dB/λ 67

3-11 TL in the horizontal plane at receiver depth $z = 45m$ obtained by 4D PFFT-BEM direct numerical simulation with (a) t=0 (b) t=1/4T_{int} (c) t=1/2T_{int} (d)3/4T_{int} 68

3-12 (a) Field normalized acoustics pressure data [Badiey et al., 2005] with source $f = 30 \sim 160Hz$ and irregular internal waves. (b) Normalized acoustics pressure predicted by 4D PFFT-BEM with sound frequency $f = 60Hz$ and regular internal wave with amplitude η as $\eta = 10sech^2[(y - c_{int}t)/70]$, where c_{int} is the internal wave phase velocity equals to 0.65 m/s [Badiey et al., 2005] 69

3-13 (a) Mouth of the Columbia River: station S2 where the acousitc source was placed, and station A5 where the receiver was placed 1m above the riverbed. The acoustics transect was 1.36km long [Reeder, 2016]. (b) A sketch of the side view of the flood tide (salt wedge) entrance the fresh water and the wave generated by the interaction between the fresh water and flood tide. 72

3-14 (a) The sound speed (m/s) vs depth at time (Z) at receiver during the 6h period of the acoustic transmission [Reeder, 2016]. (b)The SEL measure at the receiver during the flood period [Reeder, 2016]. . . . 73

3-15 PFFT-BEM prediction of the transmission loss using 500Hz frequency and realistic geometry and acoustic environment: (a) Fresh water case, c_1=1460m/s, c_b=1620m/s and α=0.365dB/m in the bottom. (b) Salt wedge only, c_1=1460m/s, c_2=1470m/s, c_3=1490m/s, c_b=1620m/s and α=0.365dB/m in the bottom. (c) Salt wedge and free surface waves with amplitude A=4m, c_1=1460m/s, c_2=1470m/s, c_3=1490m/s, c_b=1620m/s and α=0.365dB/m. 74

3-16 PFFT-BEM prediction of the transmission loss using 500Hz frequency and realistic geometry and acoustic environment with different surface wave phases relative to the sound source: (a) Calm water with salt wedge A=0, c_1=1460m/s, c_b=1620m/s and α=0.365dB/m in the bottom. (b) Salt wedge with head sea surface wave amplitude A=4m, sound source located under the surface wave crest with c_1=1460m/s, c_2=1470m/s, c_3=1490m/s, c_b=1620m/s and α=0.365dB/m in the bottom. (c) Salt wedge with head sea surfacewave amplitude A=4m, sound source located under the surface wave zero crossing. (d) Salt wedge with head sea surface wave amplitude A=4m, sound source located under the surface wave trough. 75

3-17 PFFT-BEM prediction of the transmission loss using 500Hz frequency and realistic geometry and acoustic environment with different surface wave phases relative to the sound source: (a) Calm water with salt wedge A=0, c_1=1460m/s, c_b=1620m/s and α=0.365dB/m in the bottom. (b) Salt wedge with beam sea surface wave amplitude A=4m, sound source located under the surface wave crest with c_1=1460m/s, c_2=1470m/s, c_3=1490m/s, c_b=1620m/s and α=0.365dB/m in the bottom. (c) Salt wedge with beam sea surface wave amplitude A=4m, sound source located under the surface wave zero crossing. (d) Salt wedge with beam sea surface wave amplitude A=4m, sound source located under the surface wave trough. 76

4-1 Surface realization with vertical exaggeration where kl=5.6, kh=0.52 (a) Surface shape in xz plane (b) 3D surface. 88

4-2 SS comparison for different domain size L using 3D direct numerical simulation by PFFT-BEM. The incident wave grazing angle $\theta_g = 45°$, the surface parameter is chosen to be $kh = 0.52$, $kl = 2.6$. Here k and λ are the acoustics wavenumber and wavelength. 93

4-3 (a) Locations of the numerical examples (b-d) in the kh-kl plane , the 2-D validity regions (1-dB error) for the first-order perturbation theory, second-order perturbation theory and the Kirchhoff approximation. The incident wave grazing angle $\theta_g = 45°$. (b) Comparison of the SS obtained by 2D direct numerical simulation using PFFT-BEM with 2D direct numerical simulation by Kaczkowski et al. [1994] and first-order perturbation theory ($kh = 0.38$, $kl = 1.4$). (c) Comparison of the SS obtained by 2D direct numerical simulation using PFFT-BEM with 2D direct numerical simulation by Kaczkowski et al. [1994] and second-order perturbation theory ($kh = 0.52$, $kl = 2.6$). (d) Comparison of the SS obtained by 2D direct numerical simulation using PFFT-BEM with 2D direct numerical simulation by Kaczkowski et al. [1994] and Kirchhoff approximation results ($kh = 10.0$, $kl = 1.03$). 95

4-4 The 3D validity regions (1-dB error) for the first-order perturbation theory ($\sigma^{(2)}$). These regions are valid for θ_g=45°. The black dots represent the locations of the numerical examples (a)-(d) shown in Fig.4-5. 97

4-5 Comparison of the SS obtained by 3D direct numerical simulation using PFFT-BEM with 3D first order perturbation theory with (a) $kh = 0.3$, $kl = 2.0$ (b) $kh = 0.55$, $kl = 2.0$ (c) $kh = 0.85$, $kl = 2.0$ (d) $kh = 1.3$, $kl = 2.0$, here θ_g=45°. 98

4-6 The 3D validity regions (1-dB error) for the first (lower line) and second order perturbation theory (upper line). These regions are validity for θ_g= 45°. The black dots represent the locations of the numerical examples (a)-(d) shown in Fig.4-7. 99

4-7 Comparison of the SS obtained by 3D direct numerical simulation using 3D PFFT-BEM with 3D first-order and second-order perturbation theory with (a) $kh = 0.52$, $kl = 2.6$ (b) $kh = 0.65$, $kl = 2.6$ (c) $kh = 0.85$, $kl = 2.6$ (d) $kh = 1.3$, $kl = 2.6$, here θ_g=45°. 100

4-8 Comparison of the SS obtained by 3D direct numerical simulation using 3D PFFT-BEM with Kirchhoff approximation with (a) $kh = 1.33$, $kl = 20$ (b) $kh = 1.33$, $kl = 15$ (c) $kh = 1.33$, $kl = 10$ (d) $kh = 1.33$, $kl = 5.6$, here θ_g=45°. 101

4-9 The 3D validity regions (1-dB error near the specular direction) for Kirchhoff approximation. These regions are valid for θ_g=45°. The black dots represent the locations of the numerical examples (a)-(d) shown in Fig.4-8. 102

4-10 Comparison between the 2D and 3D validity regions (1-dB error) for the first-order perturbation theory ($\sigma^{(2)}$), second-order perturbation theory ($\sigma^{(4)}$) and the Kirchhoff approximation. These regions are valid for θ_g=45°. 105

4-11 Comparison of the $\sigma^{(2)}$ 1-dB error curve obtained by 3D direct numerical simulation using 3D PFFT-BEM and asymptotic analysis with $kl >> 1$ and $kl << 1$, here θ_g=45°. 106

4-12 Comparison of the SS obtained by 3D direct numerical simulation using 3D PFFT-BEM with Kirchhoff approximation ($kh = 1.03$, $kl = 10.0$), here θ_g=45°. 106

4-13 Comparison of the SS obtained by 3D direct numerical simulation using 3D PFFT-BEM with 3D first-order, second-order perturbation theory and Kirchhoff approximation with $kh = 0.55$, $kl = 2.0$, here $\theta_g = 10°$. 107

4-14 Comparison of the SS obtained by 3D direct numerical simulation using 3D PFFT-BEM with 3D first-order, second-order perturbation theory and Kirchhoff approximation with $kh = 0.65$, $kl = 2.6$, here $\theta_g = 10°$. 108

4-15 Comparison of the SS obtained by 3D direct numerical simulation using 3D PFFT-BEM with 3D first-order, second-order perturbation theory and Kirchhoff approximation with $kh = 1.33$, $kl = 15.0$, here $\theta_g = 10°$. 109

4-16 SS in the backscattering direction with different grazing angle θ_g (down to 2.5°) with (a) kl=2.6, kh=0.65 and (b) kl=15, kh=1.33. 110

5-1 Geometry of the waveguide with a conical seamount and a penetrable bottom, seamount height 250m, seamount radius 350m. A 40Hz point source is located at $(x, y, z) = (0, 0, 100m)$ and 800m away from the seamount center. 116

5-2 (a) TL comparison at different $x-$locations with $(y, z) = (0, 100m)$ for 3D underwater seamount with $f = 40Hz$ between coupled mode method [Luo and Schmidt, 2009] (red line) and 3D direct simulations by PFFT-BEM with 8 elements per wavelength (blue line) and 12 elements per wavelength (green line); TL at different $x-$locations with $(y, z) = (400m, 100m)$ by PFFT-BEM with 12 elements per wavelength (black line); the green and blue line overlap with each other in the figure. (b) TL obtained using PFFT-BEM on the $x - y$ plane at $z = 100m$. . . 117

5-3 TL comparison at different $x-$locations with $(y, z) = (0, 100m)$ for 3D underwater seamount with $f = 40Hz$ with H_0=50m, 100m and 150m. 119

5-4 TL (as a function of distance from the source) in the direction which is tangential to the seamount cross section: comparison between 3D obtained using 3D direct simulations by PFFT-BEM and 2D approximations (left column) and TL at $x - y$ plane (z=100m) obtained using 3D direct simulations by PFFT-BEM for 3D underwater seamount with $f = 40Hz$ with (a)H_0=50m (b) H_0=100m (c) H_0=150m (right column). 120

5-5 $\mathrm{TL}_D(=\mathrm{TL}_{seamount}\text{-}\mathrm{TL}_{background})$ at $x-y$ plane (z=100m) obtained using 3D direct simulations by PFFT-BEM for 3D underwater seamount with $f = 40Hz$ with (a)H_0=50m (b) H_0=100m (c) H_0=150m. 121

5-6 TL at different $x-$locations with $(y, z) = (0, 100m)$ for 3D underwater seamount obtained using 3D direct simulations by PFFT-BEM. Here, $f = 40Hz$ with seamount cross section are circle, ellipse with a=0.875, ellipse with a=0.7 and ellipse with a=1.167. R_y is fixed at 350m. . . 123

5-7 Seamount cross section shape at seamount bottom (left column) and TL at $x-y$ plane (z=100m) obtained using 3D direct simulations by PFFT-BEM (right column). Here, $f = 40Hz$ with seamount cross section are (a) circle, (b) ellipse with a=0.875, (c) ellipse with a=0.7 and (d) ellipse with a=1.167. R_y is fixed at 350m. 124

5-8 TL_D(=$\mathrm{TL}_{seamount}$-$\mathrm{TL}_{background}$) at $x-y$ plane (z=100m) obtained using 3D direct simulations by PFFT-BEM. Here, $f = 40Hz$ with seamount cross section are (a) circle, (b) ellipse with a=0.875, (c) ellipse with a=0.7 and (d) ellipse with a=1.167. R_y is fixed at 350m. 125

5-9 (a) TL at different $x-$locations with $(y, z) = (0, 100m)$ for 3D underwater seamount obtained using 3D direct simulations by PFFT-BEM. (b) TL at different $y-$locations with $(x, z) = (800m, 100m)$ for 3D underwater seamount obtained using 3D direct simulations by PFFT-BEM for $f = 40Hz$. Here, $f = 40Hz$ with seamount cross section are circle, ellipse with a=0.875, ellipse with a=0.7 and ellipse with a=1.167. R_x is fixed at 350m. 126

5-10 Seamount cross section shape at seamount bottom (left column) and TL at $x-y$ plane (z=100m) obtained using 3D direct simulations by PFFT-BEM (right column). Here, $f = 40Hz$ with seamount cross section are (a) circle, (b) ellipse with a=0.875, (c) ellipse with a=0.7 and (d) ellipse with a=1.167. R_x is fixed at 350m. 127

5-11 TL_D(=$\mathrm{TL}_{seamount}$-$\mathrm{TL}_{background}$) at $x-y$ plane (z=100m) obtained using 3D direct simulations by PFFT-BEM. Here, $f = 40Hz$ with seamount cross section are (a) circle, (b) ellipse with a=0.875, (c) ellipse with a=0.7 and (d) ellipse with a=1.167. R_x is fixed at 350m. 128

5-12 (a) TL at different $x-$locations with $(y, z) = (0, 100m)$ for 3D underwater seamount obtained using 3D direct simulations by PFFT-BEM for $f = 400Hz$ and $f = 40Hz$. (b) TL at different $y-$locations with $(x, z) = (800m, 100m)$ for 3D underwater seamount obtained using 3D direct simulations by PFFT-BEM for $f = 400Hz$ and $f = 40Hz$. . . . 130

5-13 (a) TL obtained using PFFT-BEM on the $x-y$ plane at $z = 100m$. (b) TL obtained using PFFT-BEM on the $x-y$ plane at $z = 145m$. (c) TL obtained using PFFT-BEM on the $x-y$ plane at $z = 200m$. (d) TL obtained using PFFT-BEM on the $x-y$ plane at $z = 245m$. ($f = 400Hz$) 131

5-14 The sound speed distribution and bathymetry on the slope of the New Jersey Shelf 133

5-15 TL comparison at different x—locations with $(y, z) = (0, 290m)$ for 3D underwater seamount with seamount and without seamount. 134

5-16 TL obtained using 3D PFFT-BEM on the $x-z$ plane at $y = 0m$ (a)without seamount and (b) with seamount (seamount base at $z = 340m$) (c) Differences between TL's obtained with and without seamount.135

5-17 The double seamount geometry: The tip of the first seamount is at $(x, y, z) = (3500m, 1000m, 200m)$. The tip of the second seamount is at $(x, y, z) = (3500m, -1500m, 200m)$. The slope of both seamounts is 1/4. The radius of both seamounts are 2500 m. The water depth away from the seamount is 825 m. 136

5-18 TL on the $x-y$ plane at $z = 400m$ obtained using (a) 3D PFFT-BEM (b) PE method with fixed arc-length scheme (c) PE method with cylindrical coordinate system (d) PE method with fixed radius-length scheme. 137

5-19 TL of the scattering pressure on the $x-y$ plane with source located at 400m (a) at z=200m, (b) at z=400m, (c) at z=600m, (d) at z=800m.138

List of Tables

3.1 Computational time for validation/benchmark casses 79

Chapter 1

Introduction

1.1 Motivation

Prediction of 3D underwater sound field in range-dependent shallow water environments is a challenging research area due to the complexities associated with the domain geometry and water environments. Over the years, a number theoretical models have been proposed. Notable among these are the ray tracing model, the coupled mode model and the parabolic equation(PE) model. Ray tracing models have been used to study underwater acoustic propagation problems [Jones et al., 1986, Dushaw and Colosi, 1998, Porter, 2011], which are generally not valid for low-mid frequencies because of the underlying high-frequency assumption. In addition, as pointed out by Jensen et al. [2011], 3D ray tracing model are not widely than the two-dimensional (2D) versions due to the high computational cost.

The coupled mode method has been used successfully in 3D for specialized geometries, such as an axisymmetric seamount [Luo and Schmidt, 2009]. When environmental properties are invariant along a spatial coordinate, the 2D coupled mode method could be combined with a wavenumber integration method to obtain 3D acoustic fields [Schmidt, 1988, Shmelev et al., 2014]. For slowly varying spatial environments in two directions, a simplified coupled mode model, the adiabatic-mode model, has been applied in various studies (e.g. Badiey et al. [2005], Ballard [2012], Lynch et al. [2010]). For general 3D geometries, a fully coupled mode propagation model is still

impractical due to the large computing power and memory requirement [Jensen et al., 2011].

A popular class of propagation models are based on the one-way parabolic equation (PE) approximation [Tapperter, 1977]. For 3D applications, a number of PE models have been developed (e.g. Lin et al. [2012, 2013], Sturm [2005]) for problems where backscattering is not significant. Models that include two-way scattering have been developed in general 2D [Collins and Evans, 1992, Lingevitch et al., 2002], and for 3D formulated in cylindrical coordinates [Zhu and Bjørnø, 2000] valid within a limited area. Hybrid normal mode/PE method (e.g. Ballard et al. [2015]) has been developed to account for outgoing mode-coupling and horizontal refraction effects but is valid only when backscattering and modal coupling in the azimuthal direction are weak. Xu et al. [2016] provides a survey of PE approximations highlighting the general limitations for complex 3D problems.

Since the continued increase in computational power over the past several decades, there has been a rise in the number of direct computational investigations of shallow water acoustics which directly solve the wave equation. These techniques typically implement either the finite difference method (FDM), finite element method (FEM), finite volume method (FVM), spectral element method (SEM) or boundary element method (BEM). A review of the different direct numerical methods used in shallow water acoustics can be found in Jensen et al. [2011]. Most of these methods provide satisfactory solutions for 2D (range and depth) problems (e.g.Grilli et al. [1998], Santiago and Wrobel [2000], Pereira et al. [2010], Vendhan et al. [2010], Cristini and Komatitsch [2012], Bottero et al. [2016]). A longitudinally-invariant FEM has also been proposed recently [Isakson et al., 2014]. This method can provide a 3D sound field with the constraint that the geometry of environments must be constant along one of the three spatial coordinates. Despite the continued development of computing capabilities, preforming 3D simulations of ocean acoustics in realistic environments still remains a challenge due to the high computational costs. A 3D SEM is recently developed at low frequency [Xie et al., 2016]. However, when higher frequencies or larger computational domains are involved, 2D simulations still remain as only

option [Cristini and Komatitsch, 2012, Bottero et al., 2016]. This is due to the need for FEM/FVM/SEM to use fine meshes over the entire volume of the computational domain.

In boundary element method (BEM), the Helmholtz boundary-value problem for homogeneous medium can be formulated as a boundary integral equation (BIE) [Burton and Miller, 1971], for which the unknown pressure or the normal pressure gradient on the domain boundaries are solved for. After discretizing the boundary into piecewise elements and approximating the variables over these boundary elements, we obtain a system of linear algebraic equations of the form: $[A]\{x\} = \{b\}$, where $[A]$ is a dense $N \times N$ influence coefficient matrix, $\{x\}$ is the vector of N unknown pressures or/and normal pressure gradient on the boundary, $\{b\}$ is the vector of N known quantities and N the total number of unknowns. Since only the domain boundary is discretized, BEM has an advantage over the volume methods (FDM, FEM, SEM and FVM) which require meshing the entire volume of the computational domain. A number of 2D or 2.5D (longitudinally-invariant) BEM shallow water waveguide acoustic models exist (e.g. Grilli et al. [1998], Godinho et al. [2001], Santiago and Wrobel [2000], Pereira et al. [2010]), and efficient models have been applied to solve 3D acoustical radiation and scattering problem from rigid bodies (e.g.Keuchel et al. [2017], Yan and Gao [2013], Qu et al. [2017], Li et al. [2018]).

In this work, we implement a direct solution of the 3D acoustic problem for range-dependent shallow-water environments with complex boundaries using BEM. To account for inhomogeneity of the medium properties, we develop a multi-domain (multi-layer) approach [Pereira et al., 2010] where homogeneous properties is assumed within each sub-domain. The overall solution is obtained by imposing continuity of pressure and normal pressure gradient at the interfaces of the sub-domains. While BEM can handle complex boundaries and domain interfaces, its major drawback is the computation cost associated with the solution system involving dense influence matrices. Existing approaches use (direct or) iterative solvers [Xue et al., 2001, Li and Liu, 2015] which requires $O(N^2)$ operations to construct the influence matrix $[A]$ and ($O(N^3)$ or) $O(N^2)$ operations for the solution $\{x\}$. The major development here is the

adaptation of a Pre-corrected Fast Fourier Transform (PFFT) approach to reduce the overall computational effort from $O(N^{2\sim3})$ to $O(N \log N)$. PFFT has been applied to boundary-value problems using BEM in the field of electrostatic analysis [Phillips and White, 1997, Masters and Ye, 2004], elastodynamics [Yan et al., 2010a, Xiao et al., 2012], solid mechanics [Yan et al., 2010b], Hydrodynamics [Yan and Liu, 2011, Li and Liu, 2018] and rigid body acoustics scattering problem [Yan and Gao, 2013]. Because of the properties of the method, PFFT accelerated BEM (PFFT-BEM) is particularly suitable for massive parallelization [Yan and Liu, 2011], which we develop and implement on modern high-performance computing (HPC) platforms.

Due to this method solves the Helmholtz equation exactly (up to the discretization error), it can solve the shallow water acoustics problems with low-mid sound frequencies, general 3D environmental geometries (e.g. with sharper variations in all three directions, backscattering and reverberations effects) and sound speed/density inhomogeneous. We then investigate various 3D scattering effects from ocean environment by the developed PFFT-BEM methods. More specifically, the major works of this thesis include:

(I) Development and validation of an efficient and robust 3D direct numerical solver for shallow water acoustics, PFFT-BEM

A highly efficient boundary element method is developed for the numerical simulation of shallow water acoustics problems. The method is based on the framework of the boundary element method for the boundary integral equation and the PFFT method which accelerate the performance of BEM solver. The accuracy and efficiency dependencies of the PFFT-BEM method for the shallow water acoustics problem is investigated in this thesis by examining the effects of the numerical element(grid) sizes, the efficiency of different preconditioners and the numerical scalability of the PFFT-BEM method. By the optimizing the performance of PFFT-BEM, the key numerical parameters with best numerical efficiency for shallow water acoustic simulations are present. Three canonical numerical benchmark problems are first considered to benchmark the PFFT-BEM method against available theoretical/numerical results: the Pekeris waveguide, the ASA wedge and Gaussian Canyon.

Our ultimate goal of developing PFFT-BEM is to provide an effective and practical simulation capability for 4D (3D+T) underwater acoustics simulations. Here, 3D+T refers to time-stepped, frozen-field modeling of underwater sound. Because sound moves at 1.5km/s in the ocean, pulsed sound traveling hundreds of kilometers could, in principle, be modeled by updating medium condition over the excursion time of hundreds of seconds as the sound moves away from the sound sources [Duda, 2017]. Two additional validation cases with time dependence and realistic ocean environment conditions are presented: (i) prediction of 4D sound scattering by traveling internal waves [Apel et al., 1997, Headrick et al., 2000, Badiey et al., 2005]; (ii) prediction of 3D sound scattering in the Mouth of the Columbia River [Reeder, 2016]. By comparison with these theoretical/experimental results, we demonstrate the efficiency and accuracy of PFFT-BEM for shallow water acoustics problems.

(II) Study on the 3D scattering by rough surface

The first underwater acoustics problem investigated in this thesis is the 3D rough surface scattering problem. Several approximate models such as the Kirchhoff approximation model [Thorsos, 1988], small roughness or slope approximation model [Thorsos and Darrell, 1989, Thorsos and Broschat, 1995] have been proposed to study the rough surface scattering problems. These approximate models obtain statistics of the rough surfaces scatterings, which can be used directly by propagation methods such as Parabolic equation method or Ray tracing method [Williams et al., 2004] to simulate the rough surface scatterings and reverberations. As a result, the validity regions of these approximation models are of critical importance for the study of underwater acoustic reverberation and forward scattering problems. By 2D numerical and analytical methods [Thorsos, 1988, Thorsos and Darrell, 1989, Thorsos et al., 2000, Isakson et al., 2008], the validity regions of these approximate models for 2D problems have been studied extensively. Due to the high computational cost, direct numerical simulations for 3D rough surface scattering problems are still limited to small cases. For medium grazing angle problem ($\theta_g \sim 45°$), we show that L needs to be at least 50λ through convergence tests. For low grazing angle ($\theta_g \sim 5°$), L needs to satisfy $L \geq 200\lambda$. For such problems, most existing 3D numerical methods are

not applicable. The developed PFFT-BEM significantly reduces the computational and memory cost of conventional numerical methods (from $O(N^{2\sim3})$ to $O(N)$). This gives us a good opportunity to study and provide new insight for the 3D rough surface scattering problems. In this thesis, we conduct direct numerical simulations of 3D rough surface scattering problems with different surface roughness and grazing angles down to 2.5°. Through 3D direct numerical simulations, we obtain the validity regions of different 3D approximate models for a Gaussian roughness surface. We compare and discuss the differences between the 2D validity and 3D validity regions. Finally, by 3D direct numerical simulations, we demonstrate and discuss the effects of grazing angles on the validity regions of these approximate models especially in the backscattering direction.

(III) Study on acoustics propagation and sacttering by underwater seamount

By the use of 3D PFFT-BEM, we next conduct numerical study of sound scatterings due to an underwater seamount. Several approximate methods have been proposed to study this problem. The $N \times 2D$ method, which was introduced by Perkins and Baer [1982], assume the out-of-plane scattering to be insignificant. For the underwater seamount problem, the azimuthal inhomogeneity and three-dimensional effects are important and can not be neglected. So the use of $N \times 2D$ method is questionable under such conditions. Another method, which is applied to study the 3D underwater seamount problem recently, is the coupled mode method. This method provides accurate results in both backscattering and forward scattering directions for cases with axisymmetric bathymetry [Taroudakis, 1996, Luo and Schmidt, 2009]. In this thesis, we assess the performance of this method by comparing 3D direct numerical results of acoustics scattering by seamounts with different cross section shapes. On the other hand, 3D parabolic equation method [Lee et al., 1990, 1992] can provide approximate solution by neglecting the backscattering effects from the seamount. However, as shown in this thesis, the backscattering effects are important for specified mountain geometries. At last, we introduce two benchmark solutions by direct numerical simulation: New Jersey shelf seamount and double seamount problem. The ocean environments and the geometry of the seamounts in these cases are closer to the real

ocean environment.

1.2 Thesis contribution

1. We develop a direct multi-layer numerical boundary element method for 4D sound wave equations without fundamental approximations.

2. By the use of pre-corrected Fast Fourier Transform (pFFT) approach which reduced the computational cost of boundary element solver from $O(N^2)$ to $O(N \log N)$, we obtain highly efficient numerical capability to account for:

   (a) Inhomogeneity of water properties

   (b) Internal and surface waves

   (c) Complex topography

   (d) Multiple-scale reverberation/scattering by bottom and water surface

3. We optimize the PFFT-BEM with efficient preconditioner and implement the developed PFFT-BEM code with efficient computational libraries on the massively parallel HPC platforms, achieving nearly linear code scalability.

4. By comparing with theoretical benchmark solutions and field measurement data, we prove that PFFT-BEM to be an effective and practical simulation capability for 4D (3D+T) underwater acoustics simulations.

5. We conduct 3D direct numerical simulation for rough surface scattering with different surface roughness conditions and sound wave grazing angles. Through 3D direct numerical simulations by PFFT-BEM, we obtain the validity regions of different approximate models for a Gaussian roughness surface with difference surface conditions and sound wave grazing angles.

6. We conduct 3D direct numerical modeling of acoustic propagation in the presence of shallow water seamount(s). We investigate numerically the importances

of seamount geometries and sound source frequencies on the acoustics scatterings. Through these numerical studies, we present the applicability of several propagation models on studying 3D underwater seamount problem.

1.3 Thesis organization

In the Chapter 2, we describe the multi-layer boundary integral equation for the shallow water acoustic problems and the formulation of multi-layer boundary element method. We then demonstrate the formulation of the PFFT algorithm to accelerate the boundary element method and the key numerical issues in its implementation in detail. We demonstrate the accuracy and efficiency dependencies of the PFFT-BEM method by examining the effects of the numerical element(grid) sizes, the efficiency of different preconditioners and the numerical scalability of the PFFT-BEM method.

In Chapter 3, we systematically investigate the accuracy and efficiency of the PFFT-BEM algorithm by examining three canonical shallow water acoustic problems: the Pekeris waveguide [Jensen et al., 2011], the ASA wedge [Deane and Buckingham, 1993] and 3D Gaussian canyon problem [Isakson et al., 2014]. In each case, excellent agreements between the 3D direct numerical simulations and the existing analytical/numerical solutions are shown. We then further investigate the efficiency and applicability of the PFFT-BEM method for realistic shallow water environments by comparing with experimental data of two field measurements: the SWARM 95 internal wave experiments [Apel et al., 1997, Headrick et al., 2000, Badiey et al., 2005] and the salt wedge experiments in Mouth of Columbia River [Reeder, 2016].

In Chapter 4, PFFT-BEM is applied to study 3D acoustics scattering from a randomly rough surface with Gaussian roughness spectra satisfying the pressure release (Dirichlet) boundary conditions. The validity regions of different approximate models for 3D scattering problems are discussed in detail. We further demonstrate the influence of sound wave grazing angles on the validity regions of these approximate models.

In Chapter 5, we study and discuss the 3D scattering problem by an underwater

seamount. By 3D direct PFFT-BEM numerical simulation, we assess the importance of 3D scattering, backsacttering and blocking effects by the seamount with different mountain geometries or sound frequencies. Our goal is to demonstrate the applicabilities of N$\times$2D approximation, axisymmetric method and parabolic equation methods for underwater seamount problems.

We finally provide our concluding remarks in Chapter 6.

Chapter 2

Mathematical formulation and implementation of pre-corrected FFT-accelerated boundary element method for shallow water acoustics

In this section, we first systematically introduce the boundary integral equation for shallow water acoustic problem and the formulation of the related boundary element method. Then, we further describe the formulation of the multi-layer PFFT-BEM algorithm that accelerate the BEM solver by reducing the computation cost from $O(N^{2\sim3})$ to $O(NlogN)$. We then investigate the accuracy and efficiency dependencies of the PFFT-BEM method by examining the effects of the numerical element(grid) sizes, the efficiency of different preconditioners and the numerical scalability of the PFFT-BEM method. From this, the optimal PFFT-BEM parameters for shallow water acoustic simulations are obtained. Using these selected numerical parameters, the capability of PFFT-BEM method in conducting 3D direct numerical simulation for shallow water acoustic problems with large scale (i.e. large domain size or higher frequency) will be demonstrated in the rest chapters of this thesis.

2.1 Formulation of multi-layer boundary element method

We start with the 3D (spatial) Helmholtz wave equation for a harmonic sound wave

$$\rho(\vec{x},t)\nabla\cdot(\frac{1}{\rho(\vec{x},t)}\nabla p(\vec{x}))+k^2p(\vec{x})=0 \qquad \vec{x}\in V \tag{2.1}$$

where $\vec{x}\equiv(x,y,z)$, t is time, $p(\vec{x})$ is the sound pressure, ∇ is the gradient operator, $\rho(\vec{x},t)$ is the medium density, V is the entire domain volume and k is the medium wavenumber. The problem is subject to the pressure release boundary condition at the water surface:

$$p(\vec{x})=0 \qquad \vec{x}\in S_F \tag{2.2}$$

where S_F is the free surface. The Sommerfeld radiation condition is satisfied at the infinity S_∞:

$$\frac{\partial p(\vec{x})}{\partial n}-ikp(\vec{x})=0 \qquad \vec{x}\to\infty \tag{2.3}$$

where n is the normal direction on the boundaries. Although shallow water environment is usually associated with penetrable bottom conditions, a rigid bottom condition could be considered easily by imposing Neumann boundary condition on the surface of rigid bottom S_B:

$$p_n(\vec{x})=0 \qquad \vec{x}\in S_B \tag{2.4}$$

For shallow water environments, a multi-layer model [Pereira et al., 2010] is adopted to account for the inhomogeneous of medium properties. In this model, we assume ρ and k in each layer to be constant at every instant of time. A sketch of the multi-layer domain is shown in Fig.2-1.

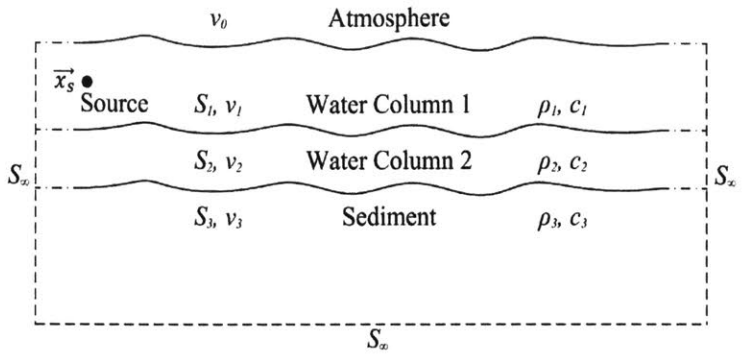

Figure 2-1: Schematic of multi-layer model with a total number $I = 3$ layers.

Then, at every instant of time, the homogeneous Helmholtz equation governing the sound field in each layer can be expressed:

$$\nabla^2 p^i(\vec{x}) + k^2 p^i(\vec{x}) = 0, \quad \vec{x} \in v_i \tag{2.5}$$

where i is the number of layers with $i = 1, ..., I$, v_i is the volume of layer i. Continuity of pressure p and particle velocity $\vec{u}$ are required across the interface $\hat{S}_{i+1}(\check{S}_i)$ of neighboring layers v_i and v_{i+1} (including at the penetrable bottoms), the symbol '$\wedge$' and '$\vee$' represents the upper and lower boundary of layer i, respectively. The continuity boundary condition across the interface can be expressed as

$$p^i = p^{i+1} \quad \vec{x} \in \hat{S}_{i+1} \tag{2.6}$$

$$\vec{u}^i = \vec{u}^{i+1} \quad \vec{x} \in \hat{S}_{i+1} \tag{2.7}$$

Based on the impedance relation between velocity and pressure, the continuity of the normal gradient of the pressure at the layer interface is derived from Eq.(2.7) as

$$\frac{1}{\rho_i} p_n^i = \frac{1}{\rho_{i+1}} p_n^{i+1} \quad \vec{x} \in \hat{S}_{i+1} \tag{2.8}$$

From Green's second theorem, the boundary integral equation (BIE) for the pres-

sure $p^i(\vec{x})$ in each layer ($\vec{x} \in v_i$) is derived from Eq. (2.5) as

$$\alpha p^i(\vec{x}) - \iint_{S_i} p_n^i(\vec{\zeta}) G(\vec{x};\vec{\zeta}) dS_i(\vec{\zeta}) + \iint_{S_i} p^i(\vec{\zeta}) G_n(\vec{x};\vec{\zeta}) dS_i(\vec{\zeta}) = 0 \qquad (2.9)$$

where S_i is the boundary of each layer (note that $S_1 \equiv S_F$), $G(\vec{x};\vec{\zeta}) = \frac{1}{|\vec{x}-\vec{\zeta}|} e^{ik|(\vec{x}-\vec{\zeta})|}$ is the Green function which satisfies the Helmholtz equation, $\vec{\zeta}$ is a dummy variable representing the point on the layer boundary S_i, and α is the solid angle.

To demonstrate the coupled domain BEM formulation, we consider the multi-layer case shown in Fig.2-1. By taking the limit of $\vec{x} \to S_i$ and using boundary conditions Eq.(2.2), Eq.(2.3), Eq.(2.6) and Eq.(2.8), the BIE in Eq.(2.9) for each layer can be coupled into one large set of integral equations as

$$\begin{cases} \alpha p^1(\vec{x}) - \iint_{\hat{S}_1} \hat{p}_n^1(\vec{\zeta}) G(\vec{x};\vec{\zeta}) d\hat{S}_1(\vec{\zeta}) + \beta_1 \iint_{\check{S}_1} \hat{p}_n^2(\vec{\zeta}) G(\vec{x};\vec{\zeta}) d\check{S}_1(\vec{\zeta}) + \iint_{\check{S}_1} \hat{p}^2(\vec{\zeta}) G_n(\vec{x};\vec{\zeta}) d\check{S}_1(\vec{\zeta}) \\ = 4\pi f_s e^{ik|\vec{x}-\vec{x}_s|} |\vec{x}-\vec{x}_s|^{-1}, \qquad \vec{x} \in S_1 \\ \\ \alpha p^i(\vec{x}) - \iint_{\hat{S}_i} \hat{p}_n^i(\vec{\zeta}) G(\vec{x};\vec{\zeta}) d\hat{S}_i(\vec{\zeta}) + \iint_{\hat{S}_i} \hat{p}^i(\vec{\zeta}) G_n(\vec{x};\vec{\zeta}) d\hat{S}_i(\vec{\zeta})) + \beta_i \iint_{\check{S}_i} \hat{p}_n^{i+1}(\vec{\zeta}) G(\vec{x};\vec{\zeta}) d\check{S}_i(\vec{\zeta}) \\ + \iint_{\check{S}_i} \hat{p}^{i+1}(\vec{\zeta}) G_n(\vec{x};\vec{\zeta}) d\check{S}_i(\vec{\zeta}) = 0, \qquad \vec{x} \in S_{2,\ldots I-1} \\ \\ \alpha p^I(\vec{x}) - \iint_{\hat{S}_I} \hat{p}_n^I(\vec{\zeta}) G(\vec{x};\vec{\zeta}) d\hat{S}_I(\vec{\zeta}) + \iint_{\hat{S}_I} \hat{p}^I(\vec{\zeta}) G_n(\vec{x};\vec{\zeta}) d\hat{S}_I(\vec{\zeta}) = 0, \qquad \vec{x} \in S_I \end{cases} \qquad (2.10)$$

where f_s is the strength of a point source located at $\vec{x}_s$ in layer 1 as shown in Fig.2-1. $\beta_i = \frac{\rho_i}{\rho_{i+1}}$. It should be noted that the Green's function automatically satisfies the Sommerfeld condition given by Eq.(2.3), therefore, S_∞ does not appear in Eq.(2.10) [Wu, 1994, Pereira et al., 2010].

For simplicity, we used Constant Panel Method (CPM) in the present study. In this method, we discretize the boundaries of all of the layers into N quadrilateral elements. On each element, the quantities such as the acoustic pressure p and the normal gradient of the pressure p_n are assumed to be constant. These transfer Eq.(2.10) into

a set of linear algebraic equations of the form

$$\begin{cases} 2\pi p^1(\vec{x}) - \sum_{j=1}^{N^1}(\hat{F}_s^1)_j + \beta_1 \sum_{j=1}^{N^2}(\hat{F}_s^2)_j + \sum_{j=1}^{N^2}(\hat{F}_d^2)_j = 4\pi f_s e^{ik|\vec{x}-\vec{x}_s|}|\vec{x}-\vec{x}_s|^{-1}, & \vec{x} \in S_1 \\ 2\pi p^i(\vec{x}) - \sum_{j=1}^{N^i}(\hat{F}_s^i)_j + \sum_{j=1}^{N^i}(\hat{F}_d^i)_j + \beta_i \sum_{j=1}^{N^{i+1}}(\hat{F}_s^{i+1})_j + \sum_{j=1}^{N^{i+1}}(\hat{F}_d^{i+1})_j = 0, & \vec{x} \in S_{2,\ldots I-1} \\ 2\pi p^I(\vec{x}) - \sum_{j=1}^{N^I}(\hat{F}_s^I)_j + \sum_{j=1}^{N^I}(\hat{F}_d^I)_j = 0, & \vec{x} \in S_I \end{cases} \tag{2.11}$$

with

$$(\hat{F}_s^i)_j = (\hat{p}_n^i)_j \iint_{E_j} G(\vec{x};\vec{\zeta}) d\hat{S}_i(\vec{\zeta});\ (\check{F}_s^i)_j = (\hat{p}_n^i)_j \iint_{E_j} G(\vec{x};\vec{\zeta}) d\check{S}_i(\vec{\zeta}) \tag{2.12}$$

$$(\hat{F}_d^i)_j = (\hat{p}^i)_j \iint_{E_j} G_{n(\vec{\zeta})}(\vec{x};\vec{\zeta}) d\hat{S}_i(\vec{\zeta});\ (\check{F}_d^i)_j = (\hat{p}^i)_j \iint_{E_j} G_{n(\vec{\zeta})}(\vec{x};\vec{\zeta}) d\check{S}_i(\vec{\zeta}) \tag{2.13}$$

where E_j represents the j^{th} constant element and N^i is the total element numbers in i^{th} layer. Here, solid angel α equals to 2π on the smooth domain boundary based on CPM. The entire linear system of equations, Eq.(2.11), is then expressed as

$$[A]\{x\} = \{b\} \tag{2.14}$$

where $[A]$ is a $N \times N$ dense and nonsymmetric matrix of influence coefficients with $N = \sum_{i=1}^{I} N^i$, $\{x\}$ is the vector of unknowns (p and p_n) on domain surface and $\{b\}$ is the known vector due to the point source at x_s. Equation (2.14) may be solved using direct matrix inversion method such as Gaussian elimination, which requires $O(N^3)$ operations. An iterative solver such as the generalized minimum residual (GMRES) method [Saad and Schultz, 1986] could also be applied to solve the system Eq.(2.14). GMRES normally requires $O(N_{itr}N^2)$ operations with N_{itr} the iteration numbers of the GMRES solver. The most expensive step in the iterative solver is matrix-vector product ($[A]\{x\}$) which require a minimum of $O(N^2)$ operations. Physically, each multiplication F_s (or F_d) in $[A]\{x\}$ represents the influence from element j to element

i on the domain boundary. As a result, the N elements contain N^2 interactions. The $O(N^2)$ effort of the iterative methods limits the applicability of BEM to 3D underwater acoustic problems involving a large number(N) of unknowns (e.g. large domains or high frequency).

2.2 Formulation of pre-corrected fast Fouier transform method

An alternative approach is to use the Precorrected-FFT algorithm which can evaluate the product $[A]\{x\}$ with $O(NlogN)$ operations without explicit construction of the matrix $[A]$. This efficient numerical algorithm is developed to solve acoustic propagation and scattering problems in shallow water environments in the present study.

For illustration, we consider the form of pressure $p(\vec{x})$ at point $\vec{x}$ due to a source $(G(\vec{x};\vec{\zeta}))$ distribution on N boundary elements on S, e.g.

$$p(\vec{x}) = \sum_{j=1}^{N} \iint_{E_j} \sigma(\vec{\zeta}) G(\vec{x};\vec{\zeta}) dS(\vec{\zeta}) = \sum_{j=1}^{N} I_{sj}(\vec{x}) \tag{2.15}$$

where E_j is the j^{th} boundary element, σ is the strength of source distribution, and I_{sj} is the contribution to the pressure at $\vec{x}$ due to the source distribution on the j^{th} element.

The evaluation of pressure $p(\vec{x})$ in Eq.(2.15) for $\vec{x}$ at the collocation points of N elements by the PFFT algorithm mainly contains five steps: (i) grid definition, (ii) projection, (iii) convolution, (iv) interpolation and (v) near field correction.

Grid definition: In this step, we identify a 3D block that contains the entire 3D domain after it has already been discretized into the N boundary elements. By subdividing this 3D block into a grid of small cubes, each differential cube will contain only a few of the boundary elements. Each of these small cubes is referred to as a cell. By temporarily computing the pressures on the cell grid points, we can account

for the distant interactions by using only a few weighted local pressure cell values. Furthermore, by evaluating these pressures on a uniform grid, the pressure evaluation has the form of a convolution (will be derived in the projection step) which allows for it to be evaluated with FFTs. Correction steps are then taken at the end of the algorithm to adjust the solution from the cell values back to the boundary element mesh. Our algorithm constructs this surrounding grid using $N_x \times N_y \times N_z$ uniform grid in the $x-$, $y-$, $z-$ directions (with $N_g \equiv N_x \times N_y \times N_z$). Note that the grid size h does not necessarily need to be identical in the three directions. Without loss of generality, h is considered to be constant [Yan and Liu, 2011].

Projection: In this step, the source distribution Eq.(2.15) is projected to point sources at the $v^3 (v \geq 2)$ vertices of the cell which contains the boundary element E_j. An accurate projection must satisfy the requirement that the $p(\vec{x})$ obtained from the net influence of the point source at cell vertices must be identical to that of the original source distribution on the elements.

In order to do that, we first represent the Green function $G(\vec{x}; \vec{\zeta})$ (i.e. $p(\vec{x})$ results from a unit source at $\vec{\zeta}$) by the net influence of point sources at the vertices of the cell which covers point source $G(\vec{x}; \vec{\zeta})$:

$$G(\vec{x}; \vec{\zeta}) = \sum_{m=1}^{v^3} H_m(\vec{\zeta}_m) G(\vec{x}; \vec{\zeta}_m) \tag{2.16}$$

where $\vec{\zeta}_m$ is the coordinate of the m^{th} vertex of the cell which covers the element E_j and H_m is the spatial interpolation function for the m^{th} vertex of the cell. Several methods has been proposed to to construct H. The most direct way is to expand the left and right hand sides of Eq.(2.16) separately based on Taylor series expansion and obtain the expansion coefficient by matching the two sides of the equation. However, this method is very tedious and thus time consuming. We here follow the same procedure proposed by Yan and Liu [2011] which obtained the same H as the direct way but with much less computational efforts. We take the Green function $G(\vec{x}; \vec{\zeta})$ and a cell with 2^3 vertices as an example. We define a set of linear function which

can represent the function G as

$$G(\vec{x};\vec{\zeta}) = \sum_{k=1}^{K=4} c_k(\vec{x}) f_k(\vec{\zeta}) = \{f\}^T(\vec{\zeta})\{c\}(\vec{x}) \tag{2.17}$$

where $f_k(\vec{\zeta}) = 1, \zeta, \eta, \xi$ for $k = 1, 2, 3, 4$, respectively, $\{f\}^T = \{f_1, f_2, ..., f_K\}$, and $\{c\} = \{c_1, c_2, ..., c_K\}^T$. The unknown coefficient vector $\{c\}$ could be obtained by substituting the values of G at vertices of the cell ζ_m, $m = 1, 2, ..., 8$ into Eq.(2.17).

$$\{G\}(\vec{x}) = \begin{bmatrix} G_1(\vec{x},\vec{\zeta_1}) \\ G_2(\vec{x},\vec{\zeta_2}) \\ \vdots \\ G_8(\vec{x},\vec{\zeta_8}) \end{bmatrix} = \begin{bmatrix} f_1(\vec{\zeta_1}) & f_2(\vec{\zeta_1}) \cdots f_K(\vec{\zeta_1}) \\ f_1(\vec{\zeta_2}) & f_2(\vec{\zeta_2}) \cdots f_K(\vec{\zeta_2}) \\ \vdots & \vdots \quad \vdots \\ f_1(\vec{\zeta_8}) & f_2(\vec{\zeta_8}) \cdots f_K(\vec{\zeta_8}) \end{bmatrix} \cdot \begin{bmatrix} c_1(\vec{x}) \\ c_2(\vec{x}) \\ \vdots \\ c_K(\vec{x}) \end{bmatrix} = [F]\{c\}(\vec{x}) \tag{2.18}$$

For a given $\vec{x}$, $\{G\}$ and $[F]$ are known. We thus solve for $\{c\}$ from solving Eq.(2.18).

$$\{c\}(\vec{x}) = [F]^{-1}\{G\}\{\vec{x}\} \tag{2.19}$$

After substituting Eq.(2.19) into Eq.(2.17), we could obtain $G(\vec{x},\vec{\zeta})$ inside the cell represented in terms of $G(\vec{x};\vec{\zeta_m})$ at the cell vertices as

$$G(\vec{x};\vec{\zeta}) = \{f\}^T(\vec{\zeta})[F]^{-1}\{G\}(\vec{x}) \tag{2.20}$$

Comparing Eq.(2.20) with Eq.(2.16), we obtain the linear interpolation function H as

$$\{H\}(\vec{\zeta}) = \{f\}^T(\vec{\zeta})[F]^{-1} \tag{2.21}$$

where $\{H\} = \{H_1, H_2, ..., H_8\}^T$ for a 8 vertices cell. For $K = 4$, Eq.(2.18) is an over-determined system of equations and the singular value decomposition method could be applied to obtain $[F]^{-1}$. Instead of using Eq.(2.17), we can also approximate the

Green function inside a cell with 2^3 vertices as

$$G(\vec{x};\vec{\zeta}) = \sum_{k=1}^{K=8} c_k(\vec{x}) f_k(\vec{\zeta}) \tag{2.22}$$

where $f_k(\zeta) = 1, \zeta, \eta, \xi, \zeta\eta, \eta\xi, \zeta\xi, \zeta\eta\xi$ for $k = 1, 2, ..., 8$, respectively.

Following the same procedure in Eq.(2.18)-Eq.(2.21), we could obtain the interpolation function $\{H\}$ in another form as

$$H_m(\vec{\zeta}) = \frac{1}{8}(1+\zeta\zeta_m)(1+\eta\eta_m)(1+\xi\xi_m), \qquad m = 1, 2, ..., 8 \tag{2.23}$$

where (ζ, η, ξ) are the coordinate of cell vertices in a natural coordinate system. The quadratic terms ζ^2, η^2 or ξ^2 are not included as it would make $[F]$ in Eq.(2.18) singular due to the symmetry property of the matrix. In addition, although more terms are included in Eq.(2.22) than in Eq.(2.17), it does not necessarily give more accurate solution as the maximum errors in these two methods are in the same quadratic order.

On the other hand, we could obtain a interpolation function $\{H\}$ which includes partial cubic and complete quadratic terms for a 3^3 vertices cells. One way to derive $\{H\}$ based on a 27-vertex cell is to write G in the form as

$$G(\vec{x};\vec{\zeta}) = \sum_{k=1}^{K=17} c(\vec{x}) f_k(\vec{\zeta}) \tag{2.24}$$

where $f_k(\vec{\zeta}) = 1, \zeta, \eta, \xi, \zeta^2, \eta^2, \xi^2, \zeta\eta, \eta\xi, \zeta\xi, \zeta\eta\xi, \zeta\eta^2, \zeta^2\eta, \zeta^2\xi, \xi^2\zeta, \eta\zeta^2, \eta^2\xi$ for $k = 1, 2, ..., 17$, respectively. Following the same procedure as described to solve for linear interpolation functions, the quadratic interpolation functions could also be determined. As a result, $I_{sj}(\vec{x})$ is expressed as

$$I_{sj}(\vec{x}) = \iint_{E_j} \sigma(\vec{\zeta}) G(\vec{x};\vec{\zeta}) dS(\vec{\zeta}) = \sum_{m=1}^{v^3} q_{jm} G(\vec{x};\vec{\zeta}_m) \tag{2.25}$$

where

$$q_{jm} = \sigma(\vec{\zeta}) \iint_{E_j} H_m(\vec{\zeta}) dS(\vec{\zeta}) \tag{2.26}$$

Eq.(2.26) is used to determine the strength of the projected point source, q_{jm}, at m^{th} vertex of the cell associated with the j^{th} element. After taking the summation of all the projections of the boundary elements associated with the uniform 3D FFT grid n, the total strength of the point source at n^{th} grid q_n is given by

$$q_n = \sum_{j=1}^{N_n} q_{jn} \tag{2.27}$$

with $n = 0, 1, ..., N_g - 1$, N_n represents the total number of boundary elements associated with the uniform 3D FFT grid n.

Convolution: In this step, we evaluate the pressure at the $3D$ grid points due to point sources at these grids as

$$p_l = \sum_{n=0}^{N_g-1} q_n G_{l-n} \quad l = 0, 1, ..., N_g - 1 \tag{2.28}$$

where $G_{l-n} = \frac{1}{|x_l - x_n|} e^{ik|x_l - x_n|}$.The Fast Fourier Transform (FFT) is used to evaluate Eq.(2.28) efficiently as it is in a convolution form. Before directly applying FFT, the forms of the G and q terms needs to be modified since the total number of G terms differs from that of q and due to G_0 being singular. To do this, we fist define a function P as

$$P_l = \sum_{n=-N_g+1}^{N_g-1} q'_n G'_{l-n}, \quad l = -N_g + 1, ..., 0, 1, ..., N_g - 1 \tag{2.29}$$

where q' and G' are periodic with the same period $(2N_g - 1)$ and are defined as

$$G'_{l-n} = \begin{cases} 0, & l = n, \\ G_{l-n}, & -N_g + 1 \leq l - n \leq N_g - 1 \text{ and } l \neq n \end{cases} \tag{2.30}$$

and

$$q'_n = \begin{cases} 0, & -N_g + 1 \leq n \leq 0, \\ q_n, & 0 \leq n \leq N_g - 1. \end{cases} \tag{2.31}$$

Eq.(2.29) is now in the convolution form of two discrete periodic functions. Therefore, FFTs can be directly applied to evaluate P_l for a given q' and G' with a computational cost of $O(N_g log N_g)$. With the self influence excluded from p in Eq.(2.28), we have $p_l = P_l$, $l = 0, 1, ..., N_g - 1$ (the self influence of point source will be added to solution in the step of near field correction).

Interpolation: In this step, we evaluate $p(\vec{x})$ on the boundary elements using the interpolation function H_m based on the grid values p_l obtained in the convolution step. The form of $p(\vec{x})$ can now be expressed as

$$p(\vec{x}) = \sum_{m=1}^{v^3} H_m(\vec{x}) p(\vec{\zeta_m}), \tag{2.32}$$

where m is the m^{th} vertex of the cell surrounds the element located at $\vec{x}$.

Near field correction: In this step, we correct the near field part of $p(\vec{x})$ evaluated by FFT based on Eq.(2.25). This is due to the fact that when $|x - \zeta|/h \leq O(1)$, the accuracy of representation of $G(\vec{x}; \vec{\zeta})$ by $G(\vec{x}; \vec{\zeta_m})$, $m = 1, ..., v^3$ deteriorates. In this step, the near field contribution evaluated in the convolution step and the exact near field contribution obtained using direct computation is subtracted and added to the solution, respectively. The correction $\Delta p(\vec{x})$ is represented as

$$\Delta p(\vec{x}) = p_N(\vec{x}) - p_{FN}(\vec{x}) \tag{2.33}$$

where $p_{FN}(\vec{x})$ is the near-field part of the influence obtained from Eq.(2.32) based on the results in convolution step and $p_N(\vec{x})$ is the exact influence of the near-field elements determined by directly evaluating the boundary element integrals in Eq.(2.15). Then, the final result of $p(\vec{x})$

$$p(\vec{x}) = p_F(\vec{x}) + \Delta p(\vec{x}) \tag{2.34}$$

where $p_F(\vec{x})$ is the total influence results evaluated from the convolution step.

Similarly, p_n can be valuated by the same manner using PFFT algoritm. We

consider the normal gradient of the pressure $p_n(\vec{x})$ at $\vec{x}$ due to the influence of the dipole distribution with strength $\gamma(\vec{\zeta})$ on a surface S, e.g.

$$p_n(\vec{x}) = \int\int_S \gamma(\vec{\zeta}) G_{n(\vec{\zeta})}(\vec{x};\vec{\zeta}) dS(\vec{\zeta}) = I_\zeta(\vec{x}) + I_\eta(\vec{x}) + I_\xi(\vec{x}) \tag{2.35}$$

$$I_\chi(\vec{x}) = \int\int_S n_\chi(\vec{\zeta})\gamma(\vec{\zeta}) G_\chi(\vec{x};\vec{\zeta}) dS(\vec{\zeta}), \quad \chi = \zeta, \eta, \xi \tag{2.36}$$

where (n_ζ, n_η, n_ξ) are the three components of the unit normal on $S(\vec{\zeta})$. Instead of the $G(\vec{x},\vec{\zeta})$ from the earlier description, we now have $G_\zeta(\vec{x},\vec{\zeta}) = G_\zeta(\vec{x}-\vec{\zeta})$, $G_\eta(\vec{x},\vec{\zeta}) = G_\eta(\vec{x}-\vec{\zeta})$ and $G_\xi(\vec{x},\vec{\zeta}) = G_\xi(\vec{x}-\vec{\zeta})$. As a result, $I_\zeta(I_\eta,\ I_\xi)$ can be determined using the PFFT algorithm described in the above with G and σ replaced by $G_\zeta(G_\eta,\ G_\xi)$ and $n_\zeta\gamma(n_\eta\gamma,\ n_\xi\gamma)$, respectively.

In summary, the evaluation of the pressure p on the boundary by the PFFT algorithm involves computational accounts of $O(N)$, $O(v^3N)$, $O(N_g log N_g)$, $O(N)$, and $O(v^3N)$ in the grid definition, projection, convolution, interpolation and near-field correction steps, respectively. For shallow water applications, N_g is normally of the same order as N. The total computational cost using the PFFT-BEM algorithm is thus $\sim O(NlogN)$ which is much lower comparing with conventional BEM with $O(N^2)$ for $N >> 1$.

In this section, we have shown the formulations of coupled layer BEM and the PFFT-BEM algorithm for 3D shallow water acoustic problem. The key numerical steps of PFFT-BEM are illustrated. It is shown that the PFFT-BEM method reduces the computational cost from $O(N^2)$ to $O(NlogN)$ which is much more efficient for $N >> 1$. As a result, the PFFT-BEM method is very suitable to study the shallow water acoustic problems in which complex 3D and large scale computational domains are usually considered.

2.3 Accuracy dependence on numerical parameters

In order to investigate the numerical accuracy and efficiency of PFFT-BEM algorithm for shallow water waveguide problem, we begin by considering a Pekeris waveguide

problem [Jensen et al., 2011] with flat pressure release boundary on the top and flat penetrable bottom. A unit source with frequency $f = 20\text{Hz}$ is located at depth $z = 36m$. The depth of the upper water column $H = 100m$ with an infinite depth in the bottom layer. The water column has a density $\rho_1 = 1g/cm^3$ and sound speed $c_1 = 1500m/s$ while $\rho_2 = 1.8g/cm^3$ and $c_2 = 1800m/s$ in the bottom layer. Different computational domain and element(grid) sizes will be used and compared in order to demonstrate the accuracy and efficiency of PFFT-BEM.

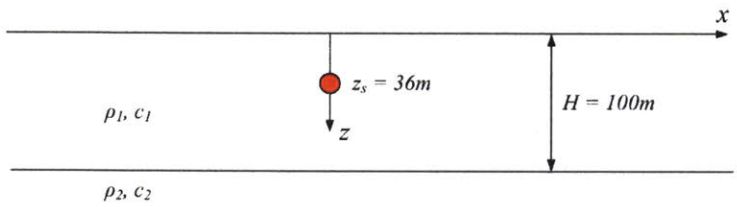

Figure 2-2: Geometry of the Pekeris waveguides [Jensen et al., 2011]: a $20Hz$ point source is located at z=36m. The depth of the upper water column $H = 100m$ with an infinite depth in the bottom layer. The water column has a density $\rho_1 = 1g/cm^3$ and sound speed $c_1 = 1500m/s$ while $\rho_2 = 1.8g/cm^3$ and $c_2 = 1800m/s$ in the bottom layer

Two important factors that determine the accuracy of the PFFT-BEM are investigated: the interpolation from boundary elements to FFT-grids and the discretization of FFT-grids and boundary elements.

We first examine the behavior of the interpolation errors. In the far field, the interpolation error is determined by the ratio between the FFT grid size h and the acoustic wavelength λ (i.e. h/λ). In the present study, we chose h/λ to equal to $\Delta l/\lambda$ where Δl is the size of the boundary elements. This ensures that the interpolation error is of the same order as the discretization error in the far field. In the near field, the interpolation error is a function of the polynomial order β of the interpolation function H where $\beta = 1, 2$ denotes linear (i.e. Eq.(2.17)) or quadratic polynomials (i.e. Eq.(2.24)) and d/h is the critical distance separating the near and far fields.

We compare the p_n on the top surface (pressure release boundary) and p on

the bottom surface (penetrable boundary) of the Pekeris waveguide obtained using PFFT-BEM with the numerical solutions obtained by conventional BEM. The computational domain size of the Pekeris waveguide is chosen as $1km \times 1km \times 100m$ with uniform meshing $\Delta l = h = \lambda/12$. In Fig.2-3(a), ϵ denotes the average difference between conventional BEM solutions and PFFT-BEM solutions normalized by the conventional BEM solutions (e.g. for p, $\epsilon = \frac{1}{N}\sum_i^N |((p_{BEM})_i - (p_{PFFT})_i)/(p_{BEM})_i|$) and is shown as a function of d/h. It is seen that for both $\beta = 1$ and 2, ϵ decays with increasing d/h, as expected. In addition, the convergence rate of the PFFT-BEM solutions with increasing d/h are much faster when quadratic interpolation functions ($\beta = 2$) are used.

To compare computational cost, PFFT-BEM with $\beta = 1, 2$ are applied to solve the Pekris waveguide problem using different size of meshing. Using the numerical experiment shown in Fig.2-3(b), we compare the operation count per iteration N_{op} for PFFT-BEM using different β and it is seen that $\beta = 2$ uses only slightly more CPU operations per iteration than the $\beta = 1$ scheme. For underwater sound field measurements [Robinson et al., 2014]), the uncertainty of the receiver system in laboratory conditions is approximately $\pm 0.1dB$, and the overall uncertainty for a field receiver is $\pm 1dB$. As a result, an average relative error of $\epsilon \sim 1\%$ (i.e. $0.1dB$) would be sufficient for the underwater acoustic numerical simulation and is used as the standard to judge the methods of interpolation and discretization in the present study. As a result, we have chosen to use the PFFT-BEM parameters as $\beta = 2$, $d/h = 3$ for the remainder of the study.

To examine the discretization error, we compare our numerical solution of the Pekeris waveguide with the known analytical solution [Jensen et al., 2011] in order to understand the convergence characteristics of the PFFT-BEM numerical predictions. Here, we continue to use that $d/h = 3$ and $\beta = 2$. The maximum and averaged errors between the analytical results and the numerical values is defined as

$$\epsilon_{average} = \frac{1}{N}\sum_i^N |((p_{PFFT})_i - (p_{analytical})_i)/(p_{analytical})_i| \tag{2.37}$$

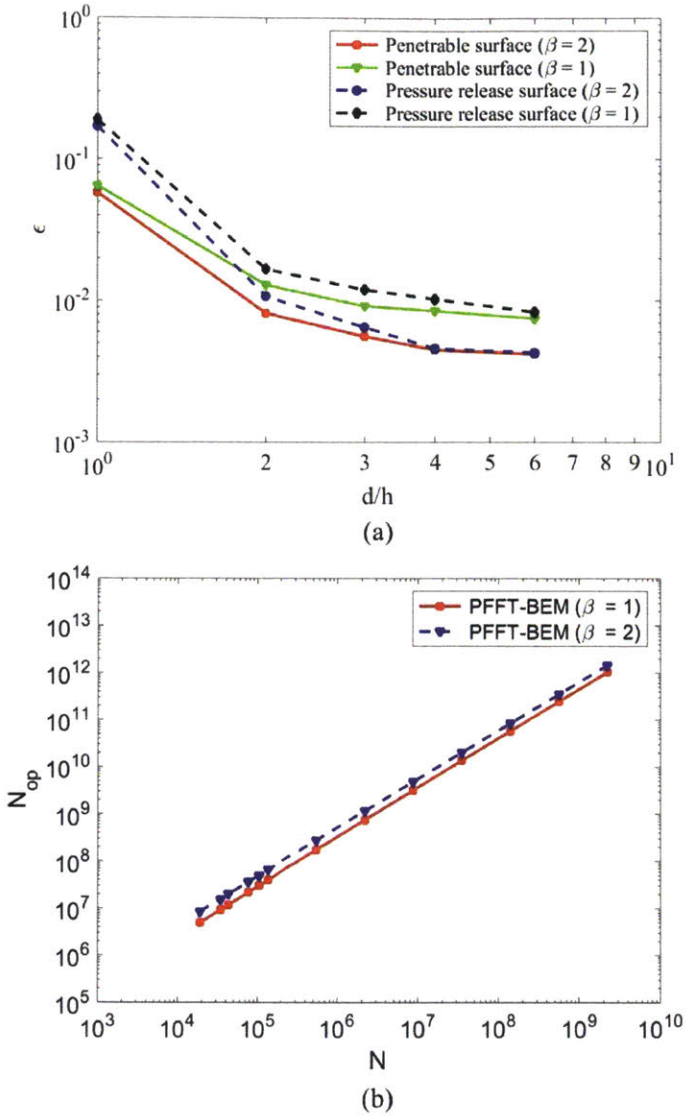

Figure 2-3: (a) Normalized average interpolation errors ϵ between PFFT-BEM and conventional BEM on different surfaces as a function of d/h. (b) Comparison of operation count per iteration step of PFFT-BEM using linear (β=1) and quadratic (β=2) interpolation function as a function of N.

$$\epsilon_{max} = \max\{|((p_{PFFT})_i - (p_{analytical})_i)/(p_{analytical})_i|\} \tag{2.38}$$

are shown in Fig.2-4. The errors of pressure at $z = 46m$ decrease approximately

quadratically as element (and grid) size $\Delta l/\lambda$ decrease (i.e. decrease linearly with the element area) as expected.

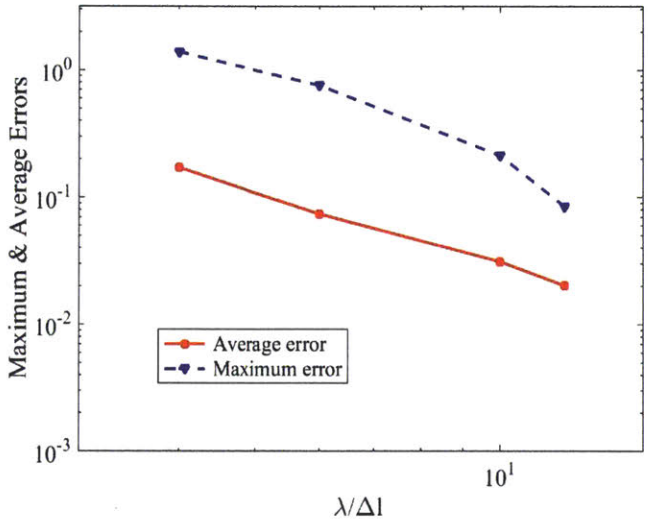

Figure 2-4: Normalized average $\epsilon_{average}$ and maximum ϵ_{max} errors of the pressure at $z = 46m$ of the Pekeris waveguide obtained using the PFFT-BEM as a function of $\lambda/\Delta l$. The slopes κ are approximately equals to -2 for both the maximum and averaged errors shown.

2.4 Determination of preconditioner

The computational cost in solving Eq.(2.9) is also largely impacted by the convergence rate of the iterative solver (i.e. N_{itr} defined in section 4.2). An efficient preconditioner [Axelsson, 1996] can significantly increase the convergence rate of the iterative solver (i.e. reduce N_{itr}) and thus reduce the computational cost. The pattern of matrix A highly determines the effectiveness of the a preconditioner. It is well known that the Jacobian preconditioner (i.e. diagonal preconditioner), which is widely used for Neumann problem in which A is a diagonal dominant matrix, is not efficient for the Dirichlet or mixed boundary condition problem in which A is not a diagonal dominant matrix. In this study, we use a so called 'Mesh-based Neighbor(MN)' preconditioner

which has been shown to be useful in different kinds of boundary value problems [Chen, 1998, Harris and Chen, 2003]. The key idea of this method is to approximate the dense matrix A^{-1} by a sparse matrix M^{-1} and solve the system as

$$M^{-1}Ax = M^{-1}b \tag{2.39}$$

It is found that as $M \rightarrow A$, the system would converge faster. For general BEM problems, the influences from far field elements are generally much weaker than the neighboring elements' and decays as $1/r$. Thus an effective pattern for the j^{th} column of M^{-1} can be computed by selecting and meshing only neighboring elements of element j to formulate and inverse the submatrix. By doing this, we can capture the main entries of A^{-1} as M^{-1} while keeping M^{-1} reasonably sparse. We test MN method for Pekeris waveguide with two different size of $1km \times 1km \times 100m$ and $25km \times 15km \times 100m$. Here, we chose $d/h = 3$, $\beta = 2$ and $\Delta l/\lambda = 1/8$. Three different MN preconditioners are used: the diagonal-type preconditioner for which only the mesh's self interaction is considered; the MN preconditioner including 2 neighboring meshes ($N_m = 2$); and the MN preconditioner including 4 neighboring meshes ($N_m = 4$). The case without a preconditioner is also presented for comparison. In Fig.2-5(a), the MN-preconditioner is shown to improve the computational speed of the PFFT-BEM code by nearly an order of magnitude for the small Pekeris waveguide problem. For the larger case, as shown in Fig.2-5(b), the preconditioner increases the convergence speed by nearly 2+ orders of magnitude. Comparison of the various MN methods shown in Fig.2-5 shows that although faster convergence is obtained with the larger matrix bandwidth, the increase is not dramatically significant above $N_m = 2$. This further confirms that the influence of the neighboring elements decays rapidly with distance from the element.

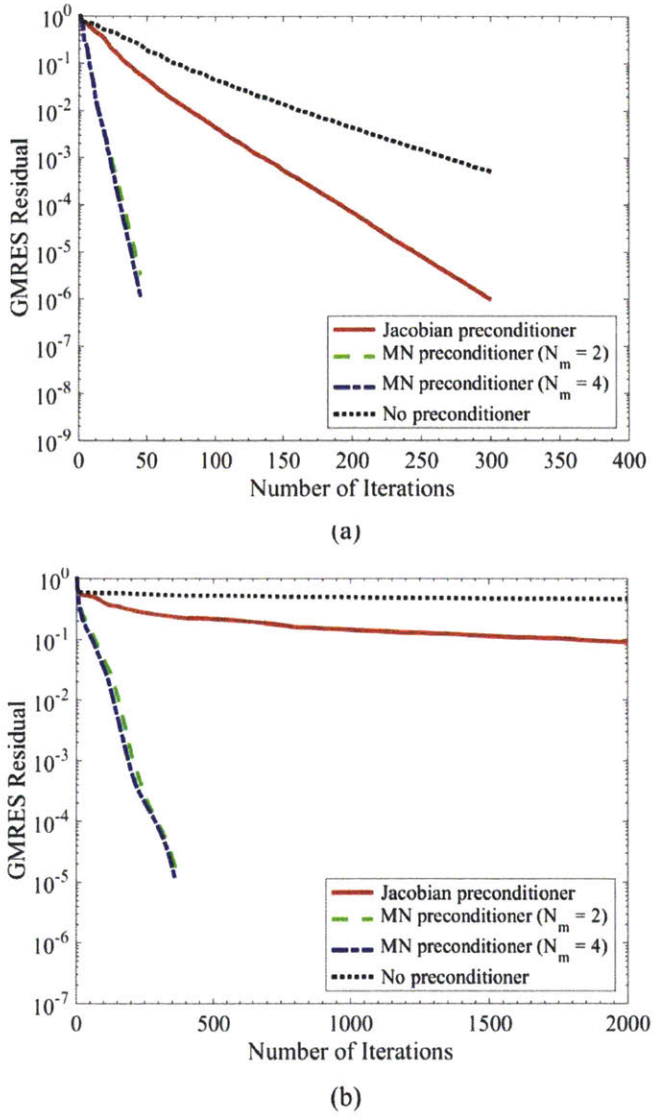

Figure 2-5: GMRES residual [Saad and Schultz, 1986] as a function of iteration number for the (a) Pekeris waveguide problem with size of $1km \times 1km \times 100m$, (b) Pekeris waveguide problem with size of $25km \times 15km \times 100m$. The results are obtained: without a preconditoner, with Jacobian diagonal preconditioner and MN precondtioner with neighboring meshes $N_m = 2, 4$.

2.5 PFFT-BEM scalability on numbers of processors and unknowns

To further increase the numerical capability, the PFFT-BEM is implemented using the PETSc software package which allows for efficient highly scalable algorithms to be developed [Balay et al., 2017]. To demonstrate the scalability of the parallelized PFFT-BEM, we report the scaling results by comparing the total execution time for a fixed problem as a function of the total processor count. We perform this test using a finely meshed Pekeris waveguide case with a computational domain of size $10km \times 10km \times 100m$ and element size $\Delta l = \lambda/16$ which makes $N = 7 \times 10^6$. We use $\beta = 2$, $d/h = 3$ and $N_m = 2$ in this case. The test is carried out using: $P = [120, 240, 320, 480, 600, 800, 960]$ where P is the number of processors that are used. As shown in Fig.2-7(a), we define a variable called 'speed up' which defined as the CPU time for a run with P processor compared with the run with $P = 120$ case. Strong scaling is observed in Fig.2-7(a) with the computational speedup being nearly linear with the processor count.

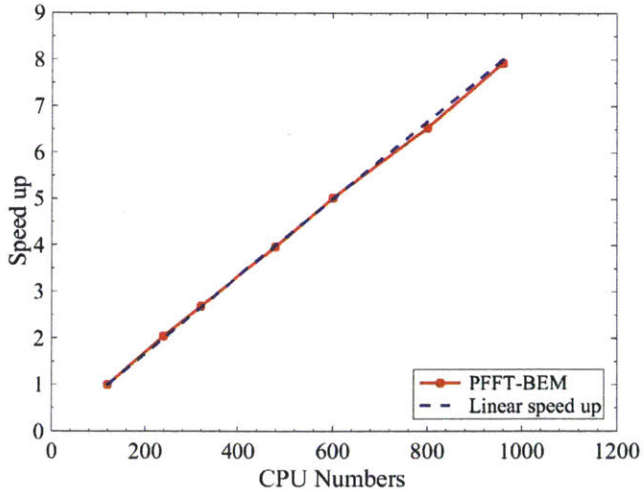

Figure 2-6: CPU scaling for the Pekeris waveguide and fixed $N = 7 \times 10^6$, with increasing processors counts, using PFFT-BEM.

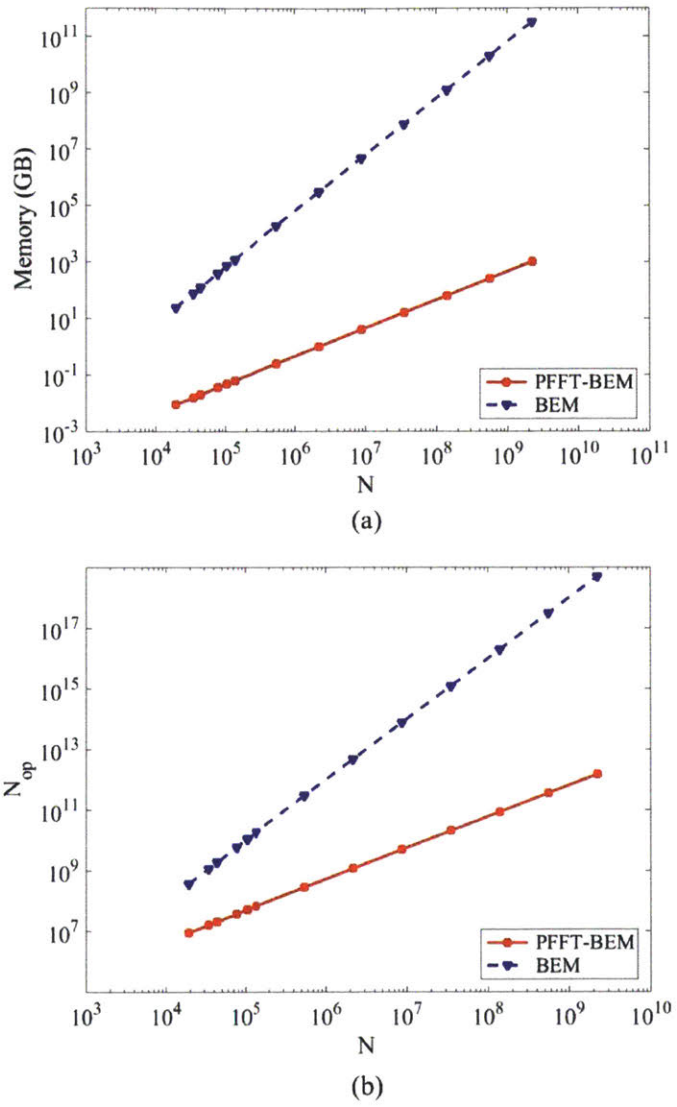

Figure 2-7: (a) Comparison of memory requirement of PFFT-BEM method (slope $\kappa \sim 1$) and conventional BEM (slope $\kappa \sim 2$) as a function of N. (b) Comparison of operation count per iteration step of PFFT-BEM method (slope $\kappa \sim 1$) and conventional BEM (slope $\kappa \sim 2$) as a function of N.

In Fig.2-7(b), we plot the operation count per iterative step of PFFT-BEM versus different N for the Pekeris waveguide problem. We use $\beta = 2$, $d/h = 3$ and $N_m = 2$ in this case. For comparison, the computational effort of conventional BEM is also

plot. It can be seen that the computational effort is proportional to N for PFFT-BEM while that of conventional BEM is proportional to N^2 and much larger than the computational effort of PFFT-BEM.

We will further demonstrate the effectiveness of the PFFT-BEM method and its capability in simulating realistic acoustic wave propagation and scattering problems in 3D range dependent environments by examining three canonical shallow water problems: the Pekeris waveguide, the ASA wedge and a 3D underwater seamount problem. We have chosen to use the PFFT-BEM parameters as $\beta = 2$, $d/h = 3$ and $N_m = 2$ in all these benchmark cases. Different grid(element) sizes are used to show the convergence of the numerical results towards the theoretical results. All the computations are performed on parallel HPC platforms with large number of computational nodes that each contains 32 Intel Xeon processors clocked at 2.3GHz.

2.6 Concluding remarks

We develop a highly efficient multi-layer boundary element method for large scales acoustics propagation and scattering in shallow water environment with complex medium and boundaries. The method is based on the integration of the pre-corrected fas Fourier transform (PFFT) algorithm into the constant boundary integral solver. The developed PFFT-BEM reduces the computational operations for the boundary value solution from O($N^{2\sim3}$) to O(Nlog N), where N is the total number of boundary unknowns. We demonstrate the high efficiency and robustness of PFFT-BEM by comparing the numerical its cost with conventional BEM for solutions of a canonical shallow water acoustics problem: Pekeris waveguide problem. To further improve the efficiency of the PFFT-BEM solver, we optimize the PFFT-BEM scheme by examining the accuracy dependence of the PFFT-BEM on key numerical parameters such as the size of the near field and the boundary mesh sizes. By making use of the Mesh-Neighbor-based (MN) preconditioner, we further improve the convergence of PFFT-BEM iterative for 2+ orders. With high performance library (e.g. PETSc and FFTW3), we implemente PFFT-BEM on massively parallel HPC platforms to

achieve linear CPU scalability up tp O(1000) CPUs. The PFFT-BEM could thus account for cases with: (a) Inhomogeneity of water properties. (b) Internal and surface waves. (c) Complex topography and lateral boundaries. (d) Multiple-scale reverberation/scattering by bottom and lateral boundaries and water surface. For the validity and applicability of PFFT-BEM, the performance of PFFT-BEM will be further studied using several benchmark solutions and acoustics scattering problems under realistic underwater conditions in the next chapter.

Chapter 3

Numerical validation/benchmark of the PFFT-BEM method

In this section, we first benchmark the PFFT-BEM method against available theoretical/numerical results: the Pekeris waveguide, the ASA wedge and Gaussian Canyon. Good agreements are obtained against available theoretical/numerical results which validate the accuracy of PFFT-BEM. Another goal of this chapter is to demonstrate the practical simulation capability of PFFT-BEM for 4D (3D+T) underwater acoustics scattering problems. As a result, the next part of this chapter is to illustrate the numerical capability of PFFT-BEM in the simulation of sound scattering variations due to the change of medium properties with time. Two cases are considered: (i) prediction of sound scattering by traveling internal waves; (ii) prediction of 3D sound scattering in the Mouth of the Columbia River.

3.1 Comparison with existing analytical and numerical results

3.1.1 Pekeris waveguide

Homogeneous ocean condition

We continue to use the Pekeris waveguide benchmark case. The computational domain is $10km \times 10km \times 100m$. The boundary element model consists of uniform quadrilateral element with edge length of Δl equals to $\lambda/8$ or $\lambda/12$. The numerical method computes the transmission loss (TL) along the range at depth of at $z = 46m$ and we compare it with the analytical results [Jensen et al., 2011] as shown in Fig.3-1(a). The numerical results compare well with the reference result which could validate our numerical method.The numerical results shows a clear convergence to the theoretical solutions when the Δl is decreased from $\lambda/8$ to $\lambda/12$. The total computational time for the Pekeris waveguide case with $\Delta l = \lambda/8$ is 276.3s with 16 computational nodes.

Inhomogeneous ocean condition: summer sound profile

In this subsection, we demonstrate the use of the PFFT-BEM to realistic range-dependent underwater acoustics problems. The same Pekeris waveguide is used but with the summer sound profile [Kuperman and Lynch, 2004]. The bottom is homogeneous with sound speed 1700m/s, density 1.5 g/cm^3 and medium attenuation $\alpha = 0.5dB/\lambda$. Fig.3-2 shows the spatial variations of sound speed in the water column. The sound frequency is 60Hz located at 70m below the sea surface. The computational domain is $2km \times 2km \times 100m$. The boundary element model consists of uniform quadrilateral element with Δl equals to $\lambda/8$. The numerical method computes the transmission loss (TL) along the range at depth of at z=70m.

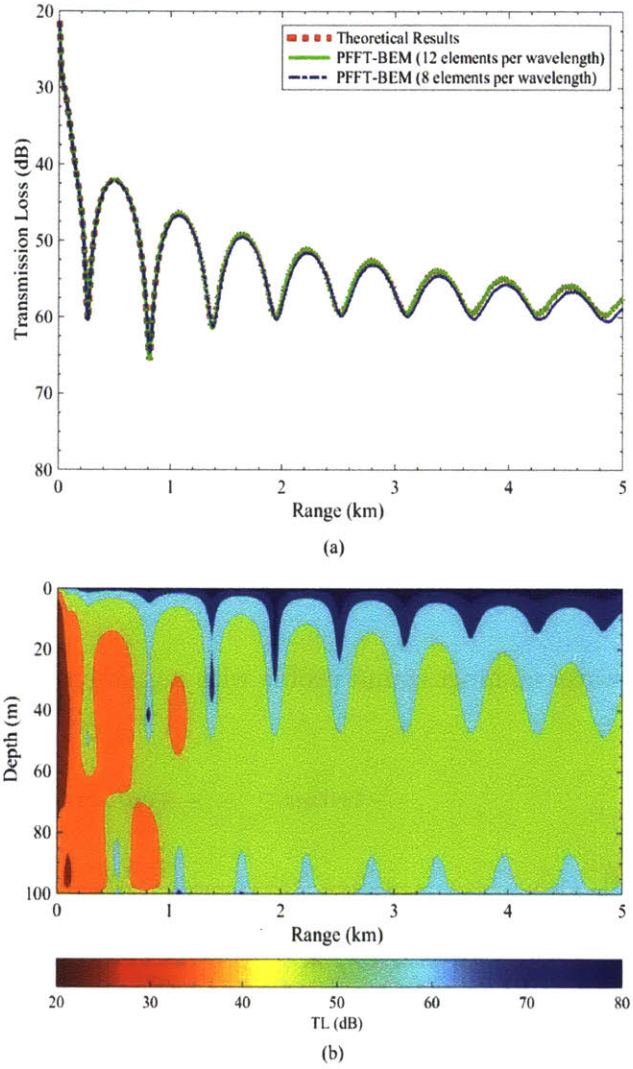

Figure 3-1: (a) Tranmission Loss (TL) at $z = 46m$ for $20Hz$ point source at 36m depth in the Pekeris waveguide: comparison between theoretical predictions[Jensen et al., 2011] and PFFT-BEM. (b) Contours of transmission loss vs. depth and range for $20Hz$ point source at $36m$ depth in the Pekeris waveguide

Since no theoretical results are available for validation, we show the convergence of the numerical results with respect to the number of layers used in PFFT-BEM. We consider four cases with different number of layers: (i) In the two layer case, the

sound speed is 1500m/s in z=0-100m region and 1700m/s in z>100m region.

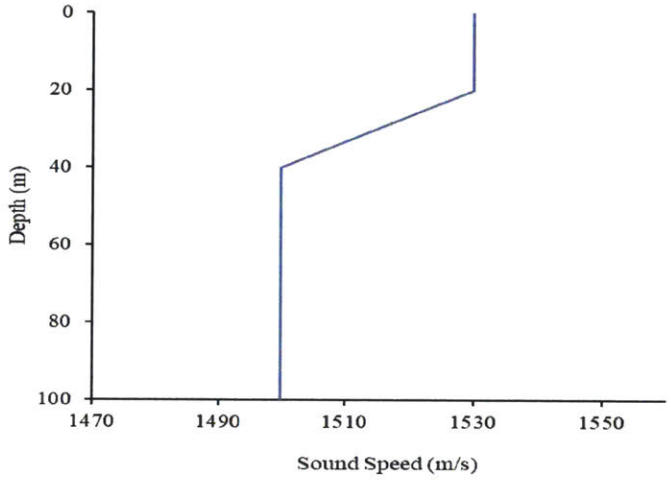

Figure 3-2: Shallow water summer sound profile with a gradient region at 20m∼40m.

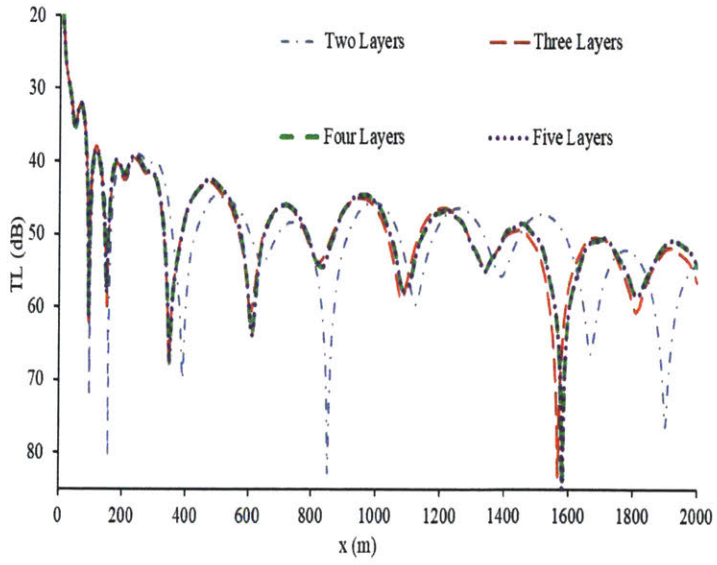

Figure 3-3: Tranmission Loss (TL) at z=70m for 60 Hz point source at 70m depth in the Pekeris waveguide with summer sound profile: comparison among PFFT-BEM results with different number of layers.

(ii) In the three layer case, the sound speed is 1530m/s in z=0-30m region, 1500m/s

in z=30-100m region and 1700m/s in z>100m region. (iii) In the four layer case, the sound speed is 1530m/s in z=0-20m region, 1515m/s in z=20-40m region, 1500m/s in 40-100m region and 1700m/s in z>100m region. (iv) In the five layer case, the sound speed is 1530m/s in z=0-20m region, 1520m/s in z=20-30m region, 1510m/s in 30-40m region, 1500m/s in 40-100m region and 1700m/s in z>100m region. After five layers is used, Fig.3-3 shows the numerical results converging with errors only in high TL region. This example demonstrates the use of PFFT-BEM for shallow water environment with inhomogeneous sound profiles.

3.1.2 Acoustical Society of America (ASA) wedge

An idealized wedge problem, shown in Fig.3-4, is used as the second benchmark problem. A $25Hz$ point source is located at $(x, y, z) = (0, 0, 100m)$. The wedge meets the free surface ($z = 0$) at $y = -4000m$. The computational domain size covers the range of $28km \times 8km \times 400m$. The water column is homogeneous with sound speed $c_1 = 1500m/s$, density $\rho_1 = 1g/cm^3$, and no medium loss. The bottom is also homogeneous with sound speed $1700m/s$ and medium attenuation $\alpha = 0.5dB/\lambda$. Two examples with bottom density equal to 1 or 1.5 g/cm^3, which corresponds to a fluid or soil bottom, are presented. The boundary element model uses quadrilateral element with $\Delta l = \lambda/8$ or $\lambda/12$.

In the first example, we consider the bottom density to be $1g/cm^3$. Fig.3-5(a) compares the numerical results of TL to the theoretical solution derived by Deane and Buckingham [1993] along $x-$axis at $z = 30m$. Excellent agreement between our 3D predictions and the theoretical solutions are observed in Fig.3-5(a). The total computational time for the first ASA wedge example with $\Delta l = \lambda/8$ is 3163s with 15 computational nodes (480 CPUs).

In the second example, we considered a bottom density of $1.5g/cm^3$ and kept the same computational domain size and resolution as the first ASA example. Once again, the comparisons of numerical TL along $x-$axis at $z = 30m$ to analytical results shown in Fig.3-6(a) are excellent. Using direct 3D boundary element simulations, we capture full 3D features as shown in Fig.3-5(b) and Fig.3-6(b) which is not generally

available using 2D numerical methods.

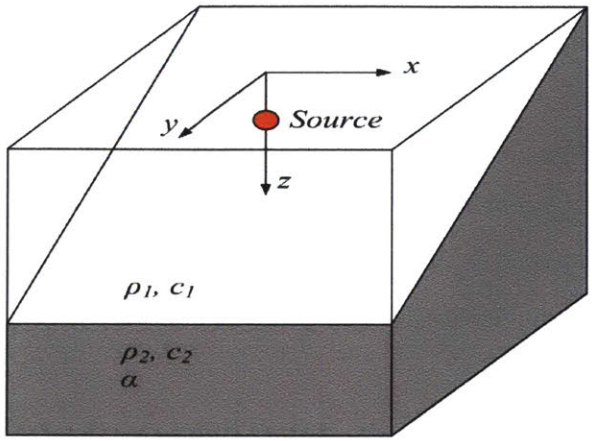

Figure 3-4: Geometry of the underwater ASA wedge, slope angle $\pi/63$. A 25Hz point source is located at (x,y,z)=(0,0,100m). The wedge meets the free surface (z=0) at y=-4000m.

The total computational time for the second ASA wedge example with $\Delta l = \lambda/8$ is 4113s with 15 computational nodes (480 CPUs).

To further demonstrate the code's capability to simulate higher frequency case, we simulated an ASA wedge case with source frequency $f = 75Hz$. The slope angle in this case is $\pi/36$, and the medium properties in the water column and the bottom are the same as the fluid bottom case shown above. The source is located $2km$ away from the wedge apex at depth $100m$. The computational domain size is $28km \times 4km \times 400m$. The element resolution are identical to the previous ASA wedge. The TL along the $x-$axis at $z = 30m$ and the TL contour on the horizontal $x - y$ plane at $z = 30m$ obtained from PFFT-BEM are shown in Fig.3-7(a) and Fig.3-7(b). In Fig.3-7(a), the numerical result compares very well with the theoretical result which demonstrates the efficiency and accuracy of the present method for higher frequency cases. The total computational time for the higher frequency ASA wedge with $\Delta l = \lambda/8$ is 22678s with 20 computational nodes (640 CPUs). It should also be noted that the numerical results show a clear convergence to the theoretical solutions when the Δl is decreased from $\lambda/8$ to $\lambda/12$ for all the three ASA wedges.

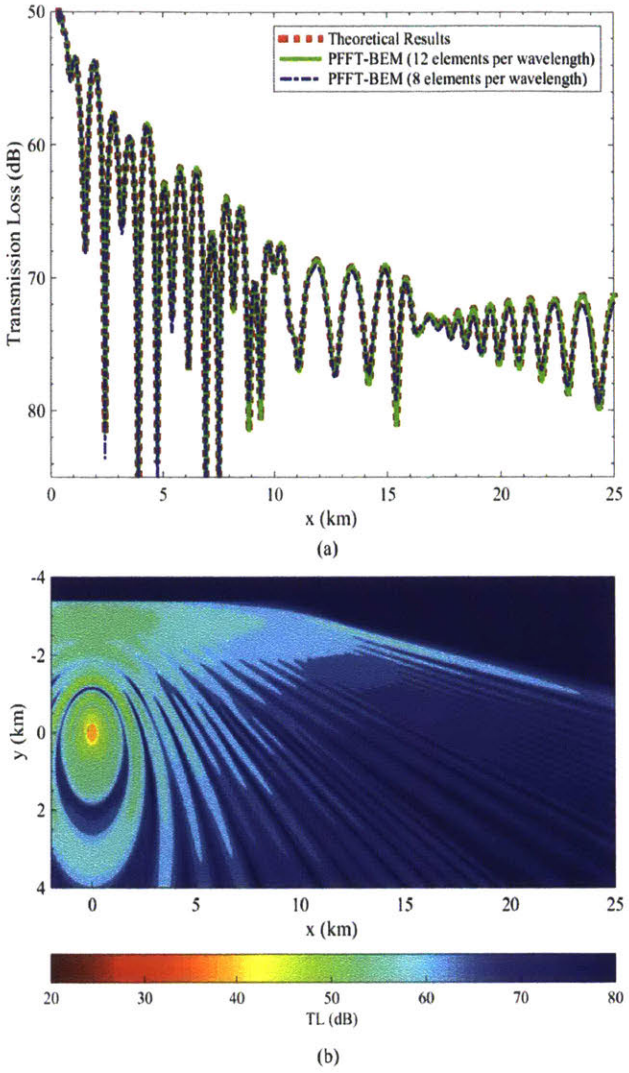

Figure 3-5: (a) TL along the $x-$axis at $z = 30m$ for ASA wedge: comparison between theoretical predictions by Deane and Buckingham [1993] and 3D direct simulations by PFFT. (b) TL obtained using PFFT-BEM on the $x-y$ plane at $z = 30m$. Case 1: source frequency $f = 25Hz$ with two water layers and both having the same density, $\rho = 1g/cm^3$, but different sound speeds, $c_1 = 1500m/s$, $c_2 = 1700m/s$. The bottom layer has a medium attenuation $\alpha = 0.5dB/\lambda$.

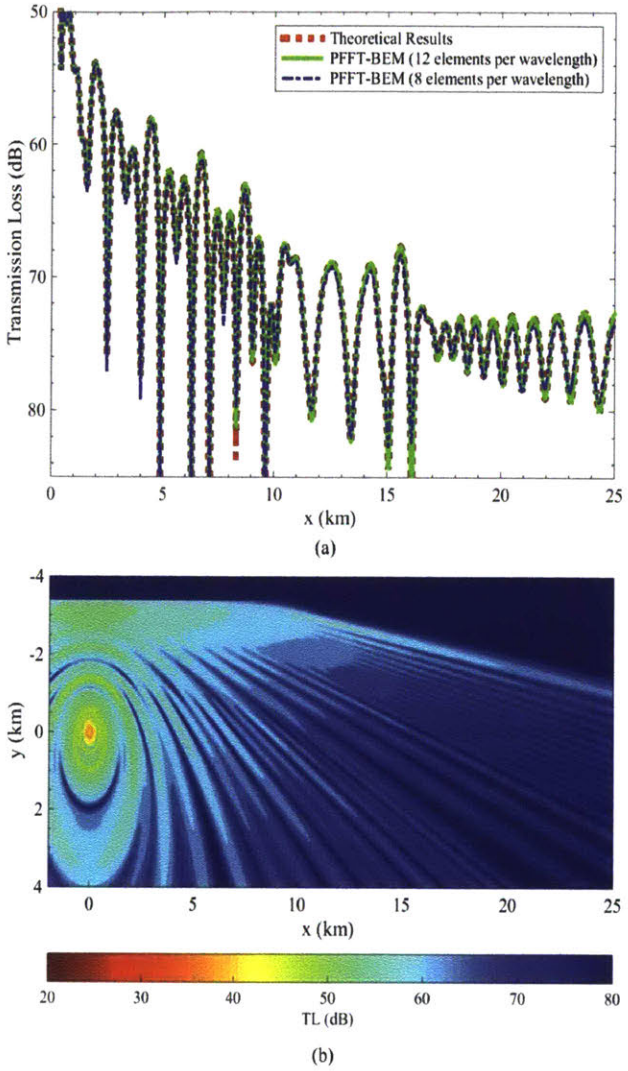

Figure 3-6: (a) TL along the $x-$axis at $z = 30m$ for ASA wedge: comparison between theoretical predictions by Deane and Buckingham [1993] and 3D direct simulations by PFFT. (b) TL obtained using PFFT-BEM on the $x - y$ plane at $z = 30m$. Case 1: source frequency $f = 25Hz$with upper water layer having $\rho_1 = 1g/cm^3$, $c_1 = 1500m/s$, on top of a soil bottom with $\rho_2 = 1.5g/cm^3$, $c_2 = 1700m/s$. The bottom layer has a medium attenuation $\alpha = 0.5dB/\lambda$.

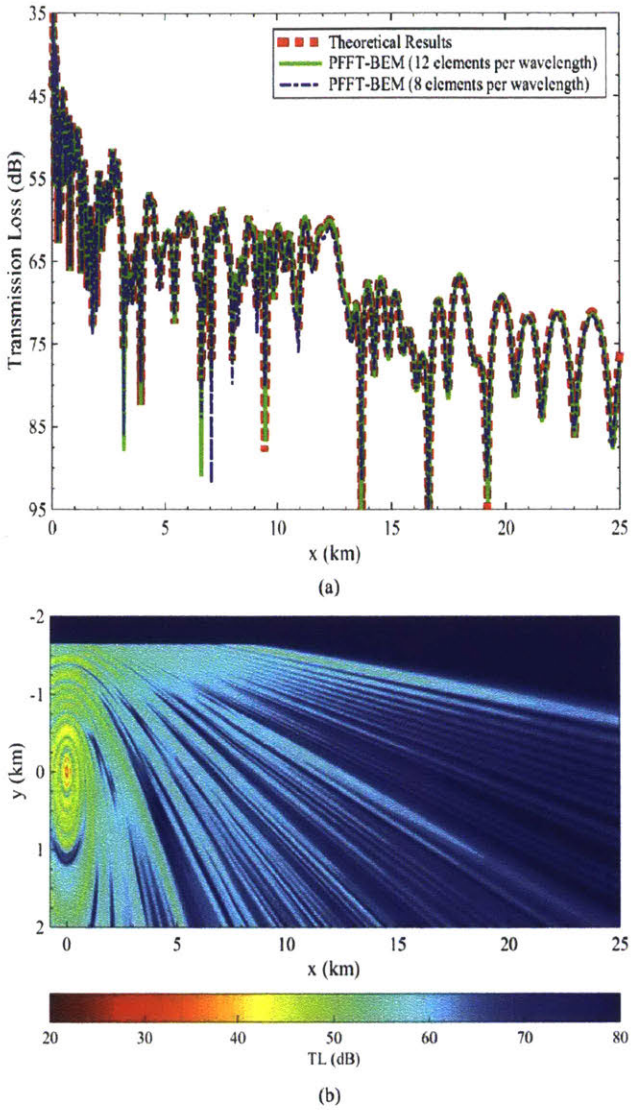

Figure 3-7: TL along the $x-$axis at $z = 30m$ for ASA wedge: comparison between theoretical predictions by Deane and Buckingham [1993] and 3D direct simulations by PFFT. (b) TL obtained using PFFT-BEM on the $x - y$ plane at $z = 30m$. Case 3: source frequency $f = 75Hz$ with upper water layer having $\rho_1 = 1g/cm^3$, $c_1 = 1500m/s$, on top of a soil bottom with $\rho_2 = 1.5g/cm^3$, $c_2 = 1700m/s$ and a medium attenuation $\alpha = 0.5dB/\lambda$.

3.1.3 3D Gaussian canyon

In the third benchmark problem, we consider a waveguide problem with Gaussian canyon with a pressure-release surface and a penetrable bottom. The water column has a depth of $700m$ with $c_1 = 1500m/s$ and $\rho_1 = 1.0g/cm^3$. A point source with f=25Hz with unit strength is placed at $(x, y, z) = (0, 0, 30m)$. The bottom has the properties as ρ_2=$1.5g/cm^3$, c_2=$1700m/s$ and α=0.5dB/λ. The geometry of the Gaussian Canyon bottom is defined as

$$z(x) = -200 - 500exp[-(x - 5000)^2/4] \tag{3.1}$$

where the coordinate system (x,y,z) is used and defined as shown in Fig.3-8.

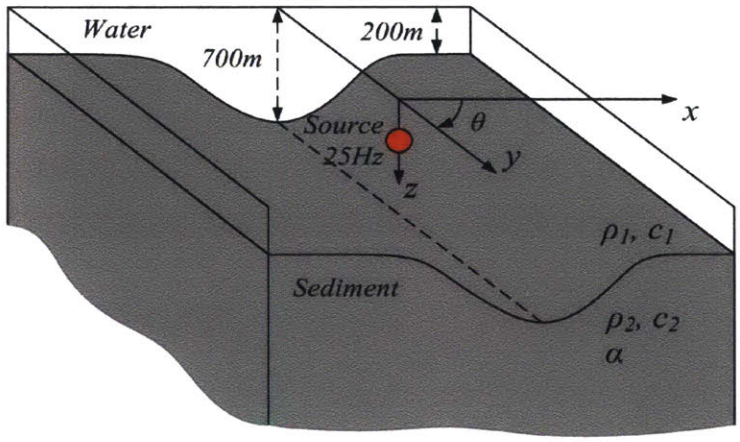

Figure 3-8: The geometry of the Gaussian canyon used in the present study with upper water layer having $\rho_1 = 1g/cm^3$, $c_1 = 1500m/s$, on top of a soil bottom with $\rho_2 = 1.5g/cm^3$, $c_2 = 1700m/s$ and a medium attenuation $\alpha = 0.5dB/\lambda$.

The computational domain size is $12km \times 23km \times 750m$. PFFT-BEM uses quadrilateral elements with $\Delta l = \lambda/8$. As the bottom is invariant along y-axis, the numerical results obtained by longitudinal invariant finite element method are used to compared with the 3D direct simulation results obtained by PFFT-BEM.

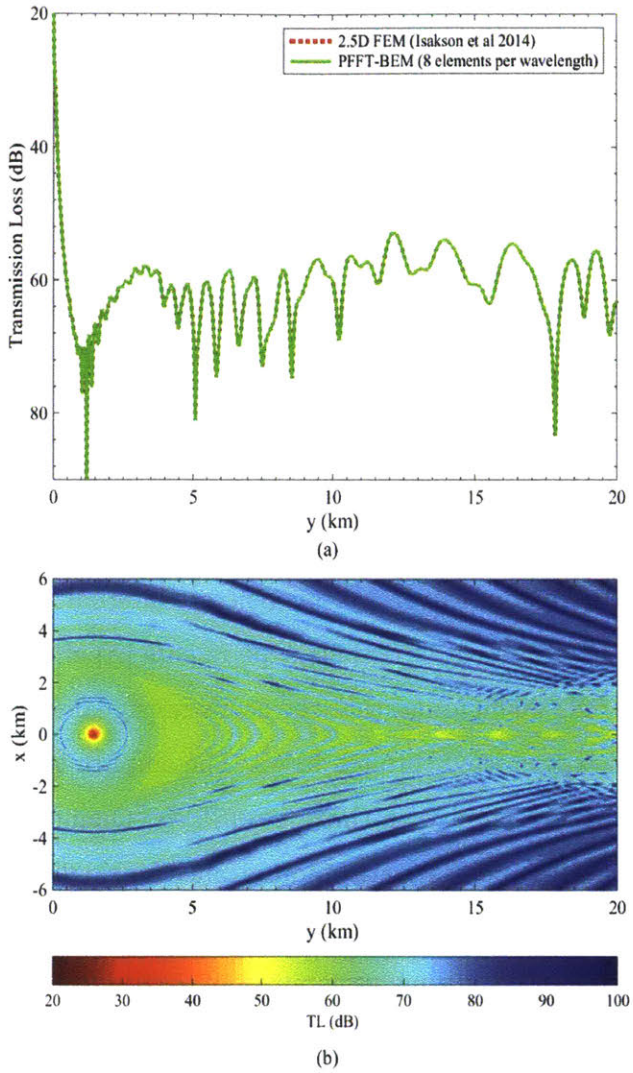

Figure 3-9: (a) TL along the $y-$axis at $z = 35m$ for Gaussian canyon: comparison between longitudinal invariant FEM predictions [Isakson et al., 2014] and 3D direct simulations by PFFT-BEM. (b) TL obtained using PFFT-BEM on the $x - y$ plane at $z = 30m$.

As shown in Fig.3-9, our numerical results compares well with the results obtained by the longitudinal invariant. The prediction by 3D direct PFFT-BEM agrees well with that by the 2.5D FEM method [Isakson et al., 2014] valid for longitudinal-invariant (2D) geometries. TL contour in the horizontal plane at the source depth is

also plot in Fig.3-9 in which significant 3D horizontal refractions could be observed. The total computational time for the low frequency seamount with $\Delta l = \lambda/8$ is 1hr with 20 computational nodes.

3.2 Comparison with experimental results

3.2.1 Prediction of 4D sound scattering by traveling internal waves

Tidal interactions with bottom features often generate internal solitary waves (ISWs) in the shallow water environment. Previous experiments [Apel et al., 1997, Headrick et al., 2000, Badiey et al., 2005] found that the acoustics signals would fluctuate when the sound waves were transmitted through ISWs. The amplitudes and phases of these fluctuations are highly correlated with the ones of ISWs. Quantifying the interaction between the acoustics wave and ISWs are of importance for shallow acoustics. In 1995, the multi-institutional SWARM'95 experimental was conducted on the New Jersey continental shelf and showed strong variability, of 7 dB, for a broad band signal propagation through ISWs [Apel et al., 1997, Headrick et al., 2000, Badiey et al., 2005]. A schematic diagram of the acoustics source and receiver position relative to the ISWs front during the experiment are plot in 3-10 (a) [Badiey et al., 2005].

During the interval 18:00 to 20:00 GMT on 4 August 1995, the source was placed at 12 m below the sea surface at the position about 15km from the receiver as shown in Fig.3-10 (b). The receiver was placed at 45m below the sea surface. The broadband source frequency f equals to 30$\sim$160Hz with 3 peak frequencies at 30Hz, 60Hz and 90Hz. Using PFFT-BEM, we simulate the propagation of the acoustics waves through the internal waves. As shown in Fig.3-10 (b), a three layer condition is used in 3D PFFT-BEM direct numerical simulation. The properties of the water column and sea bottom is based on the data from Badiey et al. [2005].

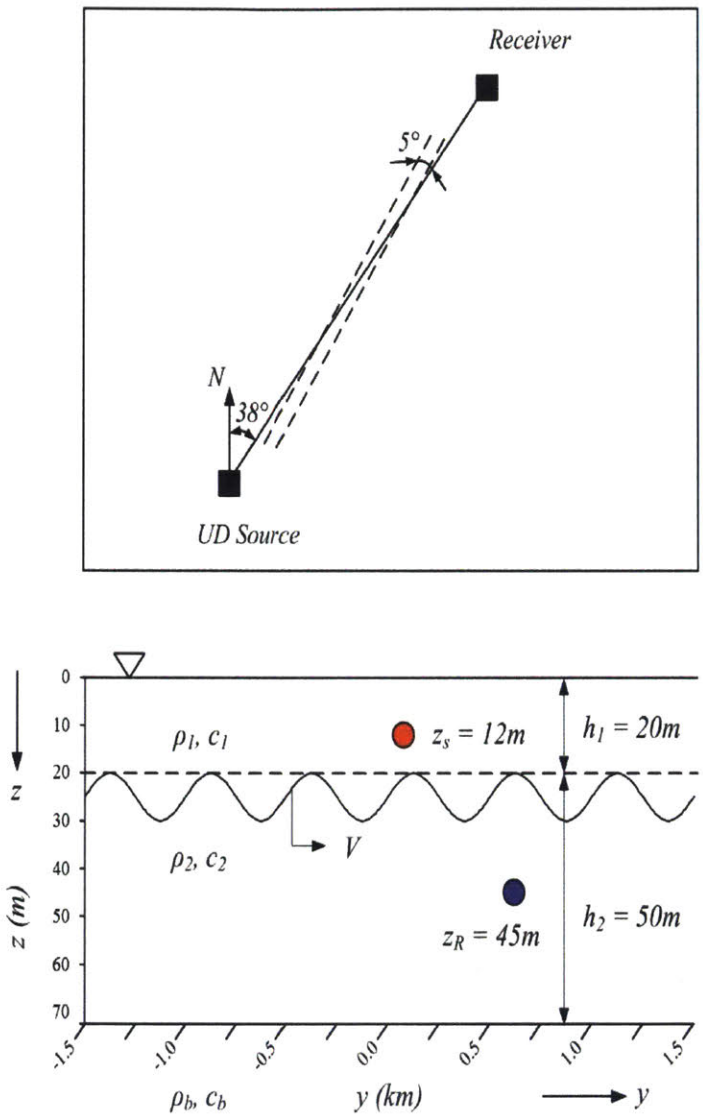

Figure 3-10: (a) Field experiment arrangement of the source/receiver and their relative position with respect to the internal wave fronts [Badiey et al., 2005] (b) Parameters of PFFT-BEM simulation (oblique sea condition): upper water layer with ρ_1=1.024g/cm^3, c_1=1530m/s, lower water layer with ρ_2=1.0257g/cm^3, c_2=1480m/s and the bottom layer with ρ_b=1.8g/cm^3, c_b=1750m/s and α=0.4375dB/λ

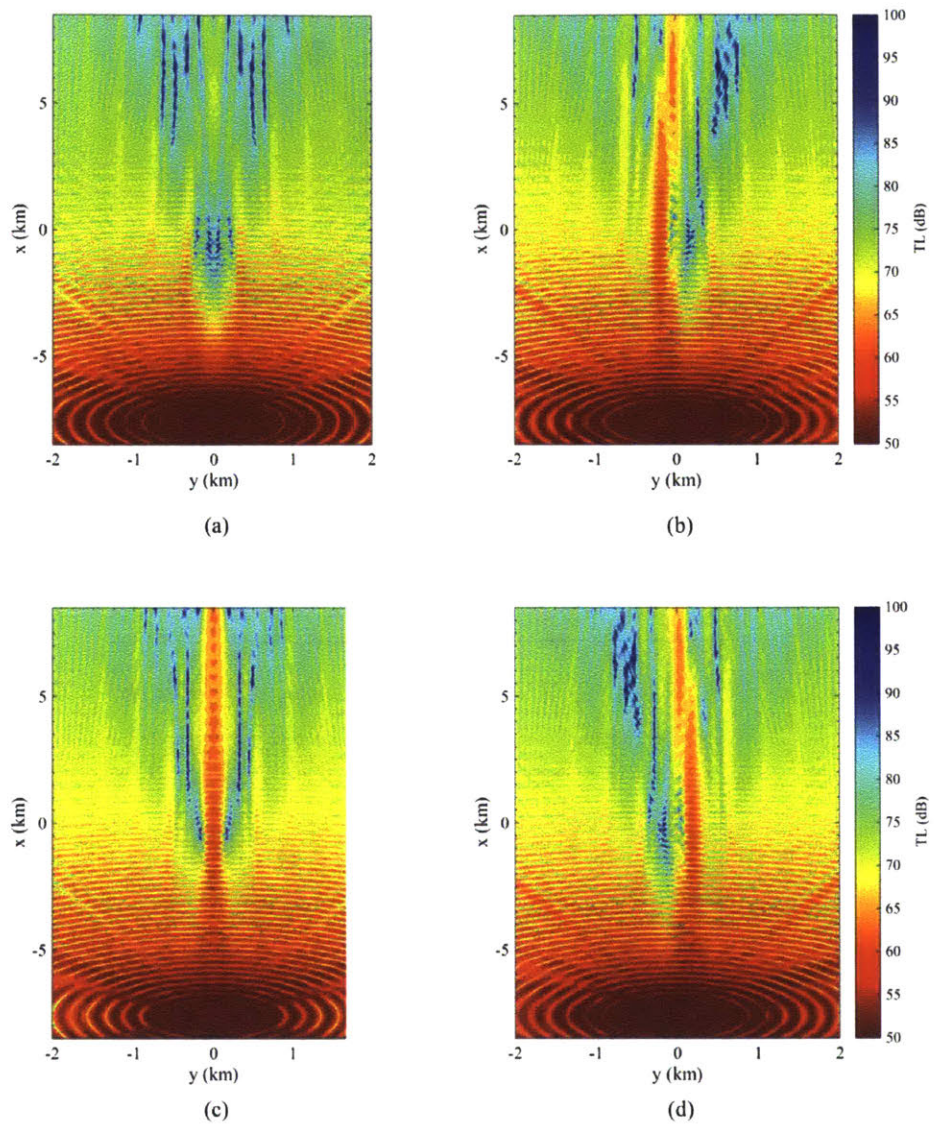

Figure 3-11: TL in the horizontal plane at receiver depth $z = 45m$ obtained by 4D PFFT-BEM direct numerical simulation with (a) t=0 (b) t=1/4T_{int} (c) t=1/2T_{int} (d)3/4T_{int}

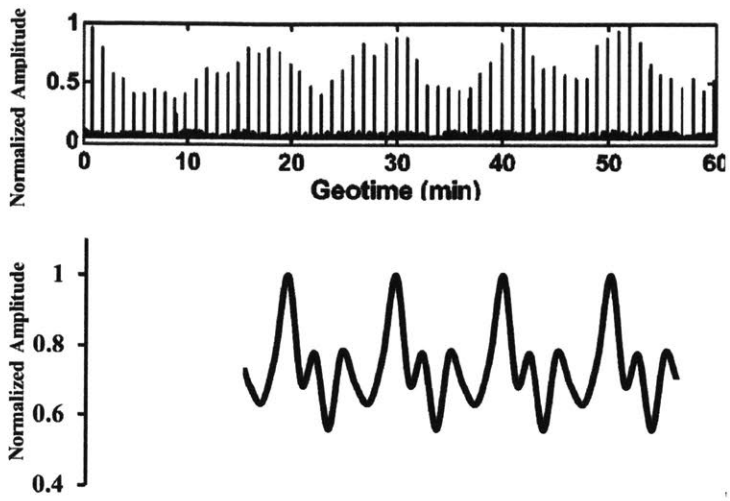

Figure 3-12: (a) Field normalized acoustics pressure data [Badiey et al., 2005] with source $f = 30 \sim 160Hz$ and irregular internal waves. (b) Normalized acoustics pressure predicted by 4D PFFT-BEM with sound frequency $f = 60Hz$ and regular internal wave with amplitude η as $\eta = 10sech^2[(y - c_{int}t)/70]$, where c_{int} is the internal wave phase velocity equals to 0.65 m/s [Badiey et al., 2005]

The sound speed and density of the upper layer in the water column are c_1=1530m/s, ρ_1=1.024g/cm^3. The sound speed and density of the lower layer in the water column are c_2=1480m/s, ρ_1=1.0257g/cm^3. The properties of the bottom are c_b=1750m/s, ρ_b=1.8g/cm^3 with attenuation parameter α=0.4375 dB/λ. The shapes of the ISWs are based on the model proposed by Badiey et al. [2005] as

$$\eta = 10sech^2[(y - c_{int}t)/70] \tag{3.2}$$

where η is the height of the internal waves. The phase velocities of the ISWs are c_{int}=0.65 m/s. Here, we ignore the differences between the speeds of separate solitary waves. As a result, the whole internal wave train is assumed to move at the same speed. The sound source frequency used in 3D PFFT-BEM is selected to be 60 Hz. To demonstrate the acoustical scattering effects of the internal waves, we plot the transmission loss in x-y plane at the receiver depth over one internal wave period. As

shown in Fig.3-11, transmission loss obtained using 3D multi-layer PFFT-BEM shows strong variability as internal wave train moves, consistent qualitatively with the field experiments (e.g. Headrick et al. [2000], Badiey et al. [2005]). We then compare the acoustics pressure calculated using 3D PFFT-BEM at the receiver with the field measurement during a two-hour period (18:00 to 20:00 GMT on 4 August 1995). As shown in Fig.3-12, numerical prediction by PFFT-BEM agrees qualitatively well with field experimental data on the trend of time variation and magnitude of fluctuation of received sound pressure.

3.2.2 Prediction of 3D sound scattering in the mouth of the Columbia river

Experimental description and observations

The salt wedge often occurs in the estuarine environment. It happens when the fresh river water flows directly into salt water in the ocean. Advection of the salt and fresh water often happens during this process. Accurate monitoring and modeling of the salt wedge advection is important for the understanding of several coastal processes [Reeder, 2016]. In 2014, a field experiment was carried out in the Mouth of the Columbia river, which spanned from several kilometers west of the North Jetty and South Jetty at the river mouth to points just west to the A-M bridge in the North Channel as shown in Fig.3-13 [Reeder, 2016] . In this thesis, we are concentrating on the time period during the period: 20130527 at 16Z-21Z as the sound speed gradients are the strongest during this period. This period is corresponding to the retreat of the fresh water (or advance of the salt water) in the estuary. The acoustic source (S2 in Fig.3-13) located 7 m below the surface transmitted acoustics signal to a receiver system (A5 in Fig.3-13). The experiment uses a linear modulated acoustics signals in 500-2000Hz band. The distance between the source and receiver is 1.36km. The receiver is 1m above the seabed. Fig.3-14(a) shows the sound speed versus depth at the source location during the period of interest. The sound energy level during the experiment, which measures the sound energy and related to the sound pressure p as

SEL $\sim \log |p|^2$, was given by Reeder [2016] as shown in Fig.3-14(b). The SEL is stable before the salt water entrance then slowly decreases approximately 15dB during the advection of the salt and fresh water. Then during an one hour period afterwards, SEL increases 15dB back to the same level before the salt water entrance.

Numerical modeling and comparison with experiments

In this subsection, we use 3D multi-layer PFFT-BEM to compute the acoustics pressure at the receiver A5 with and without the salt wedge. We modeled the estuarine environment with the bottom geometry and the sound speed based on the measurement from Reeder [2016]. The sound frequency was selected to be a signal frequency f=500Hz. Before the entrance of the salt wedge (fresh water only), the acoustic transect is composed of nearly isospeed fresh waters with c_1=1460m/s and ρ_1=1.0g/cm^3. The bottom has the properties as c_b=1620m/s, ρ_b=1.83g/cm^3, and attenuation α of 0.365 dB/m [Sherwood and Creager, 1990]. As the salt wedge entrance to the estuary, PFFT-BEM uses a three layer condition in the seawater with c_1=1460/s from z=0$\sim$14m,c_2=1470m/s from z=14$\sim$15m and c_3=1490 from z>15m. Comparing the 3D numerical results in the xz plane of Fig.3-15(a) and (b), we observed that the acoustics waves were trapped at the upper layers of the seawater and the transmission loss at the receiver increases by 7dB which is consistent with the 2D numerical results conducted by 2D Bellhop [Porter and Bucker, 1987] in Reeder [2016].

However, the actual increase in the experiment is nearly 10$\sim$15dB which is not fully observed in the numerical results. Many reasons may be accounted for this difference such as the change of the geoacousitc parameters during the experiment, the errors in the measurement of the sound speed and free surface wave effects. Here we focus on the effect of free surface waves and simulated the acoustics wave propagation with and without free surface waves.

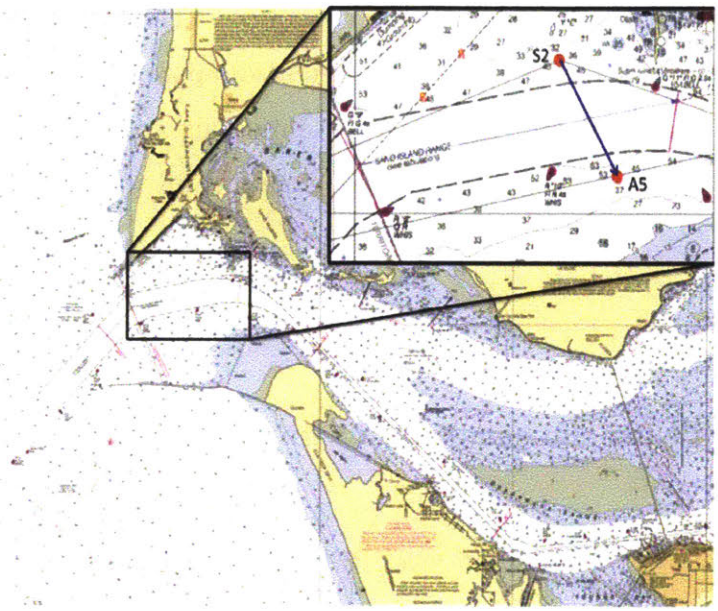

(a)

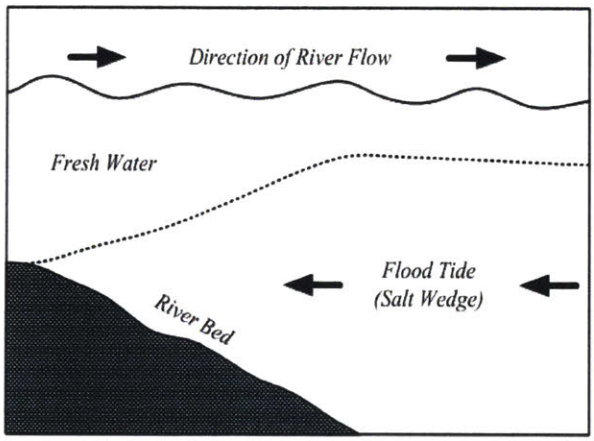

(b)

Figure 3-13: (a) Mouth of the Columbia River: station S2 where the acousitc source was placed, and station A5 where the receiver was placed 1m above the riverbed. The acoustics transect was 1.36km long [Reeder, 2016]. (b) A sketch of the side view of the flood tide (salt wedge) entrance the fresh water and the wave generated by the interaction between the fresh water and flood tide.

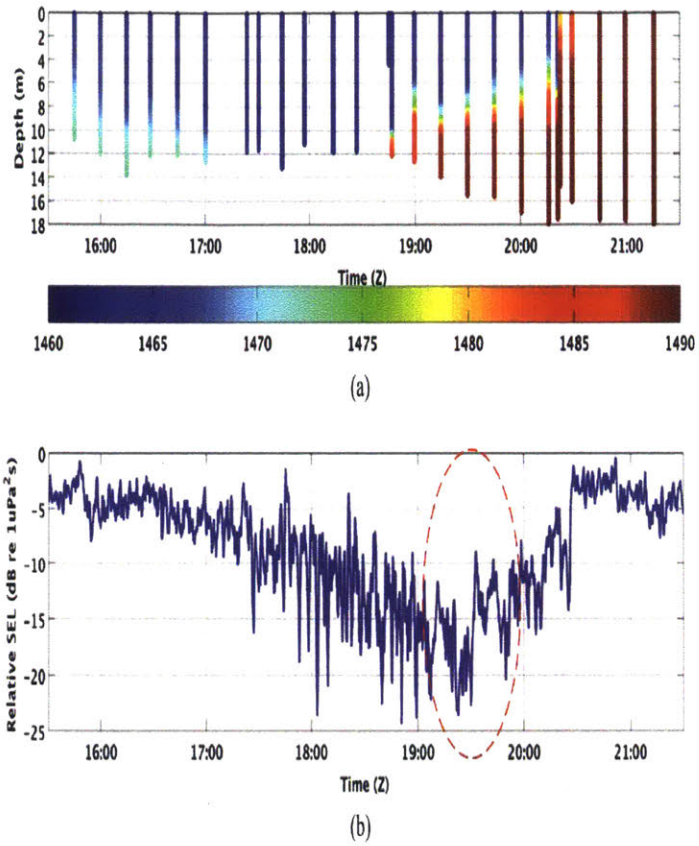

Figure 3-14: (a) The sound speed (m/s) vs depth at time (Z) at receiver during the 6h period of the acoustic transmission [Reeder, 2016]. (b)The SEL measure at the receiver during the flood period [Reeder, 2016].

As indicated by Thomson et al. [2014], very rough surface conditions can be produced via wave-current interactions. As shown in Fig.3-15(c), we include a regular free surface wave based on a sinusoidal function as:

$$\eta = \eta_0 \sin(kx) \tag{3.3}$$

where A_0=2m, 3m and 4m, and k=0.045m^{-1} based on the field measurement by Thomson et al. [2014] during the entrance of salt wedge. Fig.3-15(c) shows an example with A_0= 4m. Significant scattering effects from surface waves are found by direct numerical simulations. When including the surface waves, the increase of the TL data

comparing with fresh water cases changed to 11dB$\sim$18dB which confirming the field measurement data.

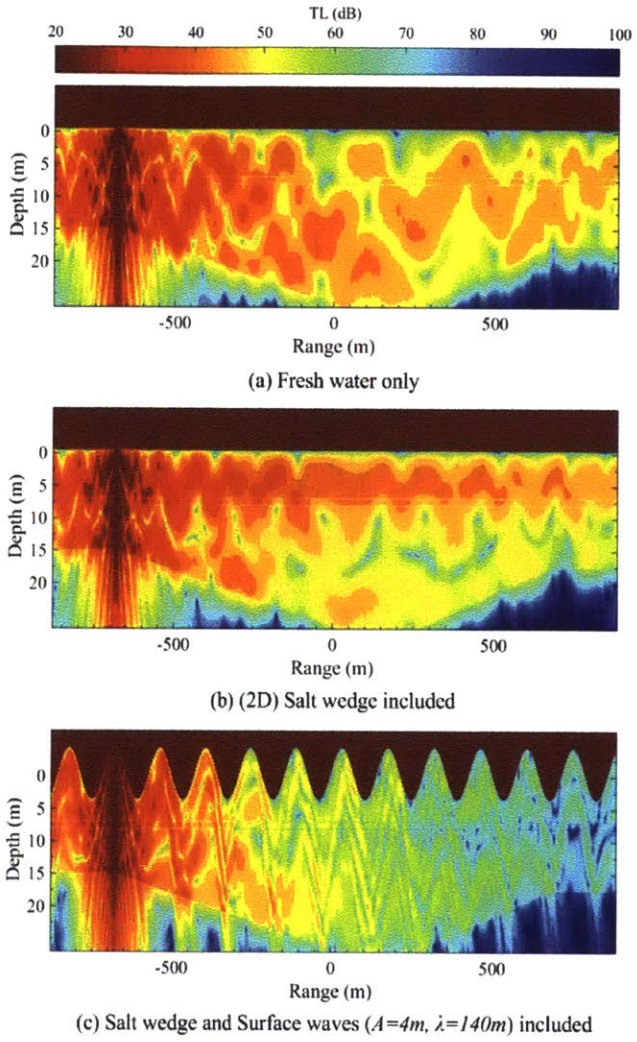

Figure 3-15: PFFT-BEM prediction of the transmission loss using 500Hz frequency and realistic geometry and acoustic environment: (a) Fresh water case, c_1=1460m/s, c_b=1620m/s and α=0.365dB/m in the bottom. (b) Salt wedge only, c_1=1460m/s, c_2=1470m/s, c_3=1490m/s, c_b=1620m/s and α=0.365dB/m in the bottom. (c) Salt wedge and free surface waves with amplitude A=4m, c_1=1460m/s, c_2=1470m/s, c_3=1490m/s, c_b=1620m/s and α=0.365dB/m.

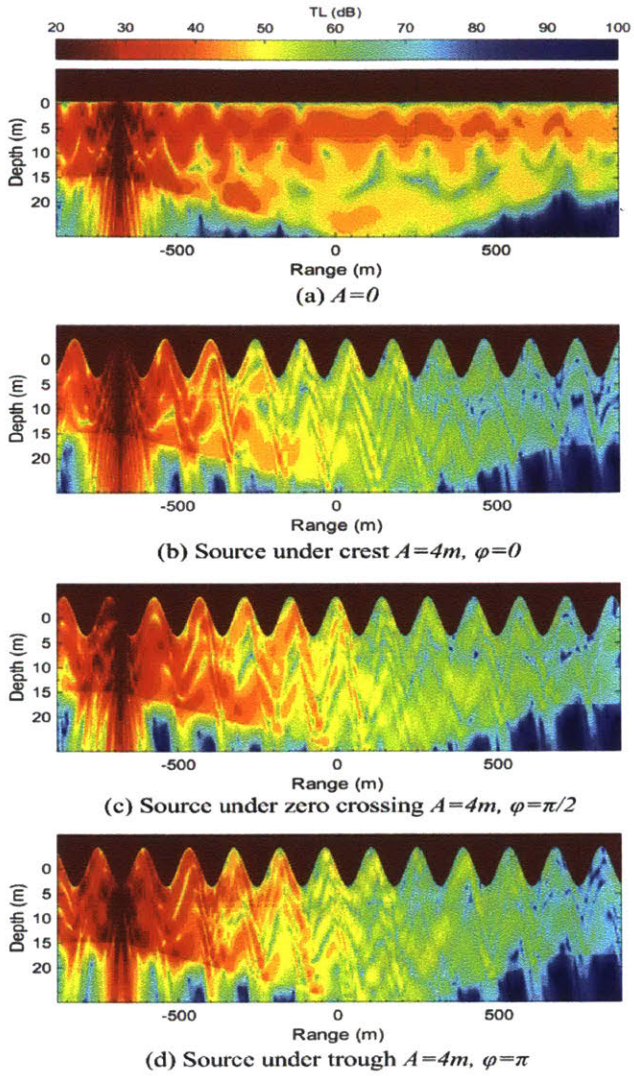

Figure 3-16: PFFT-BEM prediction of the transmission loss using 500Hz frequency and realistic geometry and acoustic environment with different surface wave phases relative to the sound source: (a) Calm water with salt wedge A=0, c_1=1460m/s, c_b=1620m/s and α=0.365dB/m in the bottom. (b) Salt wedge with head sea surface wave amplitude A=4m, sound source located under the surface wave crest with c_1=1460m/s, c_2=1470m/s, c_3=1490m/s, c_b=1620m/s and α=0.365dB/m in the bottom. (c) Salt wedge with head sea surfacewave amplitude A=4m, sound source located under the surface wave zero crossing. (d) Salt wedge with head sea surface wave amplitude A=4m, sound source located under the surface wave trough.

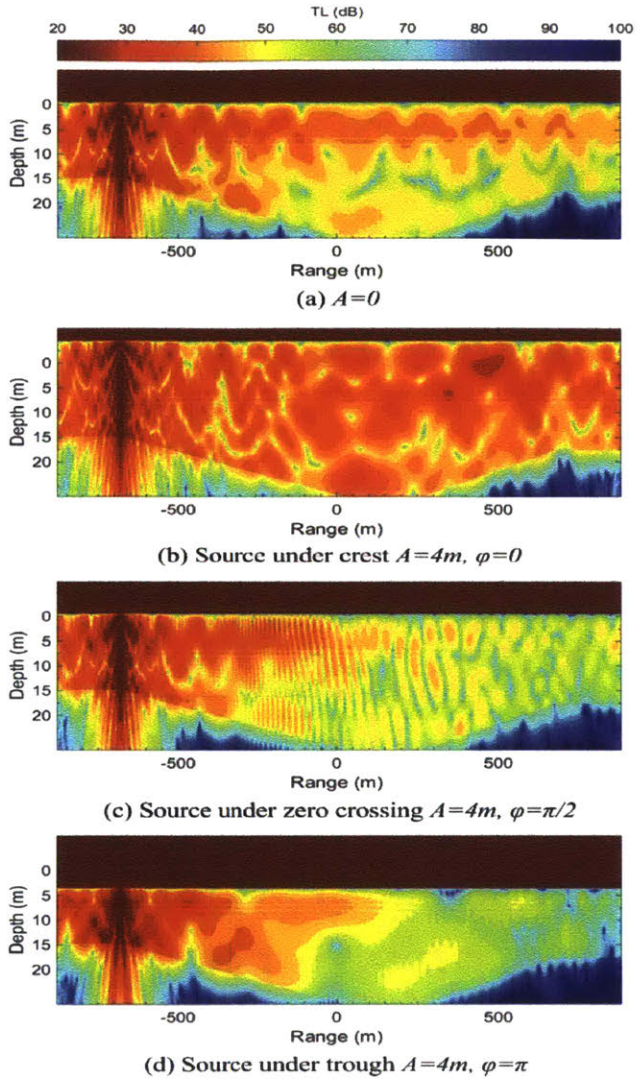

Figure 3-17: PFFT-BEM prediction of the transmission loss using 500Hz frequency and realistic geometry and acoustic environment with different surface wave phases relative to the sound source: (a) Calm water with salt wedge A=0, c_1=1460m/s, c_b=1620m/s and α=0.365dB/m in the bottom. (b) Salt wedge with beam sea surface wave amplitude A=4m, sound source located under the surface wave crest with c_1=1460m/s, c_2=1470m/s, c_3=1490m/s, c_b=1620m/s and α=0.365dB/m in the bottom. (c) Salt wedge with beam sea surface wave amplitude A=4m, sound source located under the surface wave zero crossing. (d) Salt wedge with beam sea surface wave amplitude A=4m, sound source located under the surface wave trough.

We further investigate the effect of the relative position of surface waves and the source point. As shown in Fig.3-16, we simulated cases with source located under free surface wave crest, zero crossing and trough. Comparing the the calm water case (A=0m), TL increased 9 $\sim$ 15dB for different surface wave phases. This indicates the effects of wave phase are relatively small for head seas.

The surface wave direction is another important parameters influencing the scattering effects by the surface waves. Here, we considered the scattering effect due to beam seas surface waves (i.e. surface wave front parallel to the acoustic insect). Different surface wave phases of the beam wave are considered and compared in Fig.3-17. From the direct numerical results, we found significant variation of TL (-10dB$\sim$+8dB) due to presence of beam seas waves. Different with the head sea condition, the relative surface wave phase has a major effect on TL for beam seas. Trough comparison among numerical simulation with calm fresh water, with only salt wedge and with both salt wedge and surface waves, we demonstrate the importance of the surface waves/roughness on the acoustics scattering. The 3D sound scattering effects due to rough surfaces will be further discussed in Chapter 4.

3.3 Concluding remarks

We develop and apply a highly efficient numerical capability using PFFT-BEM for direct solution of full 4D sound-wave equations without fundamental approximations. First of all, multiple coupled domain boundary-element method (MCD-BEM) is formulated based on the continuity of normal velocity and pressure at the domain interface to account domain inhomogeneity. Secondly, using pre-corrected Fast Fourier Transform (PFFT), PFFT-BEM reduce the computational (and memory) cost from $O(N^{2\sim3})$ to $O(N \log N)$, where N is the total unknown number.

For validation, this chapter first presents study of three sample three-dimensional underwater acoustic propagation and scattering problems: Pekeris waveguide problem, ASA wedge problem and the Gaussian canyon problem. For all these problems, the PFFT-BEM simulation results compare well with existing theoretical and numerical results. Good agreement are also obtained between the 3D+T simulation results and the experimental data for internal wave and salt wedge cases which involves realistic boundary and medium conditions. This demonstrates the practical simulation capability of PFFT-BEM for 4D (3D+T) underwater acoustics scattering problems. The computational times for all the cases presented in this chapter are listed in Table 3.1.

Table 3.1: Computational time for validation/benchmark casses

case name	f(Hz)	L_x, L_y, H(km)	N	N_cpu	t (hrs)
3D Pekeris waveguide	20	10, 10, 0.1	1×10^7	512	0.08
40 Hz seamount	40	2.5, 2.5, 0.25	2×10^7	384	0.08
Gaussian Canyon	25	12, 23, 0.75	5×10^8	640	1
25Hz ASA wedge	25	28, 8, 0.4	2×10^8	640	1
MCR (with surface waves)	500	1.7, 0.5, 0.03	1×10^8	960	4
Internal wave simulation	60	17, 5, 0.07	2×10^8	512	6
75 Hz ASA wedge	75	28, 4, 0.4	3×10^9	960	6

Chapter 4

Study on the 3D scattering by rough surface

A direct three dimensional (3D) numerical method based on Pre-corrected Fast Fourier Transform (PFFT) approach Boundary Element Method (BEM) has been developed. The validity of the PFFT-BEM in computing shallow water acoustics has been presented. In this chapter, the PFFT-BEM is used to study 3D acoustics scattering from a random rough surface with Gaussian roughness spectrum, satisfying the pressure release (Dirichlet) boundary condition. PFFT-BEM, which reduces the computational effort from $O(N^{2\sim3})$ to $O(N \log N)$ where N is the total number of boundary unknowns, could effectively eliminate the edge effect by using large computational domain size. By the use of PFFT-BEM method, we perform a Monte Carlo computation to obtain the acoustics scattering cross section: we first obtain the scattering pressure from one surface realization and then average over 50 realizations. Due to the high computational cost for direct numerical simulations, previous studies have proposed several approximate models for rough surface scattering problems such as the Kirchhoff approximation, first and second order perturbation theories. By combing with propagation models such as PE method and ray tracing methods, these approximate models simulate reverberations/scatterings by bottom and water surface. However, the validity of these approximate models, especially for 3D problems, is still questionable due to the large computational cost. By comparing the approximate model

results with the direct numerical simulation results by PFFT-BEM, we obtain the validity regions of these approximate models for 3D rough surface scattering problems for a wide region of grazing angles θ_g (Here, θ_g is defined as the angle between the incident plane wave and the mean rough surface). By 3D direct numerical simulations, we demonstrate and discuss the acoustics wave grazing angle effects on the validity regions of the approximate models especially near the backscattering direction.

4.1 Introduction

Accurate prediction of acoustics scattering from rough surfaces is of importance in modeling the reverberation and forward scattering problems. Kichhoff approximate model and perturbation theory are the most well-known and widely used approximate models for rough surface scattering problems due to their capabilities in providing fast prediction of statistics of rough surface scatterings.

The Kirchhoff approximation is based on flat surface assumption and generally apply to gently undulating surfaces where the radius of surface curvature is large compared to the acoustics wavelength. However, from previous 2D studies [Thorsos, 1988], it has been shown that Kirchhoff approximation is usually considered suspect at low grazing angles and for backscattering in general. The main reason is that the shadowing effect from the rough surface has not been taken into account in the Kirchhoff approximations.

Perturbation theory is another widely used approximate model for treating acoustics scattering from rough surfaces. The perturbation model is valid when $kh << 1$. Here h is the rms surface height and k is the acoustic wavenumber. In addition, according to Thorsos and Darrell [1989], when kh is fixed, the perturbation theory becomes inaccurate if kl, where l is the surface correlation length, is too large or too small. An explanation for this behavior can be found in Thorsos and Darrell [1989] by theoretically comparing the first and second order perturbation formulations.

Although the validities of Kirchhoff and perturbation approximations for 2D scatterings have been demonstrated and tested by direct numerical studies [Thorsos,

1988, Thorsos and Darrell, 1989, Kaczkowski et al., 1994, Thorsos et al., 2000, Isakson et al., 2008, Joshia and Isakson, 2011], no procedure has yet existed for estimating the approximate model errors in scatter strength for 3D scatterings. Therefore, the applications of perturbation and Kirchhoff approximations for 3D cases still need to be analyzed carefully. The challenge for direct numerical simulation to study the rough surface scattering problem is the difficulty to eliminate the edge effects, that is, scatterings from the ends of the truncated computational domain. A tapering incident wave such as Gaussian and Thorsos taper is usually used. The simplest and most popular tapered incident wave is a plane wave modulated by a Gaussian taper function. Unfortunately, Gaussian taper incident field only satisfies the Helmhotz equation for normal grazing angle cases [Toporkov et al., 1999]. Thorsos and Darrell [1989] derived a modified Gaussian tapered incident wave. The form of this tapered incident wave satisfies the Helmholtz wave equation more closely.And the criteria for the Thorsos taper to satisfy the Helmhotz equation is $kg\sin(\theta_g) >> 1$ where g controls the tapering size of the domain (with $g = \frac{1}{4}L$ in Thorsos [1988]). As a result, when $\theta_g << 1$ which corresponds to a low grazing angle problem, g and L needs to be $>> 1$ to satisfy the criteria $kg\sin(\theta_g) >> 1$.

For such a problem, the computational costs for 3D direct numerical methods such as Finite element method (FEM)/Finite Volume Method (FVM)/Spectral Element Method (SEM) are very large due to the requirements on meshing the 3D volume of the computational domain. On the other hand, for boundary element method (BEM), the Helmholtz boundary-value problem can be formulated as a boundary integral equation (BIE) [Burton and Miller, 1971], for which only the unknown pressures or the normal pressure gradients on the domain boundaries are solved for. As a result, BEM only requires the meshing of the domain boundaries. By the use of PFFT, we further reduce the overall computational efforts of BEM from $O(N^{2\sim3})$ to $O(N\log N)$, where N is the number of unknowns on the domain boundaries. Because of these advantages, PFFT-BEM is particularly suitable for studying rough surface scattering problems.

In this chapter, we implement PFFT-BEM to obtain direct numerical solutions of

general 3D acoustics rough surface scattering problems. Since the objective here is to examine the validities of these approximate models, we choose to use the pressure-release surface condition with Gaussian roughness spectrum for which 2D and 3D approximation solutions can be obtained easily [Thorsos, 1988, Thorsos and Darrell, 1989, Kaczkowski et al., 1994, Thorsos et al., 2000, Isakson et al., 2008, Joshia and Isakson, 2011]. For each of 50 surface realizations consistent with the Gaussian spectrum, the scatted pressure in the far field, which is a function of the scattering angle for a specified grazing angle, is computed numerically by 3D PFFT-BEM method. The scattering cross section σ and the scattering strength defined as $10\log_{10}\sigma$ are found from the average scattered intensity. From numerical results, we assess the validity and applicable of Kirchhoff and perturbation approximation for 3D scattering problems. Low angle grazing effects down to 2.5° are also simulated and discussed at last.

4.2 Mathematical formulations

4.2.1 Boundary-value problem for plane wave scattering

We first formulate the boundary-value problem for plane wave scattering by a pressure release surface in this section. We choose a Cartesian coordinates system Oxyz with O-xy in the horizontal plane of the mean ocean surface and Oz pointing vertically up. $z = \eta(x, y)$ describes the surface roughness. The acoustics pressure $p(\vec{x})\exp(-2\pi ft)$ in the fluid domain satisfies Helmhotz equation as

$$\nabla^2 p(\vec{x}) + k^2 p(\vec{x}) = 0, \qquad \vec{x} \in V \tag{4.1}$$

where f is the sound frequency, ∇ denotes the gradient operator, V is the entire fluid domain, and k the medium wavenumber.

The problem is subject to the pressure release boundary condition at the free surface S_F:

$$p(\vec{x}) = 0, \qquad \vec{x} \in S_F \tag{4.2}$$

and the condition at the far-field boundary S_∞ is:

$$p(\vec{x}) = p_i, \quad \vec{x} \to \infty \tag{4.3}$$

where p_i is the incident wave expressed as

$$p_i(x, y, z) = e^{ik(xsin(\theta_i)cos(\phi_i)+ysin(\theta_i)sin(\phi_i)-zcos(\theta_i))} \tag{4.4}$$

where $\theta_i = \pi - \theta_g$ and ϕ_i is the angle between the horizontal component of the incident wave (in the xy plane) and the x-axis. The grazing angle θ_g is defined with $\theta_g = \frac{\pi}{2} - \theta_i$. θ_s is the angle between the scattering plane wave and the mean rough surface. ϕ_s is the angle between the horizontal component of the scattering wave (in the xy plane) and the x-axis. Here, we define the coordinate system such that ϕ_i=0° (i.e. $\mathbf{K_i} \equiv (k_{ix}, 0)$). This completes the statement of the boundary-value problem. From Green's second theorem, we formulate the boundary integral equation (BIE) for the pressure $p(\vec{x})$ as

$$4\pi p(\vec{x}) - \iint_S p_n(\vec{\zeta})G(\vec{x};\vec{\zeta})dS(\vec{\zeta}) + \iint_S p(\vec{\zeta})G_n(\vec{x};\vec{\zeta})dS(\vec{\zeta}) = 0 \tag{4.5}$$

where S is the fluid domain boundaries. Here, $G(\vec{x};\vec{\zeta}) = |\vec{x} - \vec{\zeta}|^{-1}e^{ik|\vec{x}-\vec{\zeta}|}$ is the Green function which satisfies the Helmholtz equation, and $\vec{\zeta}$ is any point on S. Then the total acoustic pressure $p(\vec{x})$ due to sound scattering from a pressure release rough surface can be expressed as

$$p(\vec{x}) = p_i(\vec{x}) + \frac{1}{4\pi}\int_{S_F} p_n(\vec{\zeta})G(\vec{x};\vec{\zeta})dS(\vec{\zeta}) \tag{4.6}$$

If we further allow $\vec{x} \to S_F$, Eq.(4.6) yields

$$-\frac{1}{4\pi}\int_{S_F} p_n(\vec{\zeta})G(\vec{x};\vec{\zeta})dS(\vec{\zeta}) = p_i(\vec{x}) \tag{4.7}$$

At this point, we discretize the boundaries in Eq.(4.7) into boundary elements

with piecewise continuous values of p_n within each element. Eq.(4.7) can be cast as a system of linear algebraic equations of the form:

$$-\frac{1}{4\pi}(p_n)_j \iint_{E_j} G(\vec{x};\vec{\zeta})dS(\vec{\zeta}) = p_i(\vec{x}) \tag{4.8}$$

where E_j is the j^{th} element and N the total number of elements on S_F. Finally, we we express Eq.(4.8) in symbolic form:

$$[A]\{x\} = \{b\} \tag{4.9}$$

where $[A]$ is an N×N dense matrix. Precorrected fast fourier transform boundary element method (PFFT-BEM), which is a highly efficient numerical scheme for the calculation of $[A]\{x\}$ with an computational cost of $O(N \log N)$ and $O(N)$ memory (without explicitly forming the influence matrix $[A]$), has been applied to solve this boundary value problem.

4.2.2 Incident wave field

For direct numerical computations, we truncate the unbounded rough surface to a surface with finite length. As a result, we need to taper the incident pressure field to zero on the surface edges to avoid the edge effects. Here, we use a modified version of Gaussian tapering function which is proposed and given by Thorsos [1988] as

$$p_i(x,y,z) = \exp\{ik[(x\cos\phi_i + y\sin\phi_i)\sin(\theta_i) - z\cos\theta_i](1+w)\}\exp(-t) \tag{4.10}$$

where

$$t = t_x + t_y \tag{4.11}$$

$$t_x = \frac{(\cos\theta_i\cos\phi_i x + \cos\theta_i\sin\phi_i y + \sin\phi_i z)^2}{g^2\cos^2\theta_i} \tag{4.12}$$

$$t_y = \frac{(\cos\phi_i y - \sin\phi_i x)^2}{g^2} \tag{4.13}$$

$$w = \frac{1}{k^2}[\frac{(2t_x - 1)}{g^2 \cos^2 \theta_i} + \frac{2t_y - 1}{g^2}] \tag{4.14}$$

Here, g controls the tapering domain size. p_i satisfies the wave equation providing that $\gamma = kg \sin \theta_g >> 1$. From previous 2D scattering numerical and analytical studies, it is found that $g = L/4$ is a proper choice [Thorsos, 1988, Isakson et al., 2008]. The appropriate value of γ for 3D surface scattering simulations will be determined by convergence study.

4.2.3 Scattering strength

We demonstrate our numerical results by scattering strength as:

$$SS = 10 \log_{10} \sigma \tag{4.15}$$

with the scattering cross section σ defined as

$$\sigma = \frac{< |p_s|^2 > r^2}{E_3} \tag{4.16}$$

where <> indicates ensemble average, p_s represents the scatted wave pressure at the far field range r, and E_3 is the sound flux through the surface by the incident wave field.

$$E_3 = \iint_S p_i (u_i \cdot n) dS \tag{4.17}$$

where n is the surface normal, u_i is the incident particle velocity on scattering surface S.

4.2.4 Random surface generation

For modeling, the surface roughness is generated to be a random variable characterized by a power spectrum. In this study, we use Gaussian spectrum, which has been used widely for 2D and 3D studies for the rough surface scattering problem [Thorsos, 1988, Thorsos and Darrell, 1989, Kaczkowski and Thorsos, 1994, Isakson et al., 2008, Joshia and Isakson, 2011], to generate random surfaces.

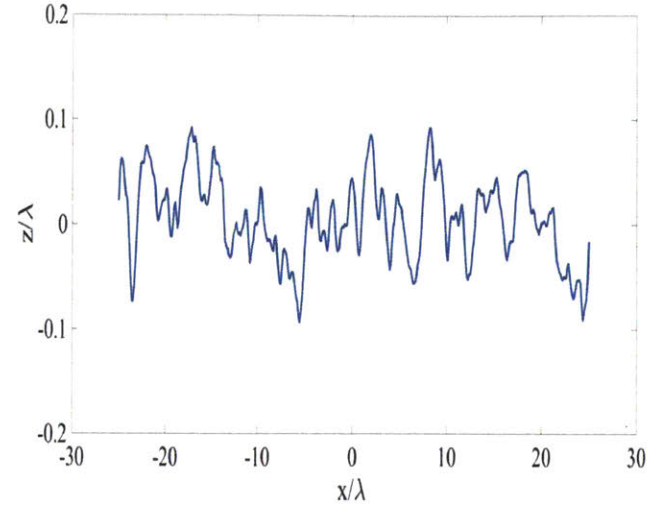

(a)

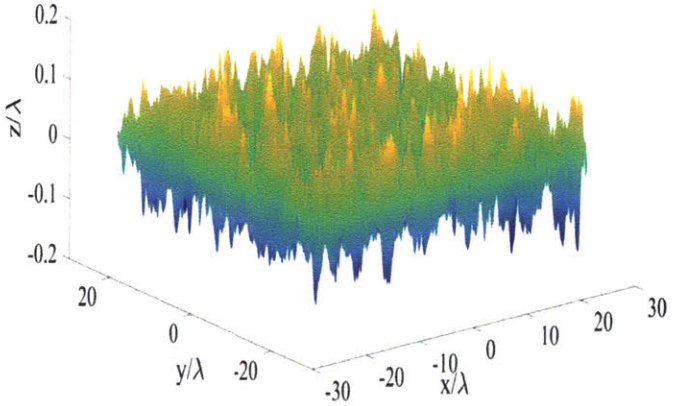

(b)

Figure 4-1: Surface realization with vertical exaggeration where kl=5.6, kh=0.52 (a) Surface shape in xz plane (b) 3D surface.

The surface roughness spectrum $W(K)$ is normalized such that

$$h^2 = \iint_{-\infty}^{\infty} W(\mathbf{K}) d\mathbf{K} \tag{4.18}$$

where h^2 is the mean square surface height and $\mathbf{K} = (k_x, k_y)$ denotes the surface

spatial wave numbers.

The scattering surface has the length of $L_x = N_x dx$ and $L_y = N_y dy$ with N_x (N_y) meshes and equal spacing dx (dy) in the x (y) directions. The surface roughness at point $(x_m, y_n) = (mdx, ndy)$ ($m = 1, ..., N_x$; $n = 1, ..., N_y$) is expressed as

$$\eta(x_m, y_n) = \mathcal{F}^{-1}\{F(k_{xj}, k_{yl})\} \tag{4.19}$$

where $k_{xj} = 2\pi j/L_x$, $k_{yl} = 2\pi l/L_y$ and $\mathcal{F}^{-1}$ is the inverse Fourier transform. The form of $F(k_{xj}, k_{yl})$ is

$$F(k_{xj}, k_{yl}) = 2\pi L_x L_y \sqrt{W(k_{xj}, k_{yl})} \begin{cases} \dfrac{N(0,1) + iN(0,1)}{\sqrt{2}}, & j \neq 0, N_x/2 \quad \text{or} \quad l \neq 0, N_y/2 \\ N(0,1), & j = 0, N_x/2 \quad \text{or} \quad l = 0, N_y/2 \end{cases} \tag{4.20}$$

where $N(0,1)$ is a random independent sample from a normal distribution with zero mean and unit standard deviation. In this study, we use isotropic surface with Gaussian roughness spectrum and $W(\mathbf{K})$ is given by

$$W(\mathbf{K}) = \frac{l^2 h^2}{4\pi} e^{-|\mathbf{K}|^2 l^2/4} \tag{4.21}$$

where l denotes the correlation length of the surface. An example of a surface used in the present study is shown in Fig.4-1 with kl=5.6, kh=0.52.

4.3 Approximate models

4.3.1 Kirchhoff approximation

In this subsection, we will briefly introduce the Kirchhoff approximation. Applying the operator $\frac{\partial}{\partial n}$ to Eq.(4.7), we have

$$\frac{\partial p(\vec{x})}{\partial n} = 2\frac{\partial p_i(\vec{x})}{\partial n} - \frac{1}{2\pi} \iint_S \frac{\partial p(\vec{\zeta})}{\partial n} G_n(\vec{x}; \vec{\zeta}) dS(\vec{\zeta}) \tag{4.22}$$

The Kirchhoff approximation neglects the second term in the right hand side of Eq.(4.22) and yields

$$\frac{\partial p(\vec{x})}{\partial n} = 2\frac{\partial p_i(\vec{x})}{\partial n} \tag{4.23}$$

We can then obtain the Kirchhoff approximation results by inserting Eq.(4.23) to Eq.(4.6) and calculating the average over 50 realizations by Monte Carlo simulations. Shadowing effect is the main reason for the inaccuracy of Kirchoff approximation model. According to Thorsos [1988], the shadowing effect occurs in two situations: for low grazing angles when section of the surface are shadowed from the incident field and for low scattered angles when section of the surface lie in shadows with respect to a receiver. A correction function S, which reduces the error, is proposed by Wagner [1967].

$$S(\theta_g, \theta_s) \begin{cases} S(\theta_s), & 0 \leq \theta_s \leq \theta_g \\ S(\theta_g), & \theta_g \leq \theta_s \leq \pi/2 \\ S(\theta_g, \theta_s) & \pi/2 \leq \theta_s \leq \pi \end{cases} \tag{4.24}$$

where S function is defined as

$$S(\theta_s) = [1 + erf(v_s)](1 - e^{-2B_s})/(4B_s) \tag{4.25}$$

$$S(\theta_g, \theta_s) = [erf(v_g) + erf(v_s)]\{1 - exp[-2(B_g + B_s)]\}/[4(B_g + B_s)] \tag{4.26}$$

$$B_s = \{exp(-9v_s^2/8)/(3\pi v_s^2)^{1/2} + exp(-v_s^2)/(\pi v_s^2)^{1/2} - [1 - erf(v_s)]\} \tag{4.27}$$

with

$$v_s = \frac{|\tan\theta_s|}{\sqrt{2}s} \tag{4.28}$$

and $s = \sqrt{2}h/l$. The quantities v_g ,B_g and $S(\theta_g)$ are obtained by substituting θ_g for θ_s in Eq.(4.28), Eq.(4.27) and Eq.(4.26), respectively. The shadowing correction factor is applied directly to the incoherent part of the scattering cross section as $\sigma_{incoh}^{modified} = S\sigma_{incoh}$. σ_{incoh} is obtained using

$$\sigma_{incoh} = \sigma_{total} - R_{coh}\sigma_{flat} \tag{4.29}$$

where $R_{coh} = e^{-k^2h^2(\sin\theta_s+\sin\theta_i)^2}$ and σ_{flat} is the scattering cross section of a finite length flat surface. From previous study [Thorsos, 1988], the accuracy of 2D Kirchhoff approximation has been examined by comparing with direct numerical simulation. In the present study, we will examine the validity regions of the Kirchhoff approximate model for 3D scattering problems.

4.3.2 Perturbation theory

Another approximate model to solve the rough surface scattering problem is perturbation theory. By expansion with respect to $O(kh)$, we write the acoustics pressure field as a summation of pressure fields at different orders of kh

$$p(\vec{x}) = p_0(\vec{x}) + (kh)p_1(\vec{x}) + [(kh)^2/2]p_2(\vec{x}) + [(kh^3)/3!]p_3(\vec{x}) + ... \tag{4.30}$$

Then p_m is solved at different orders by imposing boundary conditions correspondingly. In the present study, we compare the PFFT-BEM results with the 3D scattering cross section obtained by perturbation theory up to $O(kh)^4$. Our objective is to obtain the validity regions of the perturbation theories. Here, we only present the forms of corresponding scattering cross sections at different orders. The detailed derivation can be found in Thorsos and Darrell [1989].

The first oder perturbation model obtains corresponding scattering cross section up to $(kh)^2$ as

$$\sigma^{11} = 4k^2\sin^2(\theta_g)\sin^2(\theta_s)W(\mathbf{K_i} - \mathbf{K_s}) \tag{4.31}$$

where $\mathbf{K} = (k_x, k_y)$.

By expanding the acoustics pressure field up to the second order in the scattering pressure p_2, we obtain one part of the scattering cross section up to fourth order by $< |p_2|^2 > -| < p_2^2 > |$

$$\begin{aligned}\sigma^{22} = 4k^2\sin^2(\theta_g)\sin^2(\theta_s)\iint_{-\infty}^{\infty} d\mathbf{K}W(\mathbf{K_s} - \mathbf{K})W(\mathbf{K} - \mathbf{K_i}) \\ \times\{|k^2 - |\mathbf{K}|^2| + \sqrt{k^2 - |\mathbf{K}|^2}[\sqrt{k^2 - |\mathbf{K_i} + \mathbf{K_s} - \mathbf{K}|^2}]^*\}\end{aligned} \tag{4.32}$$

$< p_1 p_3^* + p_3 p_1^* >$ contributes another part of the fourth order scattering cross section. This part is denoted by σ^{13} and expressed as

$$\sigma^{13} = \{4k^2 \sin^2(\theta_g) \sin^2(\theta_s) W(\mathbf{K_s} - \mathbf{K_i}) \times [h^2(|\mathbf{K_s}|^2 + |\mathbf{K_i}|^2) - 2\Re(I)]\} \tag{4.33}$$

with

$$\begin{aligned} I = \iint_{-\infty}^{\infty} d\mathbf{K} W(\mathbf{K}) [|k \sin(\theta_g)| \sqrt{k^2 - |\mathbf{K_i} - \mathbf{K}|^2} \\ + |k \sin \theta_s| \sqrt{k^2 - |\mathbf{K_s} - \mathbf{K}|^2} + \sqrt{k^2 - |\mathbf{K_i} - \mathbf{K}|^2} \\ \times \sqrt{k^2 - |\mathbf{K_s} - \mathbf{K}|^2} + k^2] \end{aligned} \tag{4.34}$$

We give the final expression of scattering cross section up to $(kh)^4$ as

$$\sigma^{(4)} = \sigma^{11} + \sigma^{22} + \sigma^{13} \tag{4.35}$$

The above perturbation incoherent theory is valid to all the scattering directions θ_s except at the specular direction. To obtain a fair comparison with the PFFT-BEM results, we include the coherent part of the scattering section by combining the Kirchhoff approximation results for a flat surface and a refection coefficient [Kaczkowski et al., 1994]. The total cross section σ (for both first order and second order) is then given by

$$\sigma = \sigma_{incoh} + |R_f|^2 \sigma_f \tag{4.36}$$

where σ_f is the scattering cross section result of a flat surface obtained by Kirchhoff approximation. The reflection coefficient R_f is defined as

$$R_f = -1 + 2|k \sin \theta_g| \iint_{-\infty}^{\infty} d\mathbf{K} W(\mathbf{K_i} - \mathbf{K}) \sqrt{k^2 - |\mathbf{K}|^2} \tag{4.37}$$

4.4 Results and discussions

In this section, we first investigate the accuracy dependence of the direct numerical simulation on parameter γ=$kg \sin \theta_g$. From a convergence test, we obtain the optimal value of γ. Secondly, we use this γ and 2D PFFT-BEM method to study the 2D

rough surface scattering problem. By comparing the 2D PFFT-BEM results with the direct simulation solutions from previous studies [Kaczkowski and Thorsos, 1994] and the corresponding approximation models, we validate the accuracy and efficiency of PFFT-BEM method in studying the rough surface scattering problem. Thirdly, we conduct direct 3D simulations to investigate the applicability of the perturbation and Kirchhoff approximate models for the 3D rough surface scattering problems. Based on the 3D direct numerical simulation results, we obtain the validity region for 3D rough surface scattering models in the kh-kl plane. Fourthly, we simulate the low grazing angle ($\theta = 10°$) results by 3D PFFT-BEM to demonstrate the scattering features for small θ_g. At last, we study the effect of grazing angle on the validity of different approximation models in the backscattering direction.

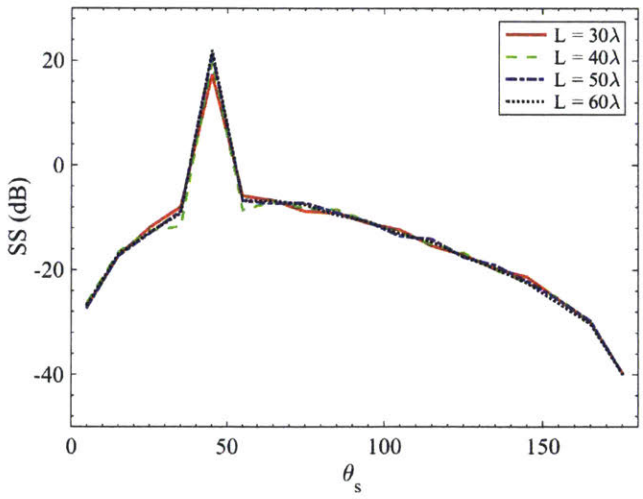

Figure 4-2: SS comparison for different domain size L using 3D direct numerical simulation by PFFT-BEM. The incident wave grazing angle $\theta_g = 45°$, the surface parameter is chosen to be $kh = 0.52$, $kl = 2.6$. Here k and λ are the acoustics wavenumber and wavelength.

4.4.1 Test for convergence of domain size

In this subsection, we test the convergence behavior of the results with respect to γ=$kg\sin\theta_g$. As γ is directly related to the domain size L, we compare the scattering strength obtained using Monte Carlo simulation by 3D PFFT-BEM with different L. Here, we choose the grazing angle $\theta_g = 45°$. The boundary element size is chosen to be uniform as $\lambda/8$, where λ is the acoustic wavelength. The tapering size g is chosen as $g = L/4$ as suggested by previous study [Thorsos, 1988]. As shown in Fig. 4-2, the variation in PFFT-BEM solution becomes very small (with no visible error) after $L = 50\lambda$ (corresponding to $\gamma \simeq 55$). As a result, we choose to use the parameters as $\gamma \geq 55$ and g=$L/4$ in this study.

4.4.2 Comparison with 2D direct numerical simulation results

We show the 2D validity regions of the first-order perturbation model ($\sigma^{(2)}$), second-order perturbation model ($\sigma^{(4)}$), Kirchhoff approximation obtained by various 2D studies [Thorsos, 1988, Thorsos and Darrell, 1989, Kaczkowski and Thorsos, 1994] in Fig.4-3. Three 2D examples are selected from these regions (denoted as (b)-(c) in Fig.4-3). The grazing angle used here is θ_g=45°.

We compare 2D PFFT-BEM results with existing 2D direct integral solutions and approximation model solutions for three different distributions of surface roughness from Kaczkowski and Thorsos [1994]. From Fig.4-3(b)-(d), we obtain close agreement between the numerical results from 2D PFFT-BEM, the 2D direct integral solution from Kaczkowski and Thorsos [1994] and approximation model results. From these comparisons, we show that the PFFT-BEM results are equivalent to the exact solution for rough surface acoustics scattering problems.

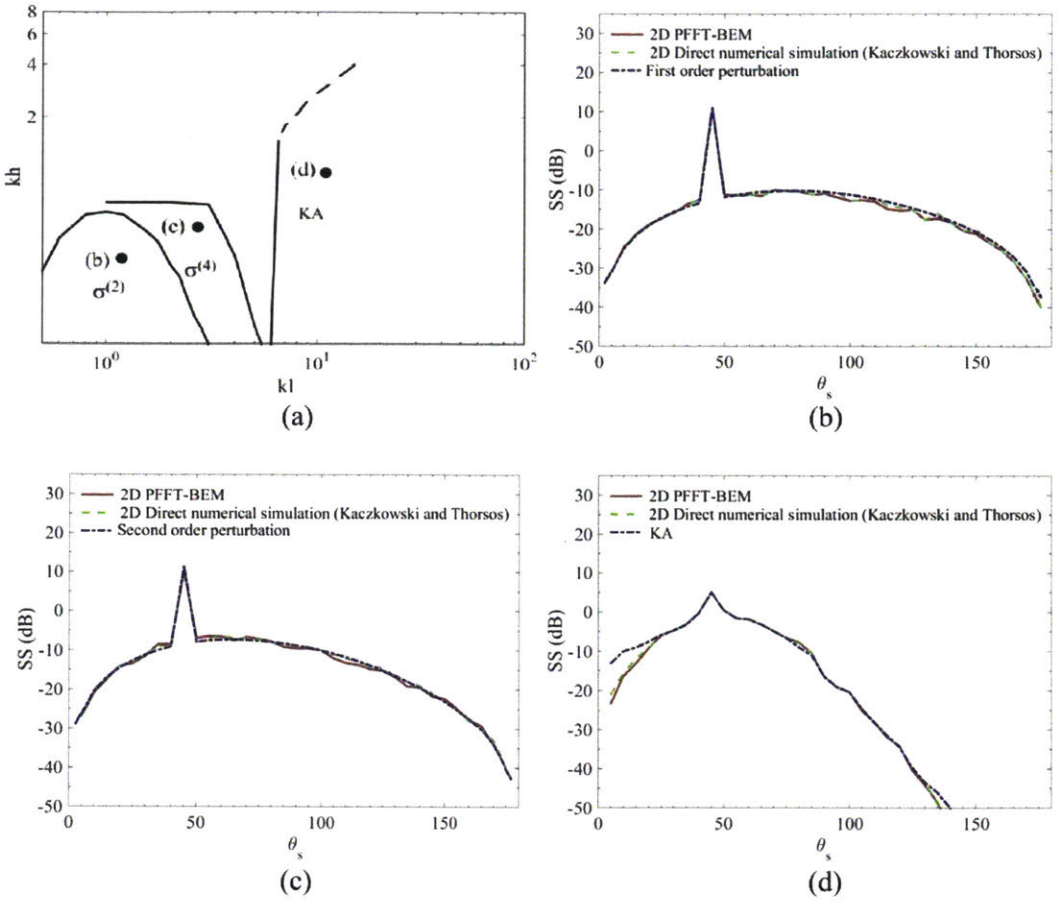

Figure 4-3: (a) Locations of the numerical examples (b-d) in the kh-kl plane , the 2-D validity regions (1-dB error) for the first-order perturbation theory, second-order perturbation theory and the Kirchhoff approximation. The incident wave grazing angle $\theta_g = 45°$. (b) Comparison of the SS obtained by 2D direct numerical simulation using PFFT-BEM with 2D direct numerical simulation by Kaczkowski and Thorsos [1994] and first-order perturbation theory ($kh = 0.38$, $kl = 1.4$). (c) Comparison of the SS obtained by 2D direct numerical simulation using PFFT-BEM with 2D direct numerical simulation by Kaczkowski and Thorsos [1994] and second-order perturbation theory ($kh = 0.52$, $kl = 2.6$). (d) Comparison of the SS obtained by 2D direct numerical simulation using PFFT-BEM with 2D direct numerical simulation by Kaczkowski and Thorsos [1994] and Kirchhoff approximation results ($kh = 10.0$, $kl = 1.03$).

4.4.3 The validity regions of 3D perturbation theory and Kirchhoff approximation

In this subsection, we compare our 3D PFFT-BEM numerical simulation results with 3D first order, second order perturbation and Kichhoff approximation results. Our goal is to identify the validity regions of these approximate models for 3D rough surface scattering problems.

3D first-order perturbation theory

We first obtain the validity region of 3D first-order perturbation theory, denoted as $\sigma^{(2)}$. The grazing angle θ_g=45°. We examine the accuracy of the 3D perturbation theory by comparing it with direct simulation results by 3D PFFT-BEM. We obtain the $\sigma^{(2)}$ validity region in the *kh-kl* space. We adopt a maximum 1-dB error criterion here based on Thorsos and Darrell [1989] as:

$$|10\log_{10}[(\sigma^{11}+\sigma^{22}+\sigma^{13})/\sigma^{11}]| \leq 1dB \tag{4.38}$$

and

$$10\log_{10}(\sigma^{11}/|\sigma^{13}|) \geq 1dB \tag{4.39}$$

where σ^{11}, σ^{22} and σ^{13} could be obtained based on the formulation in section 4.3.2. Given a single grazing angle, this criterion needs to be valid for all scattering angles. We make a number of numerical simulations near the boundary above and below the 1-dB error contours to support the criterion shown in Eq.(4.38) and Eq.(4.39). We show here four examples among these tests. The locations of the four examples ((a)-(d)) in the $kh-kl$ contour are shown in Fig.4-4. As shown in Fig.4-5, by moving the test points outside from the $\sigma^{(2)}$ region ((a)→(d)), the first-order perturbation theory results become deviated from the 3D PFFT-BEM results, which validate the $\sigma^{(2)}$ region.

3D second-order perturbation theory

Monte Carlo direct computations by 3D PFFT-BEM have been used in the present study to obtain an estimate of 3D second order perturbation theory ($\sigma^{(4)}$) 1-dB validity region. We obtain the scattering strength over different scattering angles using 3D PFFT-BEM. The grazing angle θ_g=45°. This estimation has been included as the upper red line in Fig.4-6. Four examples ((a)-(d)) below and above the 1-dB error are shown in Fig.4-7.

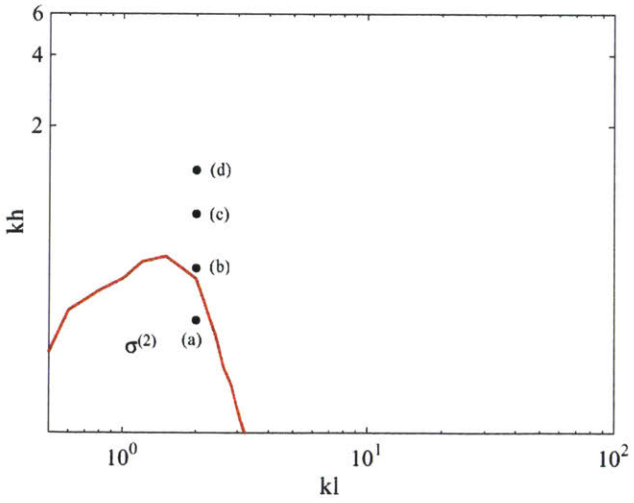

Figure 4-4: The 3D validity regions (1-dB error) for the first-order perturbation theory ($\sigma^{(2)}$). These regions are valid for θ_g=45°. The black dots represent the locations of the numerical examples (a)-(d) shown in Fig.4-5.

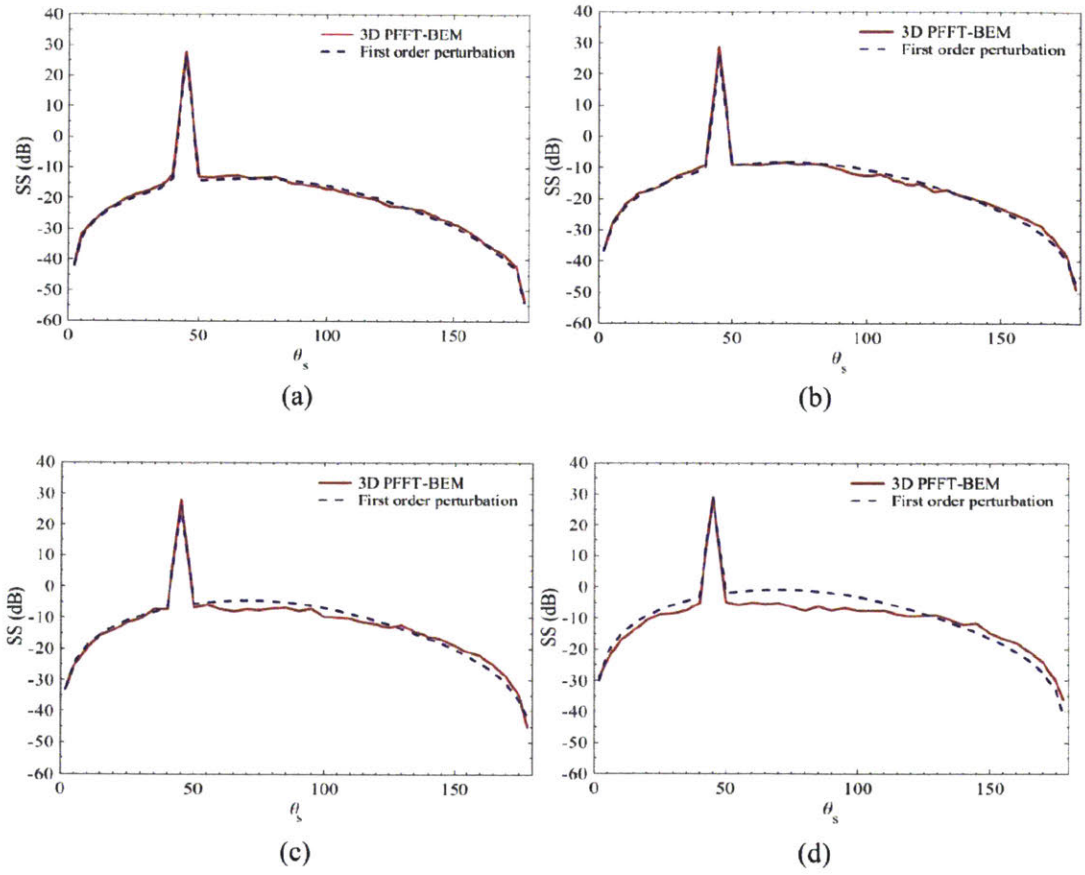

Figure 4-5: Comparison of the SS obtained by 3D direct numerical simulation using PFFT-BEM with 3D first order perturbation theory with (a) $kh = 0.3$, $kl = 2.0$ (b) $kh = 0.55$, $kl = 2.0$ (c) $kh = 0.85$, $kl = 2.0$ (d) $kh = 1.3$, $kl = 2.0$, here θ_g=45°.

As shown in Fig.4-7(a) which is outside of $\sigma^{(2)}$ region while in $\sigma^{(4)}$ region, first-order perturbation results show significant errors when $\theta_s > 60°$. On the other hand, $\sigma^{(4)}$ yields good agreement with the 3D PFFT-BEM results for $\theta_s > 60°$. As the numerical example moves far away from the $\sigma^{(2)}$ validity region (Fig.4-7(b)), the first-order perturbation results become more inaccurate while second-order perturbation results match well the direct 3D PFFT-BEM results. This indicates that the contributions from higher-order perturbation theory become more dominant. As expected, the use of second-order perturbation theory breaks down when moving out of

the $\sigma^{(4)}$ validity region as shown in Fig.4-7(c) and Fig.4-7(d).

3D Kirchhoff approximation

Next we examine the validity region of the 3D kirchhoff approximation. As indicated by 2D studies [Thorsos, 1988] and shown in section 4.4.2, the Kirchhoff approximation is usually considered suspect for low scattering angles and in the backscattering angles. As a result, we use Monte Carlo numerical simulation to obtain the validity region of Kirchhoff approximation with 1-dB error only near the specular direction ($\theta_{specular} \pm 25°$). As a result, the shadowing correction factors described in this chapter are not applied in this comparison. This validity region is shown in Fig.4-9. Four numerical examples (a)-(d), shown in Fig.4-9, are selected from these Monte Carlo simulations inside and outside the 1dB region.

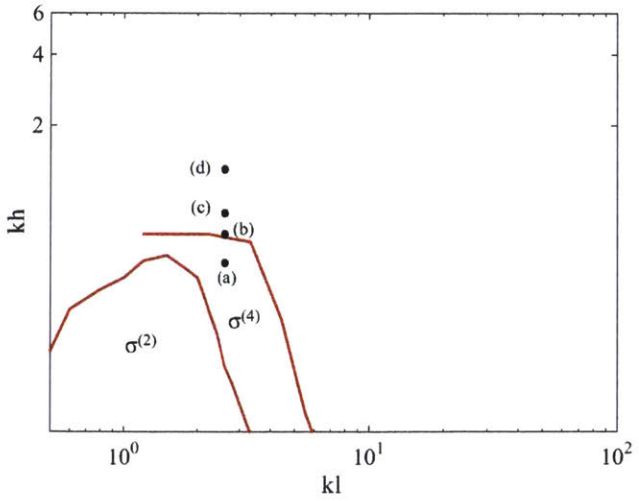

Figure 4-6: The 3D validity regions (1-dB error) for the first (lower line) and second order perturbation theory (upper line). These regions are validity for θ_g= 45°. The black dots represent the locations of the numerical examples (a)-(d) shown in Fig.4-7.

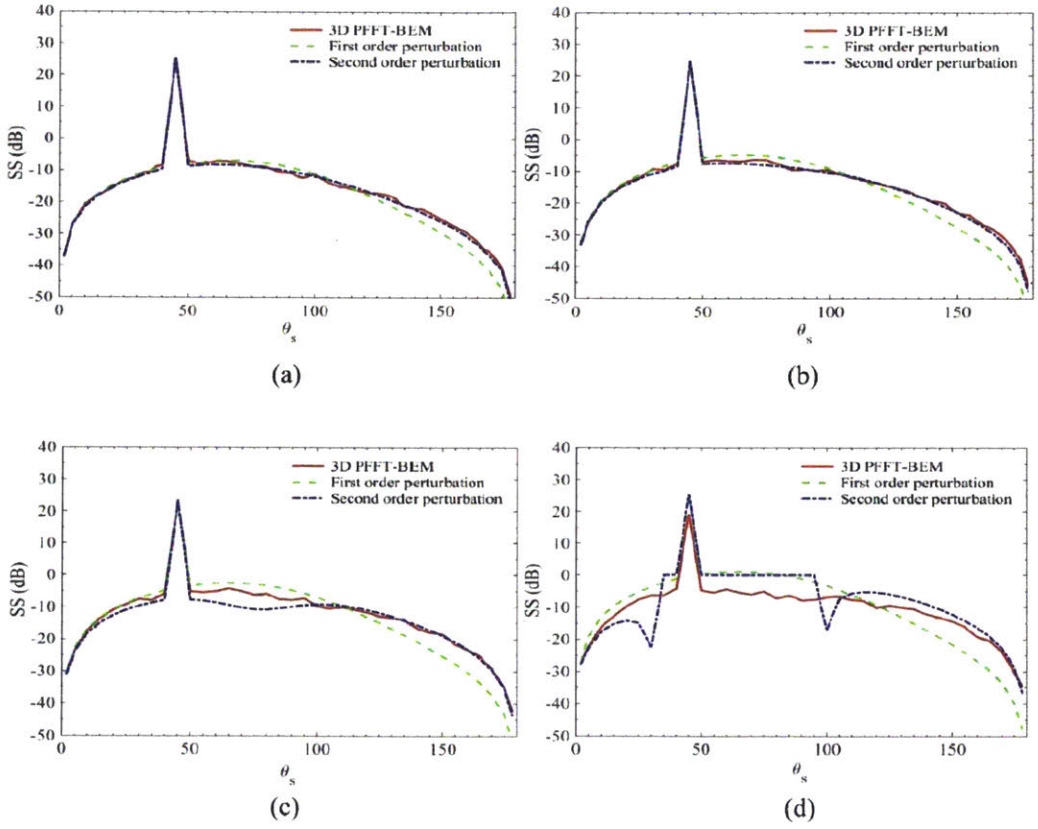

Figure 4-7: Comparison of the SS obtained by 3D direct numerical simulation using 3D PFFT-BEM with 3D first-order and second-order perturbation theory with (a) $kh = 0.52$, $kl = 2.6$ (b) $kh = 0.65$, $kl = 2.6$ (c) $kh = 0.85$, $kl = 2.6$ (d) $kh = 1.3$, $kl = 2.6$, here θ_g=45°.

As shown in Fig.4-8, similar to 2D cases, the 3D Kirchhoff approximation over predicts the scattering strength for the case with small scattering angle in the forward scattering region and the backscattering in general. Also, by moving the test points outside from the KA region ((a)→(d)), the Kirchhoff approximation results become deviated from the 3D PFFT-BEM results, which validate the KA region.

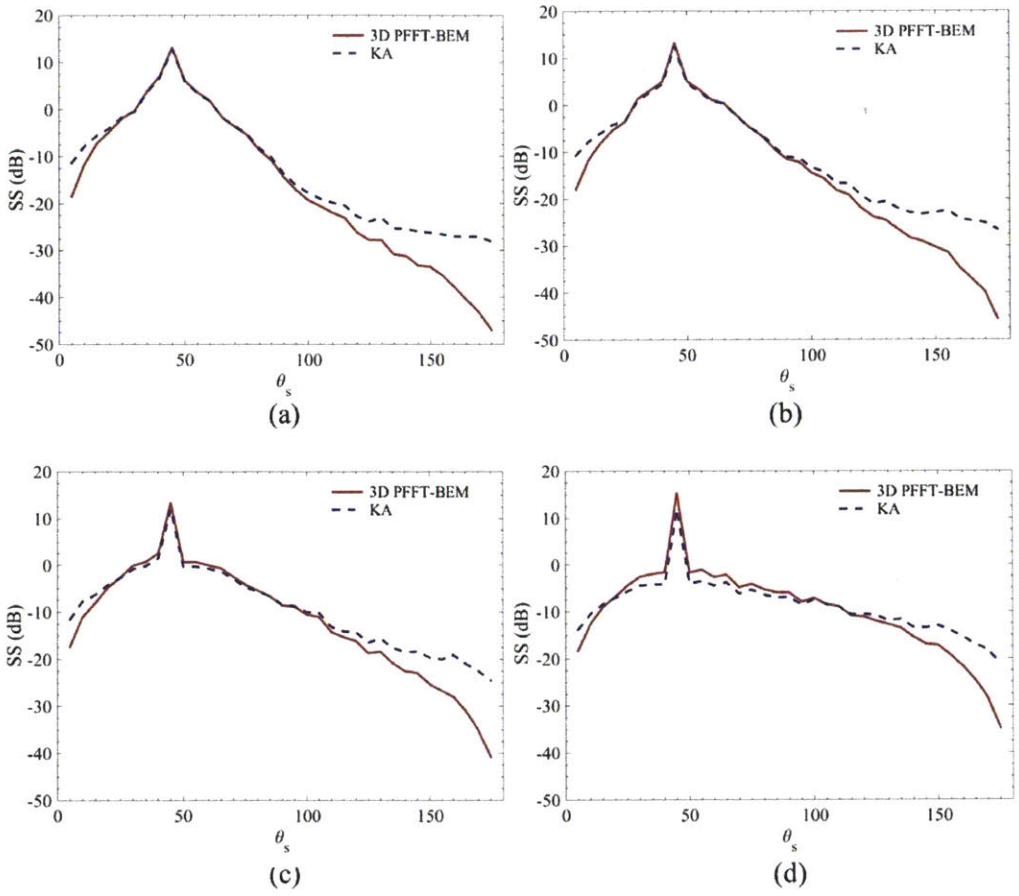

Figure 4-8: Comparison of the SS obtained by 3D direct numerical simulation using 3D PFFT-BEM with Kirchhoff approximation with (a) $kh = 1.33$, $kl = 20$ (b) $kh = 1.33$, $kl = 15$ (c) $kh = 1.33$, $kl = 10$ (d) $kh = 1.33$, $kl = 5.6$, here θ_g=45°.

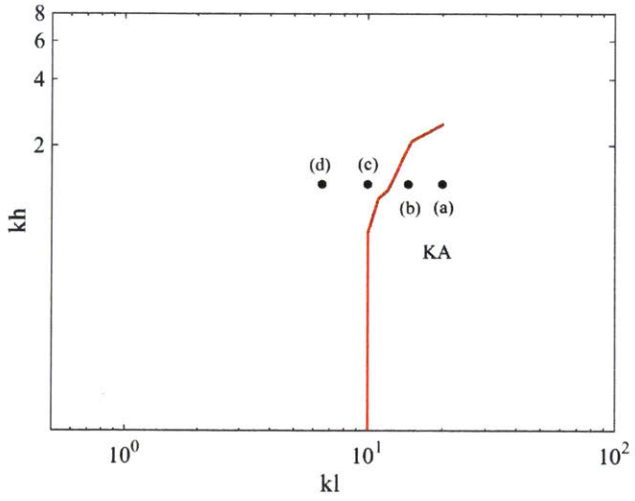

Figure 4-9: The 3D validity regions (1-dB error near the specular direction) for Kirchhoff approximation. These regions are valid for θ_g=45°. The black dots represent the locations of the numerical examples (a)-(d) shown in Fig.4-8.

4.4.4 Comparison between 2D and 3D validity regions

In this subsection, we further compare the 3D validity regions with 2D validity regions. The 2D validity regions is obtained from Kaczkowski et al. [1994]. As shown in Fig.4-10, the validity regions of the first-, second-order perturbation theories and the Kirchhoff approximations are all shifted to larger kl regions in the 3D cases. This difference is mainly due to the out of plane scattering effects in 3D cases.

To have a better understanding of the difference between 2D and 3D validity regions, we obtain the asymptotic form of $\sigma^{(4)}$ for $kl >> 1$ and $kl << 1$.

For $kl >> 1$, the contribution of σ^{13} to $\sigma^{(4)}$ can be neglected comparing with the one of σ^{22} [Thorsos and Darrell, 1989]. We then write 2D $\sigma^{(4)}_{2D}$ as

$$\begin{aligned}\sigma^{(4)}_{2D} = \sigma^{22}_{2D} = \frac{4k_{iz}^2 k_{sz}^2}{k}\int_{-\infty}^{\infty} dk_x W_{2D}(k_{sx}-k_x)W_{2D}(k_{ix}-k_x) \\ \times\{|k^2-k_x^2| + \sqrt{k^2-k_x^2}[\sqrt{(k^2-k_{ix}+k_{sx}-k_x)^2}]^*\}\end{aligned} \tag{4.40}$$

where $W_{2D}(k) = lh^2/\sqrt{4\pi}e^{-k^2l^2/4}$.

For a Gaussian spectrum with a large correlation length and for scattering in back scattering direction, the main contribution to the integral in Eq.(4.40) occurs when the arguments of the two W_{2D} function are about equal [Thorsos and Darrell, 1989]. Under this condition, Eq.(4.40) yields:

$$\sigma_{2D}^{(4)} = \sigma_{2D}^{22} = \frac{4k_{iz}^2 k_{sz}^2}{k}\sqrt{2}(k^2 - \frac{(k_{sx}+k_{ix})^2}{4})h^2 W_{2D}(\frac{k_{ix}-k_{sx}}{\sqrt{2}}) \tag{4.41}$$

For the 3D case, a similar procedure can be conducted for Eq.(4.32) and Eq.(4.21). For $kl >> 1$ at back scattering direction, $\sigma_{3D}^{(4)}$ yields

$$\sigma_{3D}^{(4)} = \sigma_{3D}^{22} = 4k_{iz}^2 k_{sz}^2(k^2 - \frac{(k_{sx}+k_{ix})^2}{4})h^2 W_{3D}(\frac{k_{ix}-k_{sx}}{\sqrt{2}}) \tag{4.42}$$

Here, $W_3D \equiv W$ in Eq.(4.21).

On the other hand, the exact forms of $\sigma^{(2)}$ in 2D and 3D are

$$\sigma_{2D}^{(2)} = (4k_{iz}^2 k_{sz}^2/k)W_{2D}(k_{ix}-k_{sx}) \tag{4.43}$$

and

$$\sigma_{3D}^{(2)} = (4k_{iz}^2 k_{sz}^2)W_{3D}(k_{ix}-k_{sx}) \tag{4.44}$$

Due to the form of the Gaussian spectrum, we have

$$\frac{W_{2D}(k_{ix}-k_{sx})}{W_{2D}(\frac{k_{ix}-k_{sx}}{\sqrt{2}})} = \frac{W_{3D}(k_{ix}-k_{sx})}{W_{3D}(\frac{k_{ix}-k_{sx}}{\sqrt{2}})} \tag{4.45}$$

As a result, for a fixed kh and kl, we obtain the relation given by

$$\frac{\sigma_{2D}^{(4)}}{\sigma_{2D}^{(2)}} = \sqrt{2}\frac{\sigma_{3D}^{(4)}}{\sigma_{3D}^{(2)}} \tag{4.46}$$

This indicates that for a fixed surface roughness condition and grazing angle, the difference between 2nd-order and 1st-order scattering cross sections in 2D is larger than that of 3D. As a result, for $kl >> 1$, the 1-dB error contour between 2nd order

and 1st-order results is expanded in the 3D case.

For $kl << 1$, on the other hand, the 2D formal perturbation theory [Thorsos and Darrell, 1989] gives

$$\sigma_{2D}^{(2)} \rightarrow (4k_{iz}^2 k_{sz}^2/k) l h^2/(2\sqrt{\pi}) \tag{4.47}$$

for the first order and

$$\sigma_{2D}^{(4)} \rightarrow \frac{4k_{iz}^2 k_{sz}^2}{k} 2 \int_{-\infty}^{\infty} dk_x [W_{2D}(k_x)]^2 k_x^2 = \frac{1}{\sqrt{2}} s^2 \sigma_{2D}^{(2)} \tag{4.48}$$

for the second order. $s = \sqrt{2}h/l$. Similar results can be obtained in the 3D case as

$$\sigma_{3D}^{(2)} \rightarrow 4k_{iz}^2 k_{sz}^2 l^2 h^2/(4\pi) \tag{4.49}$$

for the first order and

$$\sigma_{3D}^{(4)} \rightarrow s^2 \sigma_{3D}^{(2)} \tag{4.50}$$

for the second order. As a result, when $kl << 1$, for a fixed kh and kl, we could obtained the relation as

$$\frac{\sigma_{2D}^{(4)}}{\sigma_{2D}^{(2)}} = \frac{1}{\sqrt{2}} \frac{\sigma_{3D}^{(4)}}{\sigma_{3D}^{(2)}} \tag{4.51}$$

This indicates that for a fixed surface roughness condition and grazing angle, the difference between second-order and first-order scattering cross sections in 2D is smaller than that of 3D. As a result, for $kl << 1$, the 1-dB error contour between second-order and first-order shrinks in the 3D case. This explains quantitatively the shift of the validity regions in Fig.4-10. To validate our asymptotic analysis, we compare our asymptotic results with the direct numerical simulation. As shown in Fig.4-11, good agreements between the asymptotic and direct simulation results are obtained.

The validity region of Kirchhoff approximation has the most significant changes in 3D among the approximate models. From observation, we find that the validity region of Kirchhoff approximation decreases in 3D. This is because that shadowing effects are stronger for 3D cases. To show this, we compare the 2D and 3D results for same surface roughness: $kh = 1.03$, $kl = 10.0$. The shadowing correction factors are applied to the Kirchhoff approximation results here. From comparison, we find that the Kirchhoff approximation errors are more significant in 3D (Fig.4-12) than the ones in 2D (Fig.4-5 (c)), especially in the backscattering direction. According to Thorsos [1988], the errors of Kirchhoff approximation in the backscattering direction is mainly due to the inaccurate modeling of shadowing effects. The larger errors in 3D therefore indicate that the shadowing effects is stronger in 3D than that in 2D.

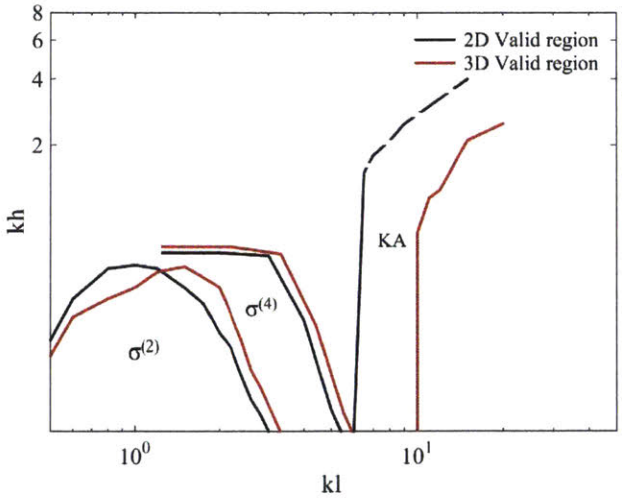

Figure 4-10: Comparison between the 2D and 3D validity regions (1-dB error) for the first-order perturbation theory ($\sigma^{(2)}$), second-order perturbation theory ($\sigma^{(4)}$) and the Kirchhoff approximation. These regions are valid for θ_g=45°.

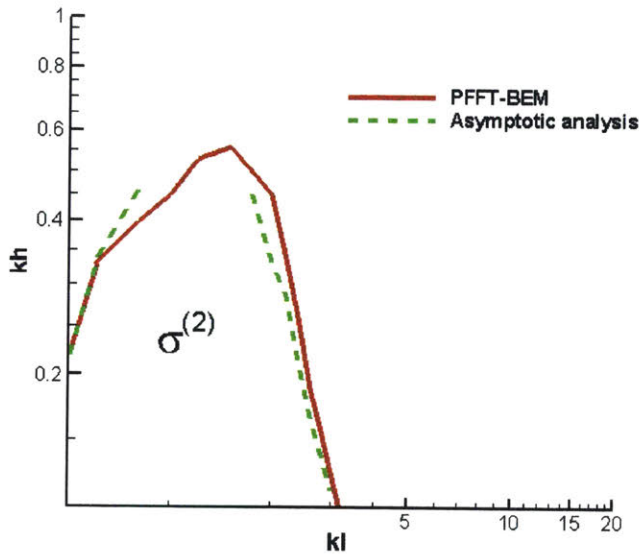

Figure 4-11: Comparison of the $\sigma^{(2)}$ 1-dB error curve obtained by 3D direct numerical simulation using 3D PFFT-BEM and asymptotic analysis with $kl >> 1$ and $kl << 1$, here θ_g=45°.

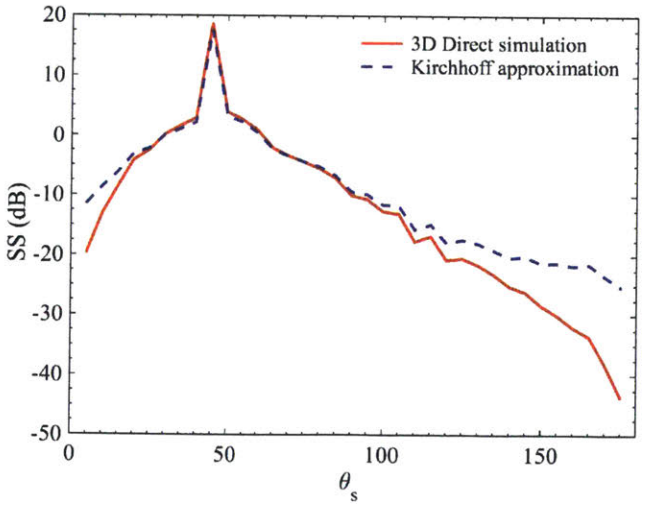

Figure 4-12: Comparison of the SS obtained by 3D direct numerical simulation using 3D PFFT-BEM with Kirchhoff approximation ($kh = 1.03$, $kl = 10.0$), here θ_g=45°.

4.4.5 Effects of low grazing angles

Rough surface scattering problem at low grazing angles is of practical importance in underwater acoustics. However, the validities of perturbation theory and Kirchhoff approximation models remain suspect especially near the backscattering direction [Thorsos and Darrell, 1989]. From previous discussion, we show that investigation of low grazing angles effect for 3D rough surface scattering problem requires large computational cost. Here, we first present cases with a low grazing angle θ_g=10°. Three surface conditions are selected and compared as shown in Fig.4-13, Fig.4-14 and Fig.4-15.

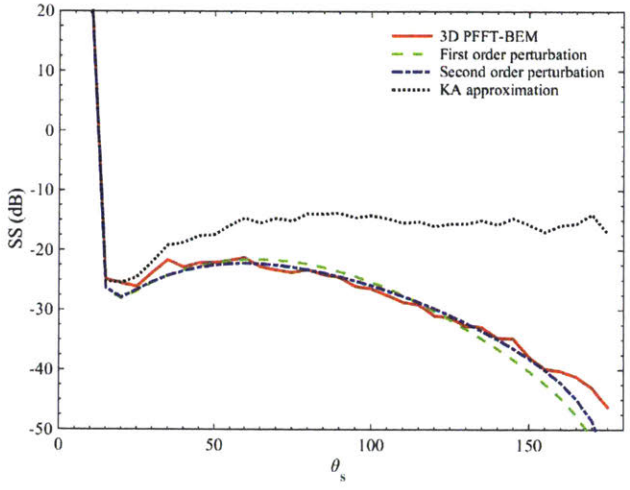

Figure 4-13: Comparison of the SS obtained by 3D direct numerical simulation using 3D PFFT-BEM with 3D first-order, second-order perturbation theory and Kirchhoff approximation with $kh = 0.55$, $kl = 2.0$, here $\theta_g = 10°$.

From comparison, first second order perturbation theory and Kirchhoff approximation all become inaccurate for low grazing angle cases, especially near the backscattering directions. We can explain this behavior by examining the 1-dB criterion in Eq.(4.38). For large kl, this criterion would take the form [Thorsos and Darrell, 1989]

in the backscattering direction as

$$kh < B\exp[-|\mathbf{K}_i - \mathbf{K}_s|^2 l^2/16] \tag{4.52}$$

where $B = 0.35[1-(k_{sx}+k_{ix})^2/(2k)^2]^{-1/2}$. For low grazing angle $\theta_g \to 0$, $|\mathbf{K}_i - \mathbf{K}_s| = 2k$ which minimizes the maximum allowed kl in Eq.(4.52) for a fixed kh.

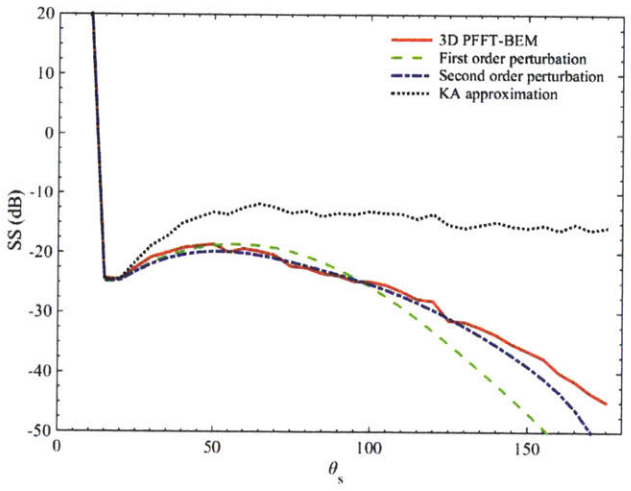

Figure 4-14: Comparison of the SS obtained by 3D direct numerical simulation using 3D PFFT-BEM with 3D first-order, second-order perturbation theory and Kirchhoff approximation with $kh = 0.65$, $kl = 2.6$, here $\theta_g = 10°$.

To further analyze the effects of different grazing angles, we calculate and compare the backscattering cross sections (defined as the scattering cross section at $\theta_s = \pi - \theta_g$) down to $\theta_g = 2.5°$. We compared the results obtained using second order perturbation theory, Kirchhoff approximation and 3D PFFT-BEM method. Two cases with different roughness are considered here: (a) kl=2.6, kh=0.65 in 3D $\sigma^{(4)}$ region and (b) with kl=15, kh=1.33 in 3D Kirchhoff approximation region. As shown in Fig.4-16, the second order perturbation theory remains to be a good approximation until very small incident grazing angle ($\theta_g < 20°$) while Kirchhoff approximation only provides accurate results when incident acoustic wave is close to the normal direction

of the rough surface ($\theta_g \sim 90°$). We also plot the results obtained using Lambert's law in Fig.4-16 for comparison. Lambert's law is often used to estimate bottom scattering strengths from very rough ocean bottoms. It states that the scattered power in the backscattering direction from a rough surface is proportional to $\sin^2\theta_g$. A good review of Lambert's law can be found in Jensen et al. [2011]. As shown in Fig.4-16, Lambert's law compares well with direct numerical solutions for grazing angle up to 40°. This result indicates that for 3D rough surface with large kl and moderate kh, direct numerical simulation is required to obtain an accurate backscattering result, especially for low grazing angles.

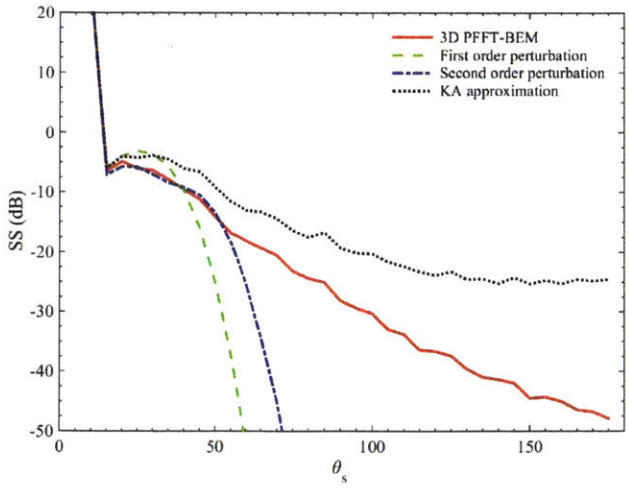

Figure 4-15: Comparison of the SS obtained by 3D direct numerical simulation using 3D PFFT-BEM with 3D first-order, second-order perturbation theory and Kirchhoff approximation with $kh = 1.33$, $kl = 15.0$, here $\theta_g = 10°$.

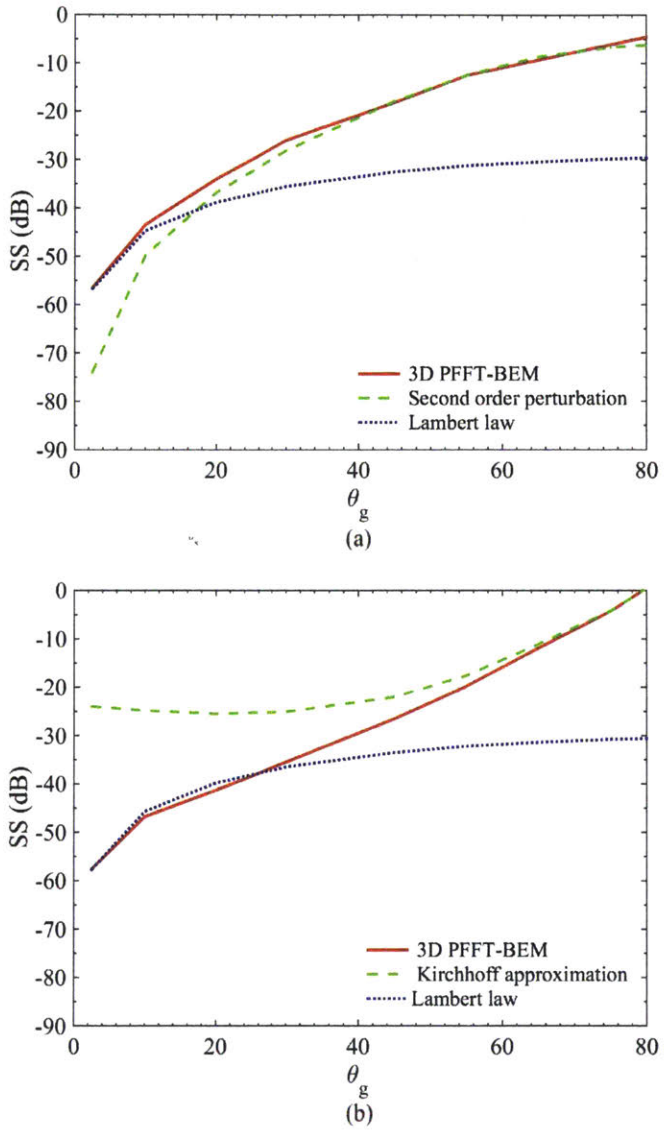

Figure 4-16: SS in the backscattering direction with different grazing angle θ_g (down to 2.5°) with (a) kl=2.6, kh=0.65 and (b) kl=15, kh=1.33.

4.5 Concluding remarks

PFFT-BEM method has been used to perform Monte Carlo computation of acoustics scattering from 3D rough surfaces. We investigate 3D rough surfaces scattering problems over a large range of parameter values. Using direct numerical simulation by 3D PFFT-BEM, we obtain the validity regions for different approximate models such as the first- and second-order perturbation theories and Kirchhoff approximation for the 3D rough surface scatterings. From comparing the 2D validity regions and 3D validity regions, we find that the validity regions for first- and second-order perturbation theories and Kirchhoff approximation are shifted to larger kl regions in 3D. We then discuss the reason for this shift in detail. The 3D scattering from rough surface at low grazing angles is also studied in this chapter. From numerical results by PFFT-BEM, it is found that the perturbation theory remains to be a good approximation until small incident grazing angle ($\theta_g < 20°$) while Kirchhoff approximation only provides accurate results when incident acoustic wave is close to the normal direction of the rough surface ($\theta_g \sim 90°$). This result indicates that for 3D rough surfaces with large kl and moderate kh, direct numerical simulation is required in order to obtain an accurate backscattering result, especially for low grazing angles.

Chapter 5

Study on 3D sound field around underwater seamount

An efficient three-dimensional O(Nlog N) multi-layer boundary-element method, PFFT-BEM, has been developed. The method is capable of accounting for complex topography, inhomogeneity of water properties, and dynamic environments associated with complex coastal and estuarine conditions. In the previous chapters, this method is benchmarked against several theoretical/numerical solutions. Through comparison with existing field experiments, we also demonstrate the efficiency and accuracy of the PFFT-BEM for 4D acoustics simulation under realistic environments.

In this chapter, we conduct a 3D direct numerical study of sound propagation and scattering by an underwater seamount environment. This is a classical three-dimensional problem in which the azimuthal inhomogeneity and 3D effects are important and can not be neglected. As a result, the traditional method such as $N \times 2D$ method [Perkins and Baer, 1982], which assumes the out-of-plane scattering to be insignificant, could not provide accurate results.

3D propagation models, such as the 3D Parabolic equation (PE) method [Lee et al., 1990, 1992, Collins et al., 1995, Lin et al., 2013] can provide approximate solutions by neglecting the backscattering effects. However, as will be shown in this chapter, the backscattering effect can be important for the scattering problem of 3D seamounts especially with specified mountain geometries.

Another widely used method to study the 3D underwater seamount problem is the couple mode method [Taroudakis, 1996, Luo and Schmidt, 2009]. By assuming the conical seamount geometry, these methods provide accurate results in both backscattering and forward scattering directions. However, the coupled mode method developed by Taroudakis [1996] are severely limited in terms of frequency, size and geometry of the seamount. By extending this coupled mode method, Luo and Schmidt [2009] obtained accurate and efficient coupled mode method for 3D propagation and scattering around a large scale conical seamount.

On the other hand, direct numerical method requires huge computational effort to solve such fully three-dimensional problem directly. First attempt was conducted by Xie et al. [2016] using SEM. However, the size of the seamount and the sound frequency are still limited. In this chapter, with the highly efficient PFFT-BEM method, we obtain the exact numerical solution of such a three dimensional seamount scattering problem. We assess the influences of different seamount geometries and sound source frequencies through numerical studies. From these numerical results, we examine the applicability of $N \times 2D$ method, axisymmetric coupled mode method and PE method .

This chapter is organized as follows: We first compare our numerical results for a specified seamount geometry (i.e. conical seamount) with the known 3D couple mode results [Luo and Schmidt, 2009] which is only valid for axisymmetric (circular conical) geometries. This step is used to demonstrate the accuracy of the PFFT-BEM method in studying 3D underwater seamount problem. We then simulate and compare our 3D numerical results with different seamount geometries (height and cross section shapes) and sound source frequencies. The aim of this step is to demonstrate the dependence of the backscattering, blocking and 3D scattering effects on the seamount geometries and source frequencies. From these numerical results, we demonstrate and discuss the applicability of $N \times 2D$ approximation, coupled mode methods and PE method. At last, we provide two benchmark solutions. The first case is the seamount located on New Jersey shelf with realistic sea condition. This example includes multi-layer sound speed conditions and 3D complex bathmetry. The second benchmark is the

double seamount scattering problem. By comparing with the results obtained by different kinds of Parabolic equation method [Lin and Duda, 2012, Lin et al., 2012], we assess the accuracy of different PE methods in simulating the propagation and scattering of sound in underwater seamount environment. These benchmark solutions are also important as it could facilitate the benchmark and improvement of different propagation models in the future.

5.1 Validation against coupled mode method

We first consider a conical seamount waveguide with a pressure-release free surface and a penetrable bottom. The water column has a depth of $250m$ with c_1=1500m/s and ρ_1=1.0g/cm^3. A point source with unit strength is placed at (x,y,z)=(0,0,100m). A conical seamount is located 800m from the point source. The geometry of the seamount is based on the study by Luo and Schmidt [2009] as shown in Fig.5-1. The slope of the seamount is $\theta \approx 17°$ which is sharper than most existing studies by 3D PE models [Xu et al., 2016]. The properties of the seamount is the same as the bottom with c_B=1800m/s, ρ_B=2.0g/cm^3 and medium attenuation α=0.1dB/λ. The computational domain size is 2.5km$\times$ 2.5km$\times$ 250m. The source frequency is defined as f=40Hz. PFFT-BEM uses quadrilateral elements with $\Delta l = \lambda/8$ and $\lambda/12$. We compare TL obtained using PFFT-BEM and the axisymmetric coupled mode method of Luo and Schmidt [2009] at different x-locations with (y,z)=(0,100m). As shown in Fig.5-2(a), our numerical results compares well with the coupled mode method results. TL obtained by PFFT-BEM at different x-locations with (y,z)=(400m,100m) is also plotted in Fig.5-2(a). Significant differences are observed at different $x-$locations with (y,z)=(400m,100m) comparing with the results at different x-locations with (y,z)=(0,100m). TL contour in the horizontal plane at the source depth is also plotted in Fig.5-2(b) in which significant 3D disturbance due to the presence of seamount could be observed. The total computational time for the low frequency seamount with Δl=$\lambda/8$ is 233s with 12 computational nodes (384 CPUs).

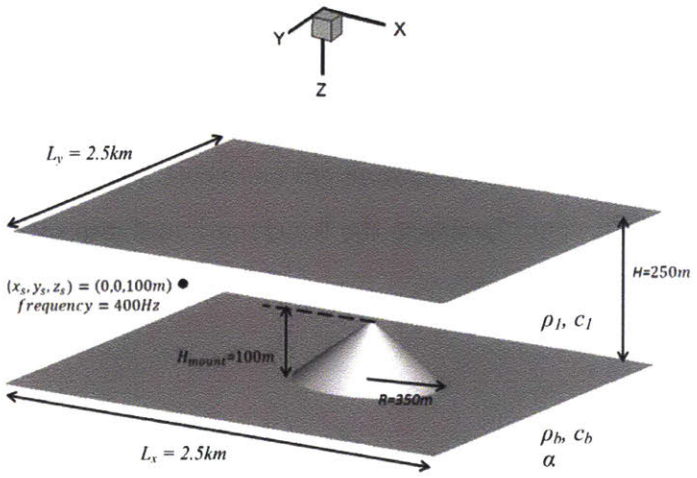

Figure 5-1: Geometry of the waveguide with a conical seamount and a penetrable bottom, seamount height 250m, seamount radius 350m. A 40Hz point source is located at $(x, y, z) = (0, 0, 100m)$ and 800m away from the seamount center.

5.2 Effects of seamount geometries on acoustic scatterings

The geometry of the seamount is expected to have a large effects on acoustics wave scatterings. By conducting numerical simulations of underwater seamount with different geometries, we evaluate the dependence of backscattering, blocking and 3D scattering effects on different seamount geometry parameters. We can therefore examine the validity of $N \times 2D$ and the axisymmetric coupled mode method [Luo and Schmidt, 2009] for general shape seamount. The source properties are kept to be the same with the ones in section 5.1.

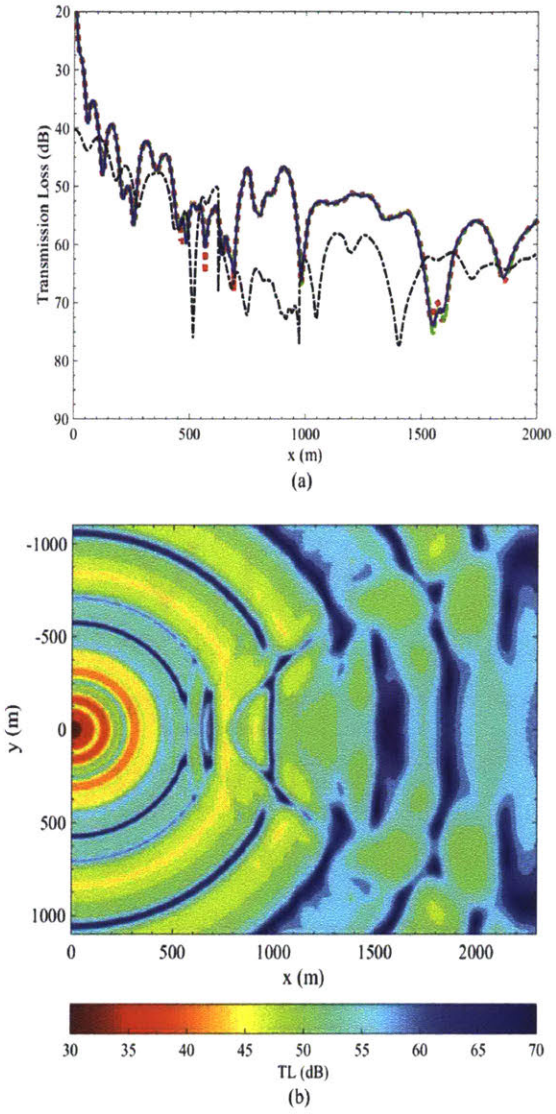

Figure 5-2: (a) TL comparison at different $x-$locations with $(y, z) = (0, 100m)$ for 3D underwater seamount with $f = 40Hz$ between coupled mode method [Luo and Schmidt, 2009] (red line) and 3D direct simulations by PFFT-BEM with 8 elements per wavelength (blue line) and 12 elements per wavelength (green line); TL at different $x-$locations with $(y, z) = (400m, 100m)$ by PFFT-BEM with 12 elements per wavelength (black line); the green and blue line overlap with each other in the figure. (b) TL obtained using PFFT-BEM on the $x - y$ plane at $z = 100m$.

5.2.1 Seamount height

First, we illustrate the relation between the seamount height and the significance of seamount 3D scattering, backscattering and blocking effects. Here, we change the height of the conical seamount from 50m to 150m and compare the transmission loss in the horizontal plane at the source depth z=100m. Fig.5-4 (b) plots the transmission loss of the 3D numerical simulation results from PFFT-BEM versus the 2D approximation results in the direction tangential to the seamount cross section. This comparison can be seen as a direct check for the seamount 3D scattering effects. Because an N×2D method considers only in-plane results, the 2D results in the tangential direction are the same with the waveguide results without a seamount. From comparison in Fig.5-4 (a) and (b), we find that for a small seamount height H_0=50m, the 3D scattering effects is not significant and N×2D approximation gives a good approximation (with errors up to 2dB comparing with the 3D results). When the seamount height rises from 50m to 100m which is plot in Fig.5-4 (c) and (d), the N×2D results deviate from the 3D results (with errors up to 5dB). As the height of the seamount risers to 150m which is plot in Fig.5-4 (e) and (f), the 3D effects become more significant and the N×2D results deviate from the 3D results up to 12dB. In addition, as shown in Fig.5-4(b), (d) and (f), the perturbation zone in the 3D result becomes larger as the seamount height is higher. This also indicates stronger 3D effects.

We then further compare the transmission loss along the x-axis at the source depth to check backscattering and blocking effects by seamounts with different heights. From Fig.5-3, we see that when the height of the seamount is small, both the backscattering and blocking effects are less significant. As the height of the seamount increases from 50m to 100m, the backscattering and blocking effects from the seamount rises with 2-3 dB. As the height of the seamount tip rises to 150m which is at the same depth as source, the blocking and backscattering effect become much more significant (up to 10dB different comparing with the 50m case).

We further compare TL_D, which represent the differences between the TL in the

field with seamount $TL_{seamount}$ and TL without seamount $TL_{background}$. As shown in Fig.5-5, as the height of the seamount rises, the value of TL_D becomes larger in the entire domain which indicates larger scattering effect from the seamount. From the above observations, we can conclude that as the height of seamounts becomes larger, the 3D, blocking and backscattering effects become more significant. These results also indicate that the N×2D model is a poor approximation of the three dimensional model for an underwater seamount with large slope angle. Similar results were also found in Luo and Schmidt [2009].

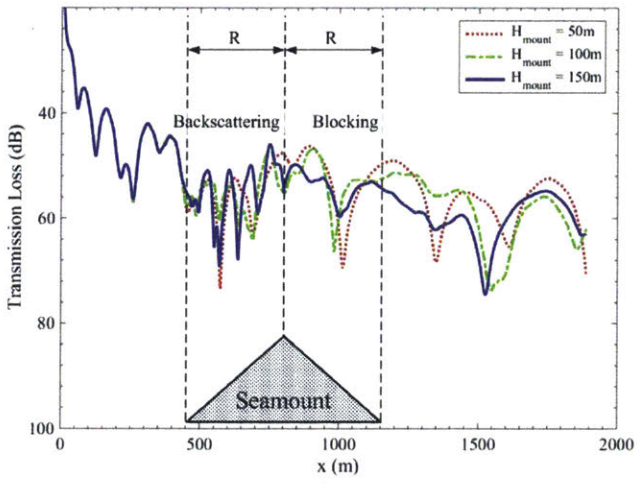

Figure 5-3: TL comparison at different $x-$locations with $(y, z) = (0, 100m)$ for 3D underwater seamount with $f = 40Hz$ with H_0=50m, 100m and 150m.

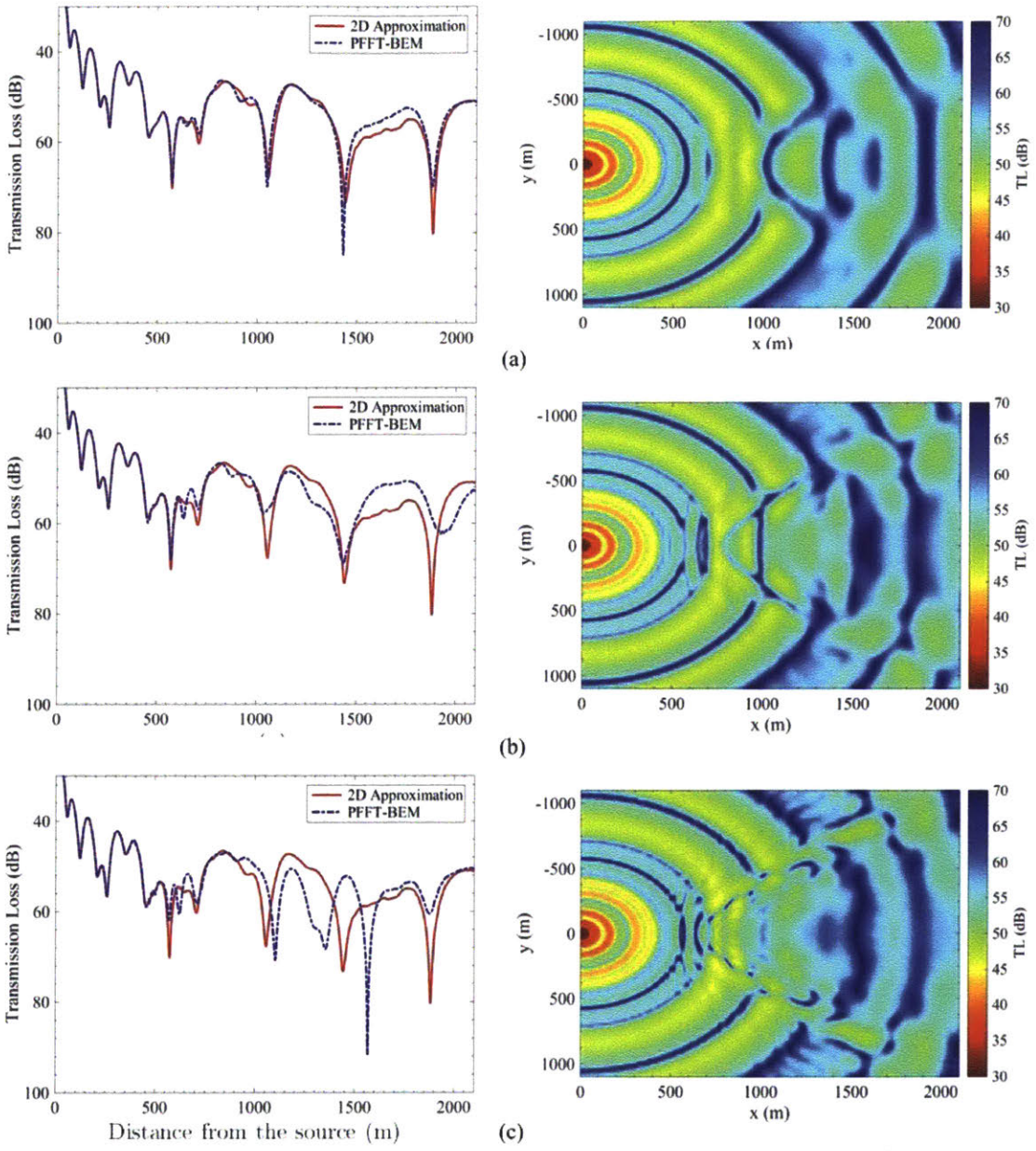

Figure 5-4: TL (as a function of distance from the source) in the direction which is tangential to the seamount cross section: comparison between 3D obtained using 3D direct simulations by PFFT-BEM and 2D approximations (left column) and TL at $x-y$ plane (z=100m) obtained using 3D direct simulations by PFFT-BEM for 3D underwater seamount with $f = 40Hz$ with (a)H_0=50m (b) H_0=100m (c) H_0=150m (right column).

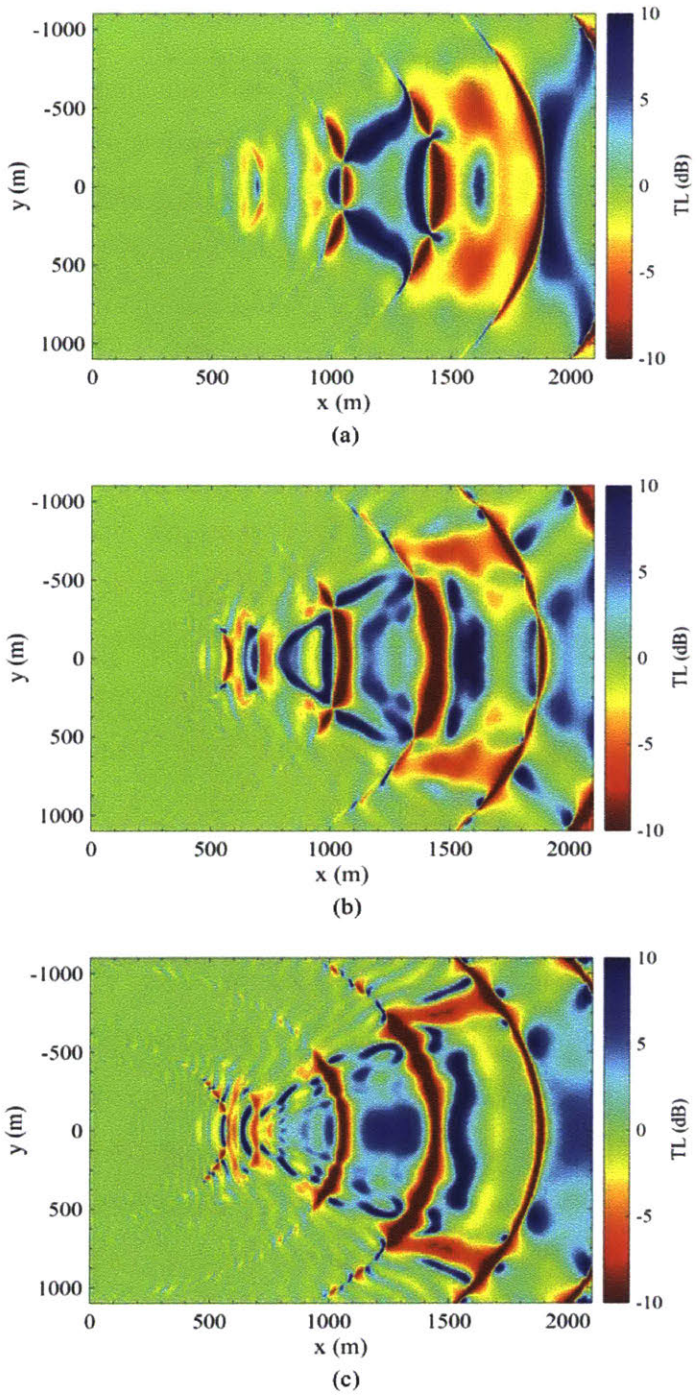

Figure 5-5: TL_D(=$\mathrm{TL}_{seamount}$-$\mathrm{TL}_{background}$) at $x-y$ plane (z=100m) obtained using 3D direct simulations by PFFT-BEM for 3D underwater seamount with $f = 40Hz$ with (a)H_0=50m (b) H_0=100m (c) H_0=150m.

5.2.2 Seamount cross section shape

Recently, 3D propagation models are developed based on coupled mode method for simulating acoustics propagation and scattering in an axisymmetric bathymetry environment. These numerical methods can provide accurate and efficient solutions for 3D underwater bottom features with specified geometries such as cylindrical island [Athanassoulis and Prospathopoulos, 1996] or conical seammounts [Taroudakis, 1996, Luo and Schmidt, 2009]. To assess the applicability of these methods, we study the acoustics scattering problems of shallow water seamounts with different cross section geometries. As shown in Fig.5-7, we conduct direct numerical simulations using PFFT-BEM for the seamounts with different cross section shapes. The geometries of the seamount cross sections are assumed to be ellipse which are not axisymmetric shapes assumed by the coupled mode methods. The aspect ratio of these ellipses $a = R_y : R_x$ is defined in Fig.5-7. Here, R_y is the ellipse radius in the y-direction while R_x is defined as the ellipse radius in the x-direction. The height of the seamount H_0 is kept to be 100m. The source properties and fluid (and bottom) properties are the same as those in the conical seamount case. For all these cases, PFFT-BEM uses uniform quadrilateral elements with $\Delta l = \lambda/8$.

We first fix $R_y = R$ and vary a by changing R_x. The TL in the x-y plane at z=100m is plotted and compared in Fig.5-7. TL_D, which represent the TL differences between simulation with and without seamount, in the $x - y$ plane at z=100m is plotted and compared in Fig.5-8. From these plots, we see that the TL contour changes significantly even with a small change in a. To quantify these differences, we further compare the TL in the horizontal plane at depth z=100m along the x-axis for different seamount cross section shapes. From Fig.5-6, we see that relatively small variations in a can create large changes (up to 10dB) in TL for both backscattering and blocking effects. As a result, we can conclude that using a conical seamount with radius R=R_y to approximate the acoustics scattering by an ellipse seamount would introduce large errors in the backscattering, blocking and azimuthal directions.

In the second case, as shown in Fig.5-10, we fix $R_x = R$ and change the aspect ratio

by changing R_y. The height of the seamount H_0=150m. The other environment and mesh properties are kept same. From Fig.5-10, we can see that relatively variations in the scattering effect by the seamount with different a are not as significant as the ones in first ellipse case. The TL_D, which represent the TL differences between simulation with and without seamount, in the x-y plane at z=100m is plotted and compared in Fig.5-11.

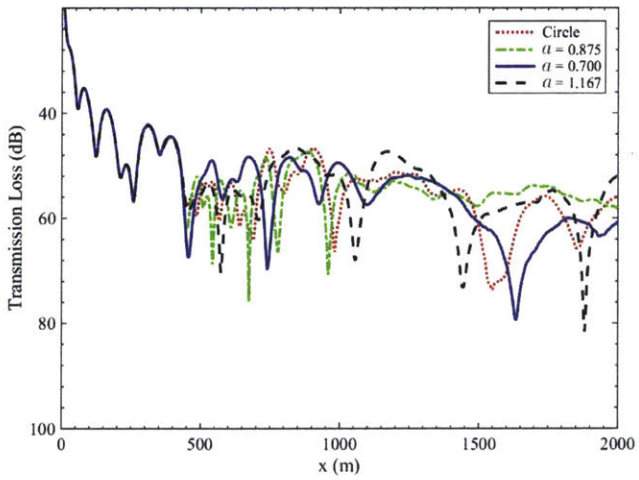

Figure 5-6: TL at different $x-$locations with $(y, z) = (0, 100m)$ for 3D underwater seamount obtained using 3D direct simulations by PFFT-BEM. Here, $f = 40Hz$ with seamount cross section are circle, ellipse with a=0.875, ellipse with a=0.7 and ellipse with a=1.167. R_y is fixed at 350m.

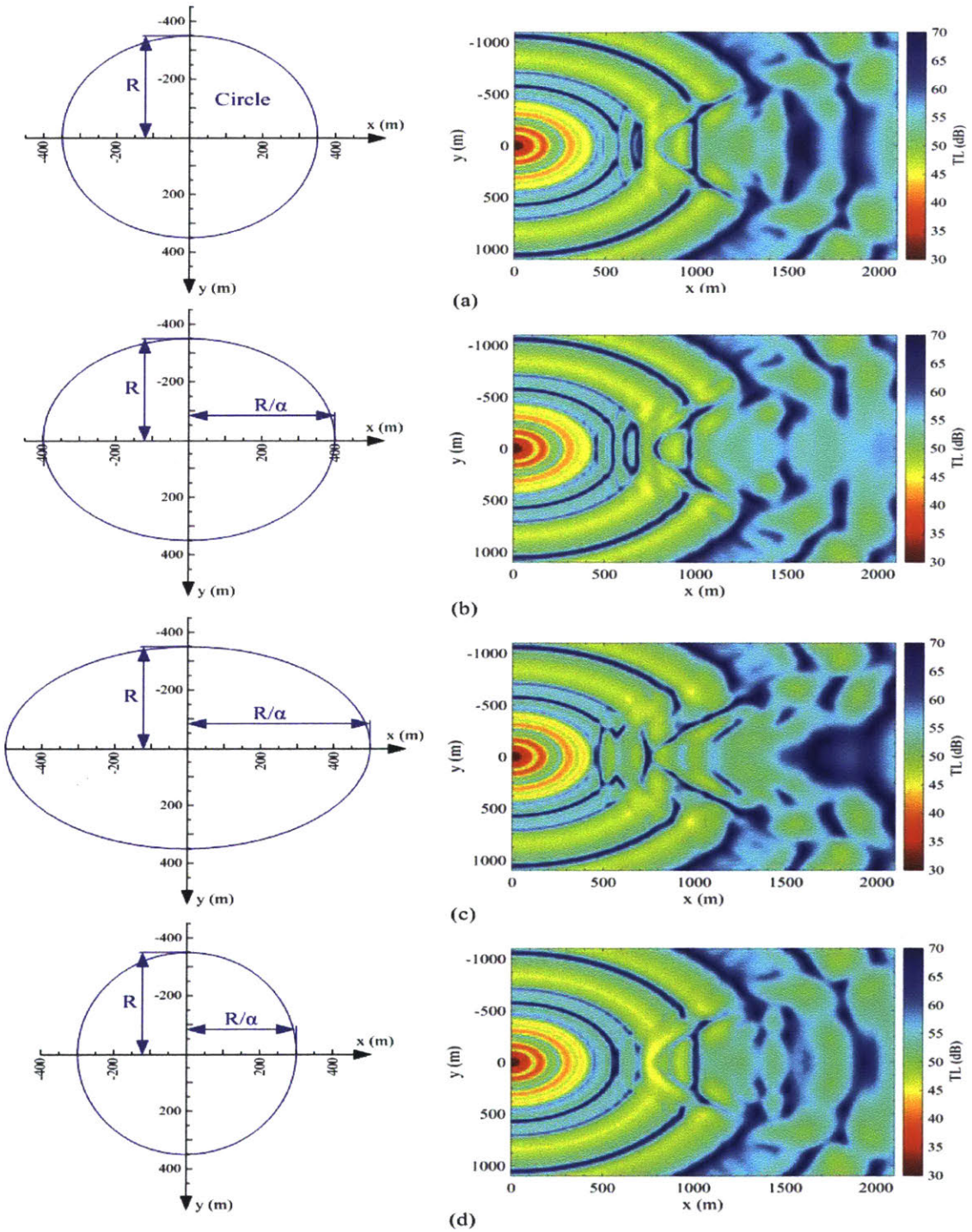

Figure 5-7: Seamount cross section shape at seamount bottom (left column) and TL at $x-y$ plane (z=100m) obtained using 3D direct simulations by PFFT-BEM (right column). Here, $f = 40Hz$ with seamount cross section are (a) circle, (b) ellipse with a=0.875, (c) ellipse with a=0.7 and (d) ellipse with a=1.167. R_y is fixed at 350m.

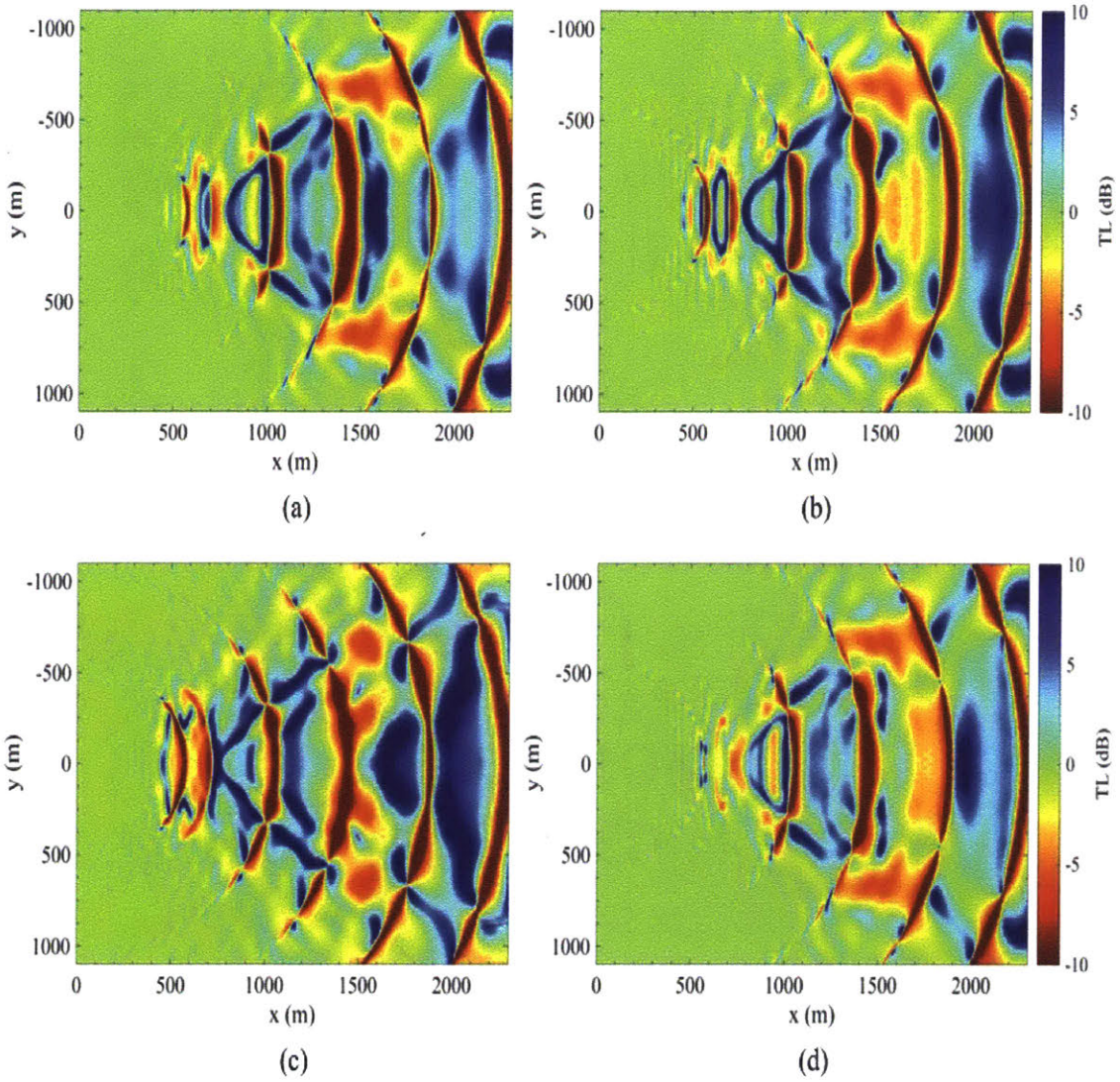

Figure 5-8: TL_D(=$\mathrm{TL}_{seamount}$-$\mathrm{TL}_{background}$) at $x-y$ plane (z=100m) obtained using 3D direct simulations by PFFT-BEM. Here, $f = 40Hz$ with seamount cross section are (a) circle, (b) ellipse with a=0.875, (c) ellipse with a=0.7 and (d) ellipse with a=1.167. R_y is fixed at 350m.

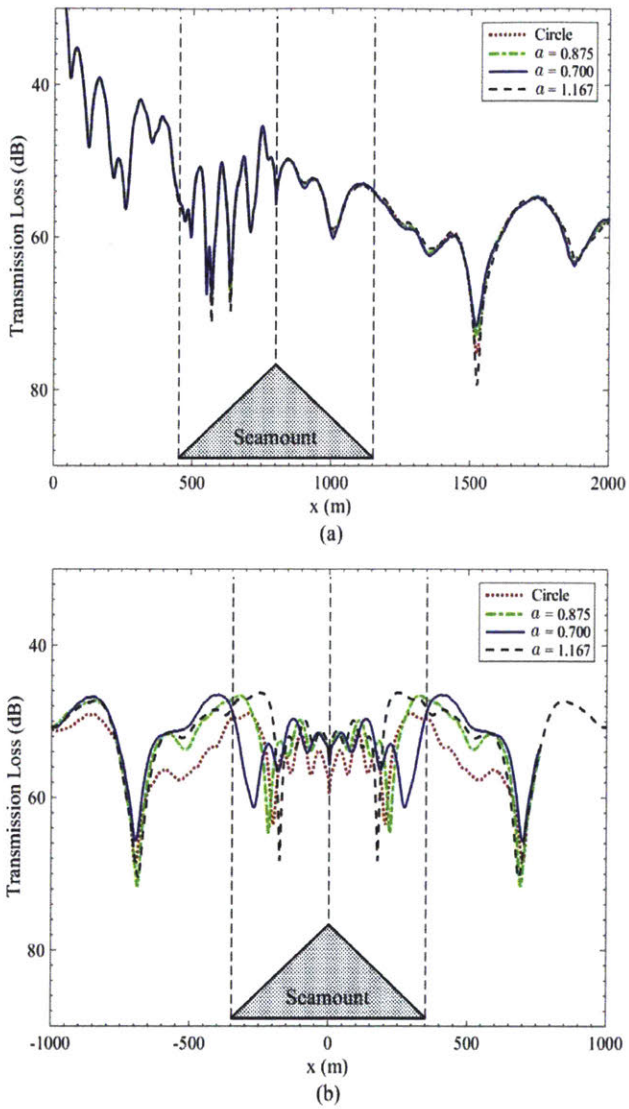

Figure 5-9: (a) TL at different $x-$locations with $(y, z) = (0, 100m)$ for 3D underwater seamount obtained using 3D direct simulations by PFFT-BEM. (b) TL at different $y-$locations with $(x, z) = (800m, 100m)$ for 3D underwater seamount obtained using 3D direct simulations by PFFT-BEM for $f = 40Hz$. Here, $f = 40Hz$ with seamount cross section are circle, ellipse with a=0.875, ellipse with a=0.7 and ellipse with a=1.167. R_x is fixed at 350m.

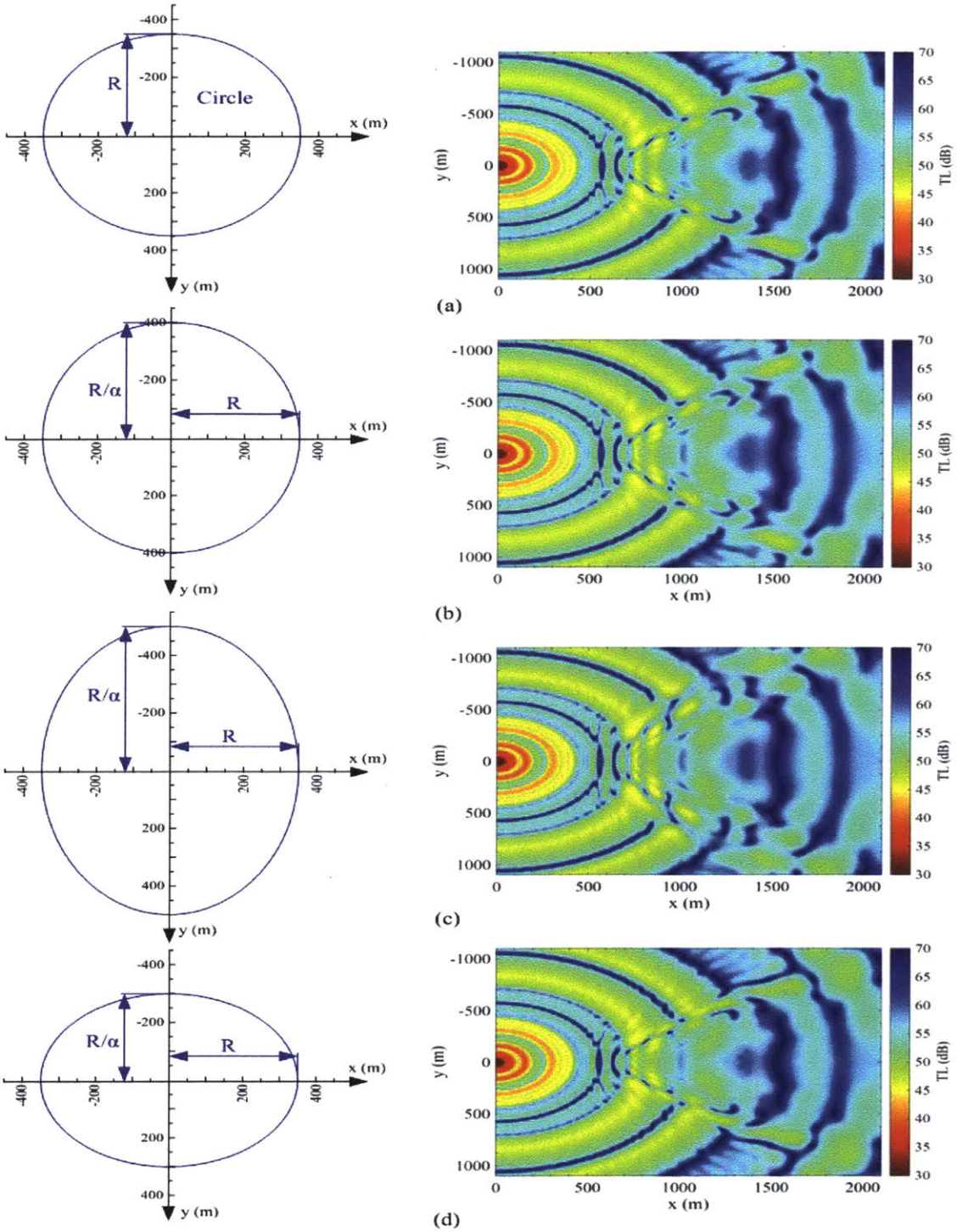

Figure 5-10: Seamount cross section shape at seamount bottom (left column) and TL at $x-y$ plane (z=100m) obtained using 3D direct simulations by PFFT-BEM (right column). Here, $f = 40Hz$ with seamount cross section are (a) circle, (b) ellipse with a=0.875, (c) ellipse with a=0.7 and (d) ellipse with a=1.167. R_x is fixed at 350m.

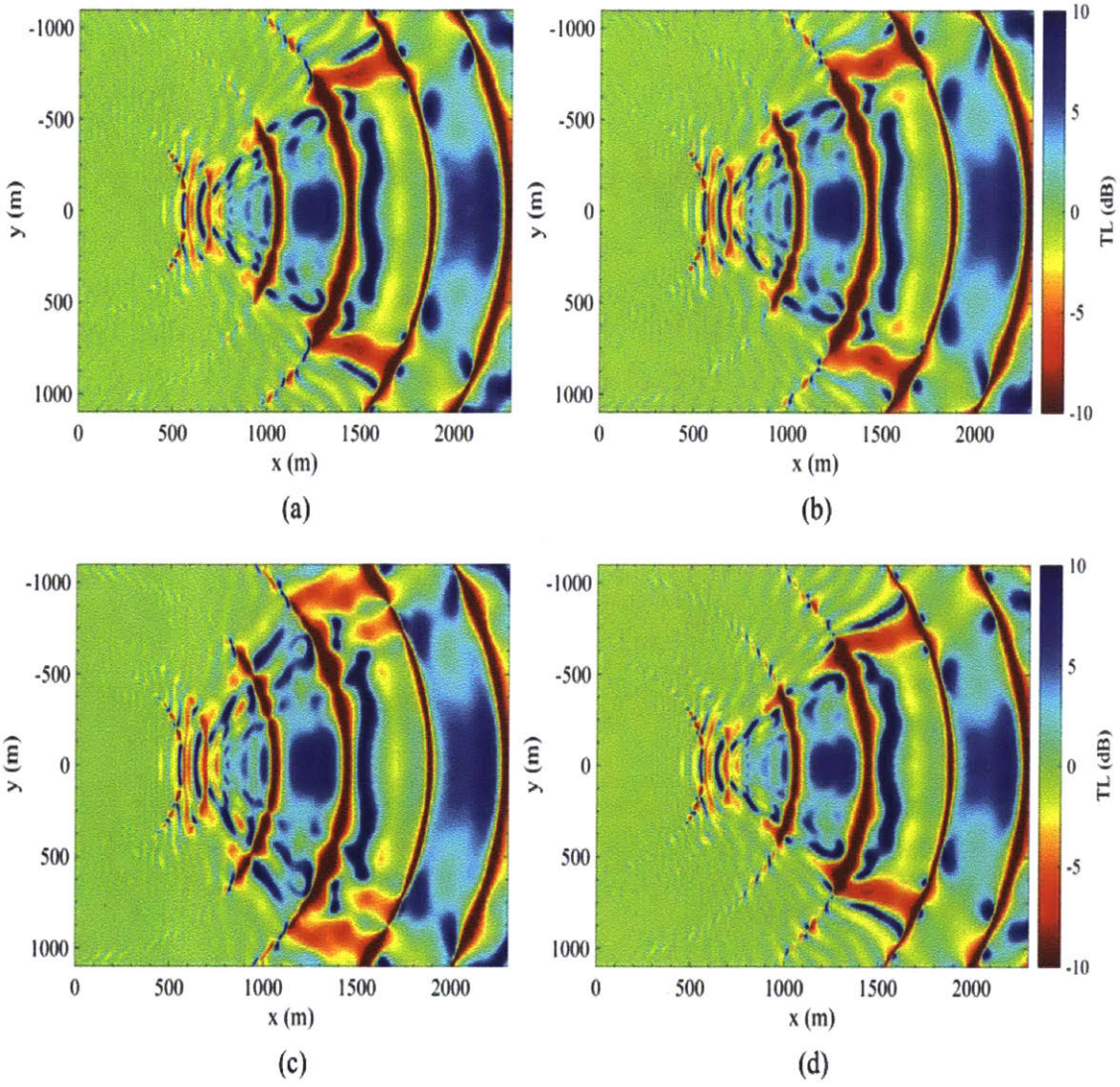

Figure 5-11: TL_D(=$\mathrm{TL}_{seamount}$-$\mathrm{TL}_{background}$) at $x-y$ plane (z=100m) obtained using 3D direct simulations by PFFT-BEM. Here, $f = 40Hz$ with seamount cross section are (a) circle, (b) ellipse with a=0.875, (c) ellipse with a=0.7 and (d) ellipse with a=1.167. R_x is fixed at 350m.

From comparison, we find that the differences among the cases with difference aspect ratios are mostly located in the azimuthal directions when keeping $R_x = R$. From Fig.5-9(a) which plots the TL along the x-axis from the source point, we see

that the variations in aspect ratio a do not create visible changes in TL for both backscattering and blocking effects. As a result, the conical seamount approximation could provide a generally good approximation of the blocking and backscattering effects when keeping R_x=R. On the other hand, Fig.5-9(b) plots the TL along the y-direction across seamount tip. This measures the strength of 3D scattering by the seamount. From Fig.5-9(b), we observe large variations (up to 10dB) in transmission loss for different a. Therefore, small variation in a can introduce large changes in TL for 3D scattering effects. This indicates that the conical seamount approximation by the coupled mode method cannot provide accurate predictions of the seamount 3D scattering effects.

5.3 Difference between low frequency and higher frequency scattering by the underwater seamount

A higher frequency case (with source frequency $f = 400Hz$) is also considered. The fluid and bottom properties are kept to be the same. PFFT-BEM uses uniform quadrilateral elements with $\Delta l = \lambda/8$. The TL obtained by PFFT-BEM at different $x-$locations with $(y, z) = (0, 100m)$ and at different $y-$locations with $(x, z) = (800m, 100m)$ are compared with the PFFT-BEM results with source frequency $f = 40Hz$. It should be noted that the source is located at $(x, y, z) = (0, 0, 100m)$ while the peak of the seamount is at $(x, y, z) = (800m, 0, 100m)$ which is marked by the dash lines in Fig.5-12. From Fig.5-12(a), it can be seen that the backscattering effects from the seamount is more significant when $f = 400Hz$ (the TL is nearly $10dB$ smaller than the case with $f = 40Hz$ in front of the seamount). From Fig.5-12(b), it can also be seen that the 3D scattering effects in the azimuthal direction from the seamount is more significant in the $f = 400Hz$ case (the TL is nearly $5dB$ smaller than the case with $f = 40Hz$ at the side of the seamount). From these results, we can see that as the frequency of the sound source becomes larger, the backscattering, blocking and 3D scattering effect all becomes more significant.

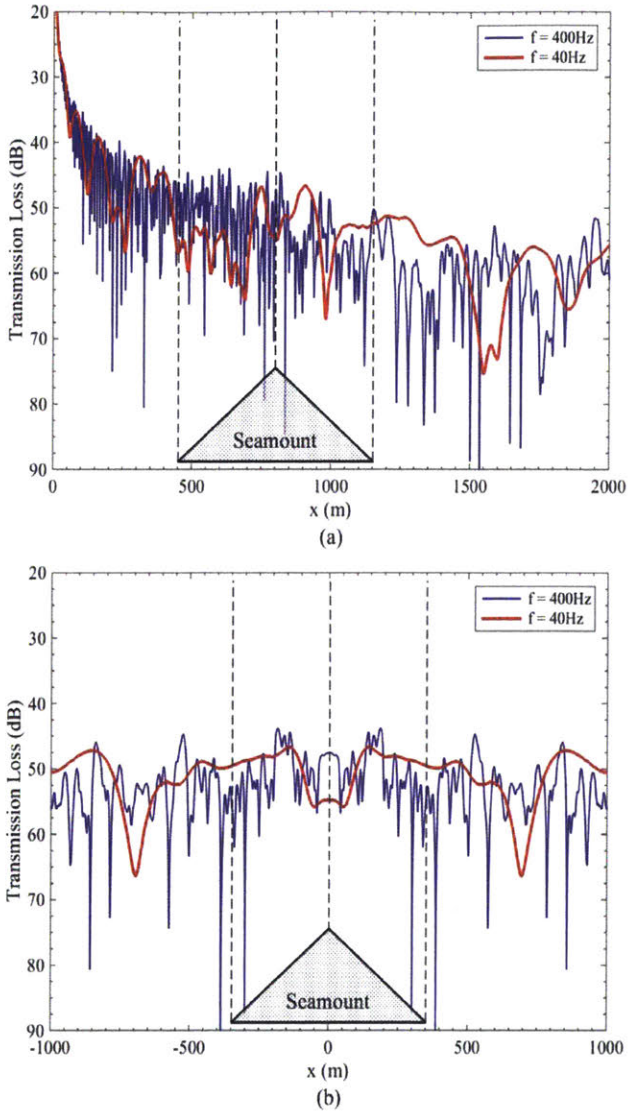

Figure 5-12: (a) TL at different $x-$locations with $(y, z) = (0, 100m)$ for 3D underwater seamount obtained using 3D direct simulations by PFFT-BEM for $f = 400Hz$ and $f = 40Hz$. (b) TL at different $y-$locations with $(x, z) = (800m, 100m)$ for 3D underwater seamount obtained using 3D direct simulations by PFFT-BEM for $f = 400Hz$ and $f = 40Hz$.

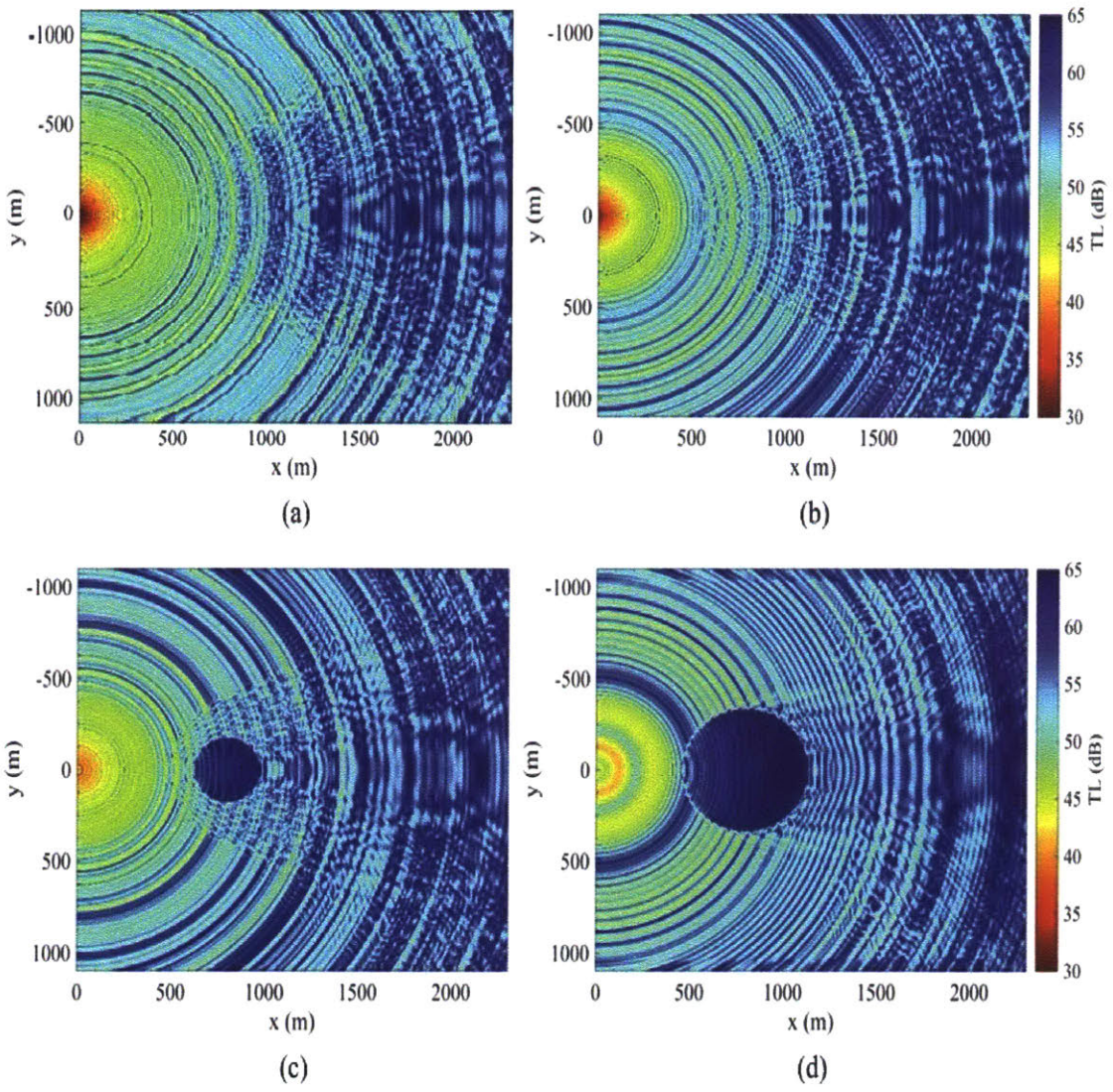

Figure 5-13: (a) TL obtained using PFFT-BEM on the $x-y$ plane at $z = 100m$. (b) TL obtained using PFFT-BEM on the $x-y$ plane at $z = 145m$. (c) TL obtained using PFFT-BEM on the $x-y$ plane at $z = 200m$. (d) TL obtained using PFFT-BEM on the $x-y$ plane at $z = 245m$. ($f = 400Hz$)

The TL contour in the horizontal plane at the different depths are also shown in Fig.5-13. It can be seen that the 3D scattering effects from the seamount changes significantly with different water depths. Significantly stronger (up to 10dB) backscat-

tering and blocking effects for the deeper cases are observed due to presence of the seamount. This numerical example indicates the backscattering effect can be important for cases with high frequency source and neglect the backscattering effects, which is assumed in PE method, could introduce large error to the numerical results. The total computational time for the higher frequency seamount is 6hrs with 60 computational nodes.

5.4 Seamounts with realistic environment/geometry

One of the research objective in this chapter is to provide direct numerical benchmark solutions under realistic conditions or real underwater seamount geometries. This would be useful in understanding the importance of 3D sound scattering by underwater seamount in shallow water conditions as well as facilitating the development and validation of approximation/theoretical methods. To achieve this goal, two numerical simulatios are conducted and presented here: the sound field scattering by a seamount in New Jersey Shelf environment and a double seamount problem.

5.4.1 Prediction of 3D (spatial) sound scattering due to presence of a seamount in New Jersey continental shelf

The sound propagation and scattering effects by seamount under realistic environment conditions are numerically simulated and studied here. The 3D multi-layer PFFT-BEM method has been used to obtain the propagation and scattering of sound over an underwater seamount on the slope of New Jersey shelf. The sound speed profile and bathmetry shown in Fig.5-14 are based on the data from Lin [2016]. The origin of the coordinates used in this problem is located above the source at the sea surface with z-axis pointing into the sea. The source is located at (0, 0, 50)m. The multi-layer model is used in the present study with water column sound profile shown in Fig.5-14 and uniform fluid density ρ=1.024g/cm^3. The bottom layer is modeled with sound speed c_b=1700m/s, ρ_b=1.5g/cm^3 and α=0.5dB/λ. Due to the detailed 3D

bathmetry of the shelf is unknown, we approximated the bottom feature, shown in Fig.5-14 at 340m depth, as a 3D conical seamount with H_0=100m, R=350m. The center of the seamount is located at (5565, 0, 340)m. The numerical simulation of the sound propagation and scattering over the seamount are conducted with a computational domain of $8km \times 4km \times 0.5km$ and with uniform quadrilateral elements of size $\Delta l = \lambda/8$. Fig.5-16 and Fig.5-15 shows the TL obtained using PFFT-BEM on the $x - z$ plane at y=0m without the seamount (a) and with the seamount (b). From comparison, several observations can be made. First, the numerical acoustic data shows that a significant decrease in sound intensity as it propagates through the sea bottom. Secondly, by comparing the numerical results with and without the underwater seamount, we show strong blocking and backscattering effects (5$\sim$15dB) due to presence of (shallow water) bottom seamount.

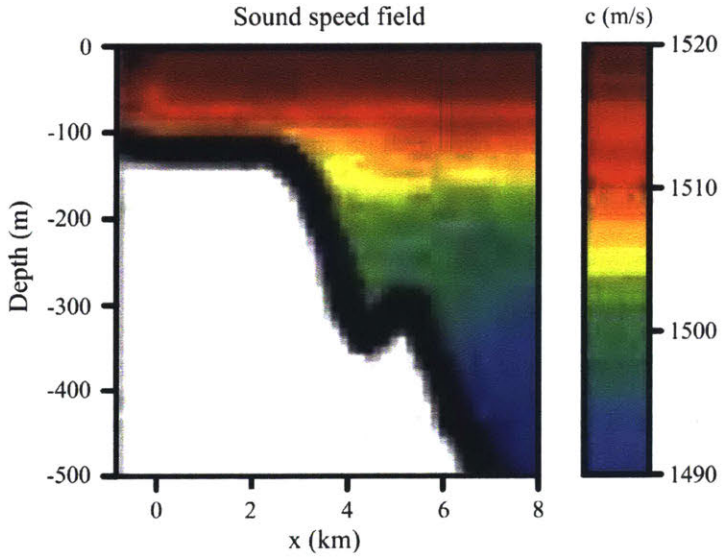

Figure 5-14: The sound speed distribution and bathymetry on the slope of the New Jersey Shelf

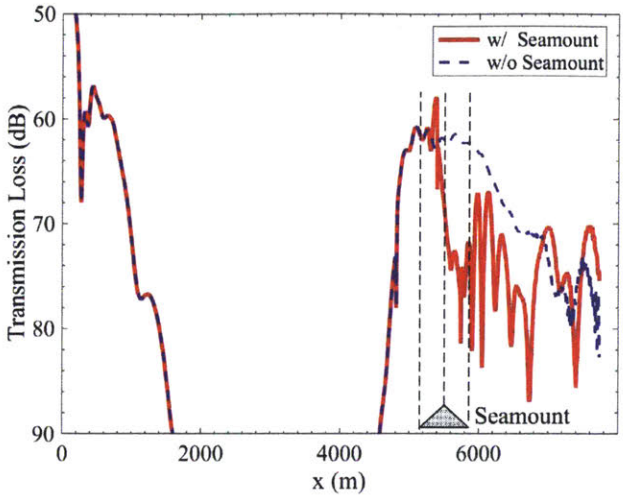

Figure 5-15: TL comparison at different $x-$locations with $(y, z) = (0, 290m)$ for 3D underwater seamount with seamount and without seamount.

5.4.2 Prediction of 3D (spatial) sound scattering due to double seamount

The second problem contains a double seamount, which is in fact inspired by a real world environment. The bathmetry of this double seamount problem is demonstrated in Fig.5-17. The origin of the coordinate system is located at the free surface with the z-axis pointing down to the ocean. The sound source is located below the origin of the coordinate system with (x_s,y_s,z_s)=(0m, 0m, 250m) and frequency f=100Hz. The tip of the first seamount is at (x,y,z) = (3500 m, 1000 m, 200 m). The tip of the second seamount is at (x,y,z) = (3500 m, -1500 m, 200 m). The slope of both seamounts is 1/4. The radius of both seamounts are 2500 m. The water depth away from the seamount is 825 m. The water is iso-speed with sound speed c_w=1500m/s and ρ_w=1g/cm^3. The sea bottom is also iso-speed with sound speed c_b=1650m/s, ρ_w=1.5g/cm^3 and bottom loss α=0.5dB/λ. In this case, the numerical simulation of the sound propagation and scattering over the seamount are conducted with a computational domain of $8km \times 6km \times 0.8$km with uniform quadrilateral elements of $\Delta l = \lambda/8$.

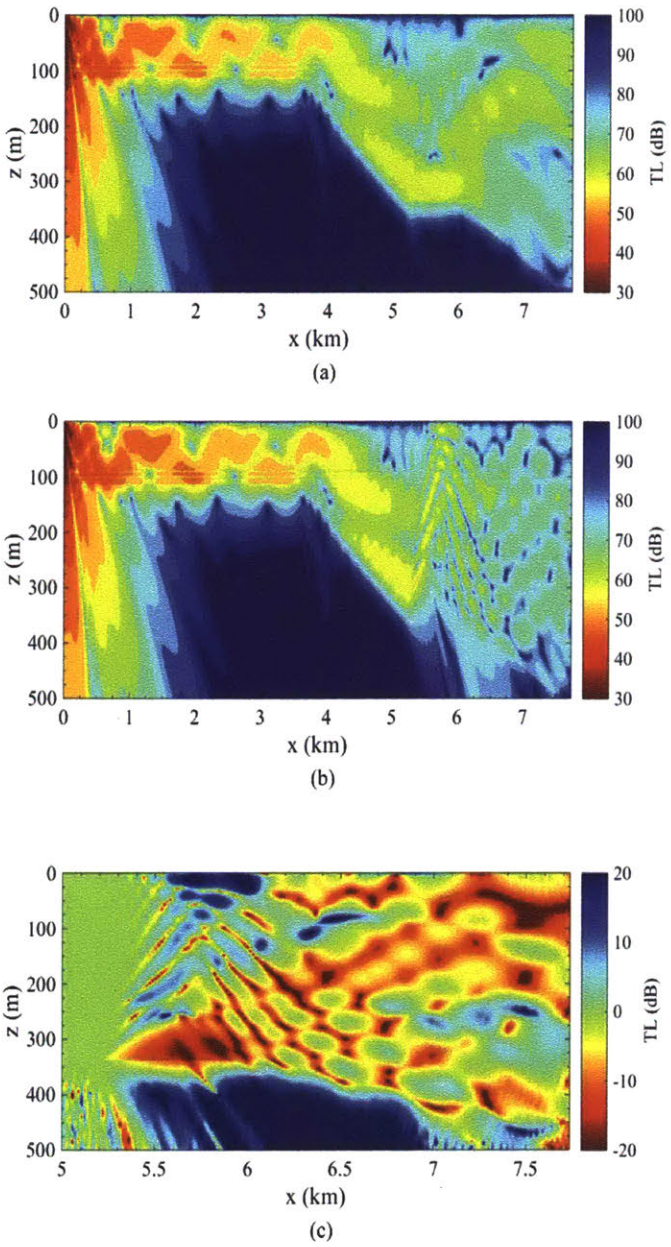

Figure 5-16: TL obtained using 3D PFFT-BEM on the $x - z$ plane at $y = 0m$ (a)without seamount and (b) with seamount (seamount base at $z = 340m$) (c) Differences between TL's obtained with and without seamount.

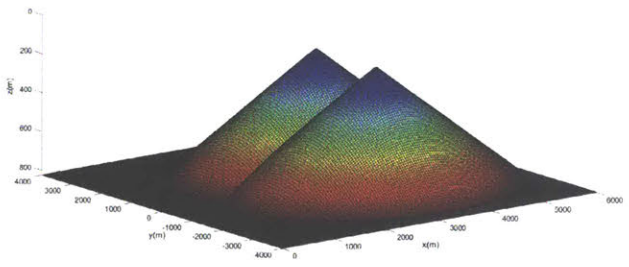

Figure 5-17: The double seamount geometry: The tip of the first seamount is at $(x, y, z) = (3500m, 1000m, 200m)$. The tip of the second seamount is at $(x, y, z) = (3500m, -1500m, 200m)$. The slope of both seamounts is $1/4$. The radius of both seamounts are 2500 m. The water depth away from the seamount is 825 m.

Three-dimensional models based on the parabolic equation method have been used here for comparison. As is well known, parabolic equation models are suitable for treating underwater acoustic propagation problems in cases only where no significant backscattered field is expected. In the present study, three PE solutions [Lin and Duda, 2012, Lin et al., 2012] using different discretization schemes are compared with the PFFT-BEM results. The transmission loss in the x-y plane at depth of 400m is plot and compared in Fig.5-18. From comparison, it is seen that the fixed arc-length scheme (Fig.5-18(b)) and fixed radius-length scheme (Fig.5-18(d)) in a cylindrical coordinate system give the best PE solutions. The Cartesian PE scheme (Fig.5-18(c)) could only give good solutions close to the solution marching direction (the x-axis). From observation, it is also clear that all the PE results underestimate the backscattering effects in front of the seamount.

To further check the backscattering effects, we change the source location to z_s=400m which is closer to the double seamounts. The transmission losses for scattering acoustics pressure are plotted in Fig.5-19 at different depths. As shown in Fig.5-19, the backscattering effects is much stronger (up to 10 dB) at the source depth (z=400m) when comparing with the ones at other depths.

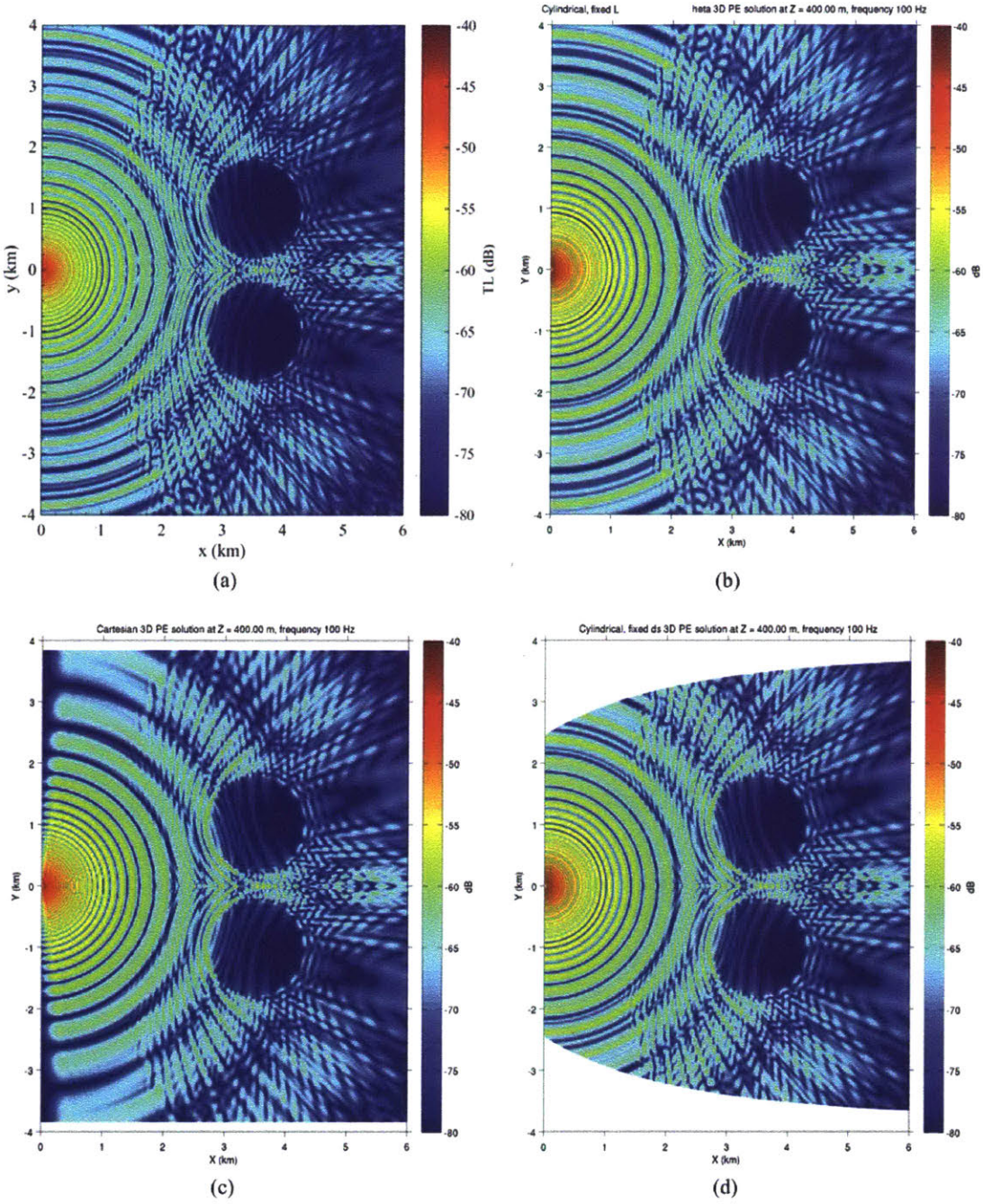

Figure 5-18: TL on the $x-y$ plane at $z = 400m$ obtained using (a) 3D PFFT-BEM (b) PE method with fixed arc-length scheme (c) PE method with cylindrical coordinate system (d) PE method with fixed radius-length scheme.

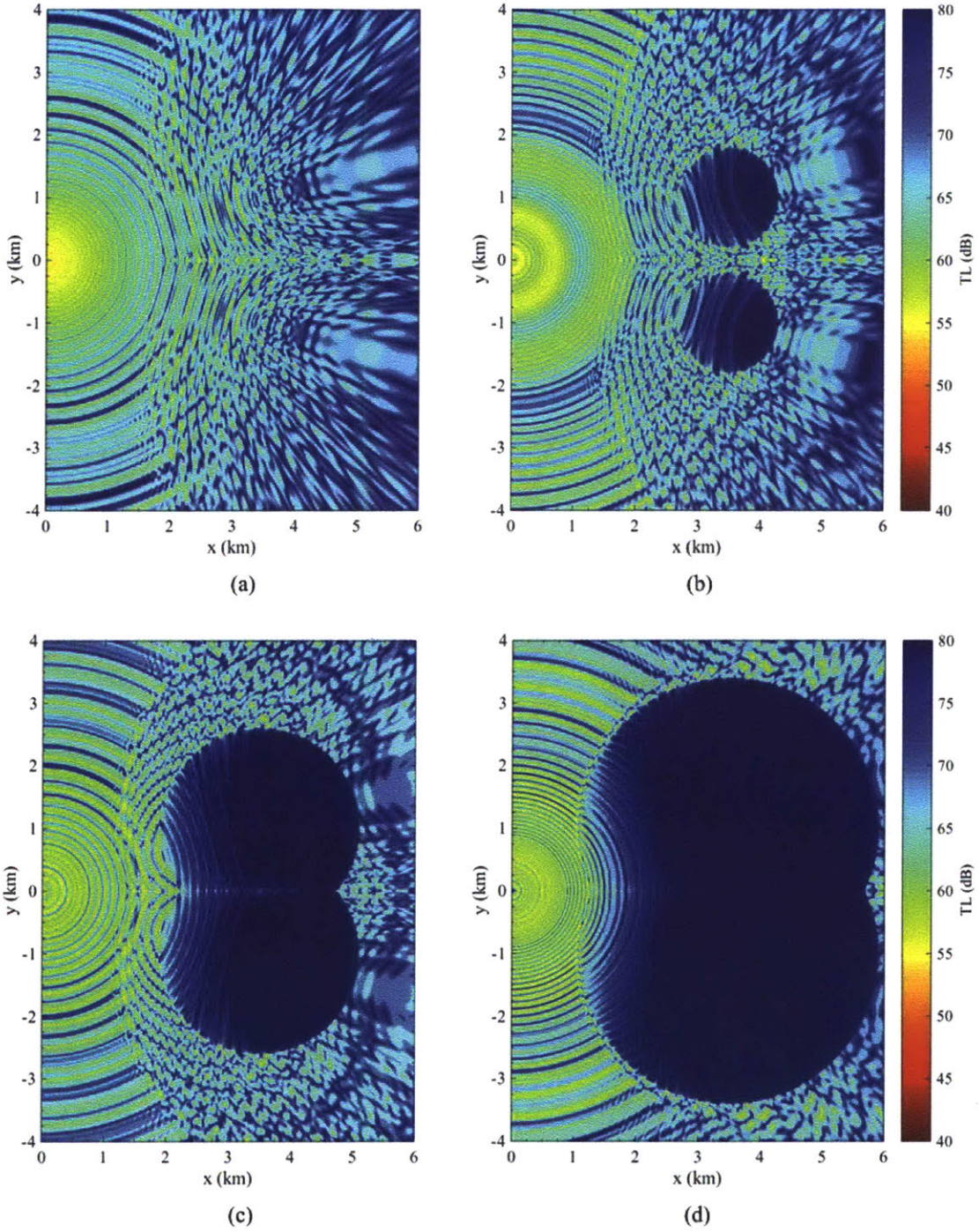

Figure 5-19: TL of the scattering pressure on the $x-y$ plane with source located at 400m (a) at z=200m, (b) at z=400m, (c) at z=600m, (d) at z=800m.

5.5 Concluding remarks

The PFFT-BEM method is a very efficient and accurate method to solve shallow water range-dependent problems. In this chapter, we apply the PFFT-BEM method to analyze the propagation and scattering around underwater seamounts. From numerical examples, we show that 3D coupling effects in azimuthal directions can be important for certain seamount geometry (i.e. seamount with large slope). Under this condition, the N×2D approach is not a good approximation of the true 3D approach. The dependences of the 3D scattering, backscattering and blocking effects on the seamount cross section shapes are also illustrated through numerical examples. We show that the 3D scattering effects by an ellipse seamount differs significantly with the one of a conical seamounts. In such a situation, true 3D numerical models are required especially for 3D scatterings. Two benchmark solutions are presented: seamount on the New Jersey shelf slope and double seamount problems. We simulate and discuss the seamount backscattering and blocking effects in both cases using 3D PFFT-BEM. From comparison with different 3D PE solutions, we assess the accuracy of different 3D PE methods in simulating 3D scattering problems.

Chapter 6

Conclusion and future works

6.1 Conclusion

We develop a highly efficient multi-layer boundary element method for large scale acoustics propagation and scattering in shallow water environment with complex medium and boundaries. The method is based on the integration of the pre-corrected fas Fourier transform (PFFT) algorithm into the constant boundary integral solver. The developed PFFT-BEM reduces the computational operations for the boundary value solution from $O(N^{2\sim3})$ (for conventional boundary element method) to O(N log N), where N is the total number of boundary unknowns. We demonstrate the high efficiency and robustness of PFFT-BEM by comparing the its computational cost with conventional BEM for solving a canonical shallow water acoustics problem: Pekeris waveguide problem. To further improve the efficiency of the PFFT-BEM solver, we optimized the PFFT-BEM scheme by examining the accuracy dependence of the PFFT-BEM on key numerical parameters such as the size of the near field and the boundary mesh sizes. By making use of the Mesh-Neighbor-based (MN) preconditioner, we further improved the convergence of PFFT-BEM iterative solver for 2+ orders. With high performance library (e.g. PETSc and FFTW3), we implemented PFFT-BEM on massively parallel HPC platforms to achieve linear CPU scalability up tp O(1000) CPUs. The PFFT-BEM is able to account for cases with: (a) Inhomogeneity of water properties. (b) Internal and surface waves. (c) Complex/realistic

topography. (d) Multiple-scale reverberation/scattering by bottom and water surface.

For validation, we present study of three sample three-dimensional underwater acoustic propagation and scattering problems: Pekeris waveguide problem, ASA wedge problem and the Gaussian canyon problem. For all these problems, the PFFT-BEM simulation results compare well with existing theoretical and numerical results. Good qualitative agreement are also obtained between the 3D+T simulation results and the experimental data for internal wave and salt wedge cases which involves realistic ocean conditions. This demonstrates the practical simulation capability of PFFT-BEM for 4D (3D+T) underwater acoustics scattering problems.

Two underwater acoustics problems, which are of scientific interest and practical importance, are then investigated in detail: acoustics scattering from a 3D pressure-release rough surface and 3D acoustics propagation/scattering around a shallow water seamount.

For the first problem, PFFT-BEM method has been used to perform Monte Carlo computation of 3D acoustics scattering from rough surfaces. By using 3D PFFT-BEM, we investigate and obtain the validity regions of different approximate models for the 3D rough surfaces scattering such as the first- and second-order perturbation theories and Kirchhoff approximation. From comparing the 2D validity regions and 3D validity regions of these models, we find that the 3D validity regions are shifted to larger kl regions. The 3D acoustic scattering from rough surface at low grazing angle is also studied in this study. From numerical results by PFFT-BEM, it is found that the perturbation theory remains to be a good approximation until very small incident grazing angle ($\theta_g < 20°$) while Kirchhoff approximation only provides accurate results when incident acoustic wave is close to the normal direction of the rough surface ($\theta_g \sim 90°$). This result indicates that for 3D rough surfaces with large kl and moderate kh, direct numerical simulation is required in order to obtain an accurate backscattering result, especially for low grazing angles.

We then apply the PFFT-BEM method to analyze the propagation and scattering around a shallow water seamount. From numerical examples, we show that 3D coupling effects in azimuthal directions can be important for certain seamount geometry

(i.e. seamount with large slope). When the azimuthal variation is strong, the out-of-plane scattering can not be neglected and therefore, as shown by the results, the N×2D approach is not a good approximation of the true 3D approach. The dependences of the 3D effects, backscattering and blocking effects on the seamount cross section shapes are also illustrated through numerical examples. The numerical examples show that the scattering effects by the seamount with ellipse cross section shape differ with the ones by conical seamounts. In such situation, 3D numerical models are required especially for modeling the 3D scatterings. Two solutions are then presented: seamount on the New Jersey shelf slope and a double seamount problem. The backscattering and blocking effects by the seamount in both cases are simulated and discussed using PFFT-BEM. From comparison with different 3D PE solutions, we assess the accuracy of different 3D PE methods in simulating 3D scattering problems. By comparison the results of the double seamount problem at different depths, the importance of backscattering effect by the seamount is also discussed.

6.2 Future works

We have developed an O(N) multi-layer boundary-element method, PFFT-BEM for shallow water acoustic propagation which utilizes a Pre-corrected Fast Fourier Transform (PFFT) approach to reduce the computational effort from $O(N^{2\sim3})$ to O(N) where N is the total number of boundary unknowns. The method is capable of accounting for complex topography, inhomogeneity of water properties, and dynamic environments associated with complex coastal and estuarine conditions. The method is benchmarked against theoretical cases and field experiments. For realistic modeling and forward prediction in practical estuarine environments, and especially for achieving inversion of the sensed acoustics to characterize and predict the geometry and environment in such complex problems, a number of extensions and developments needs to be accomplished in the future.

I. Develop of $O(N^{2/3})$ PFFT-BEM method for shallow layers with large horizontal extent.

In shallow depth, the influence of three-dimensional acoustic wave propagation in the far field can be determined by the Taylor series expansion about a reference horizontal plane. By use of this expansion, the influence of the three-dimensional wave fields can be represented in terms of a small number of two-dimensional problems. For the two-dimensional problems, the PFFT approach is again applied with the total number of unknown reduced from N (in the 3D problem) to $N^{2/3}$. The resulting computational count then becomes $O(N^{2/3})$. This advantage shall be effective for the shallow water problem at the large horizontal extents with relatively low acoustic frequency. The potential gain in efficiency can be game changing, which could increase the effective N from $O(10^{10})$ to $O(10^{15})$ using the same computational time. This will achieve speedup of $O(10^{3\sim5})$ for realistic applications requiring $O(10^{9\sim15})$ unknowns.

II. Develop time-domain version of PFFT-BEM to achieve true 4D acoustic predictions

For another direction of the future work, a time-domain version of PFFT-BEM can be developed. Such a capability will be efficacious for true transient environmental and acoustic problems including Doppler effects associated with fast moving sources, and scattering by fast deforming boundaries. To do that, the BEM formulation and solution in the frequency domain need to be modified to the time domain, incorporating time-varying source position/speed, and boundary deformations. The time domain boundary integral equation on the domain boundary $\vec{x} \to S$ could be formulated as

$$\begin{aligned} 2p(\vec{x},t) = \int_0^t \iint_S [G(\vec{x},t|\vec{\xi},\tau)]p_n(\vec{\xi},\tau) \\ -\frac{\partial G}{\partial n}(\vec{x},t|\vec{\xi},\tau)dS(\xi)d\tau - \int_0^t \iint_{S_0} a(\vec{\xi},\tau)G(\vec{x},t|\vec{\xi},\tau)dS_0 d\tau \end{aligned} \tag{6.1}$$

Here, G is the time domain Green function as

$$(\vec{x},t|\vec{\xi},\tau) = \frac{\delta(t-\tau-R/c)}{4\pi R} \tag{6.2}$$

with $R=|\vec{x}-\vec{\xi}|$ and δ is the Dirac delta function. The last term on the right hand of

Eq.(6.1) represents the moving source with surface S_0 and strength $a(\vec{\xi}, \tau)$. By obtaining the 4D time-domain O(Nlog N) PFFT-BEM direct solution, we can study the problem with large source speeds and surface/internal waves propagation at (small) oblique angles to acoustic propagation direction, under which time-domain effects (such as Doppler effects) are significant.

III. Develop O(N) solution to the acoustic inversion problem incorporating fast forward capability based on the adjoint formulation

Characterization and prediction of the geometry and environment for complex problems is another interesting topic which needs to be further investigated. The inversion of the acoustics measurements could be achieved using Conjugate gradient method. By incorporating fast forward capability using developed PFFT-BEM to the acoustic inversion problem, we could obtain fast inversion of the measured acoustics data. The computational cost of this direct method is thus $O(N \log NP)$ with P the inversion unknowns. As a result, the adjoint approach is essential for large number of inversion unknowns P, while the direct method is sufficient for small P. The key challenges are the conditioning of the problem, and the minimization of the number of optimization iterations/evaluations N_{opt} (independent of N and P).

IV. Apply PFFT-BEM direct simulations to forward and inverse problems of 3D and 4D underwater acoustics

After the above development of the PFFT-BEM method, we can then study the realistic, practical problems such as the acoustics of the Mouth of the Columbia River, the Connecticut River, and Regional Ocean Modeling System (ROMS) predicted domains/environments to obtain validation and corroboration to measurements and to available approximate model predictions. By studying these practical problems, the importance of sufficient modeling resolution; the acoustic effects of complex surfaces and bottoms; the surface/internal wave (spectral) amplitudes and nonlinearities; the presence of complex sound speed and sound attenuation variations can be assessed. Using the forward prediction, we can also characterize (possible) unmodeled effects such as bubble fields and suspended sediments.

V. Apply of PFFT-BEM direct simulations to reverberation problems in

shallow water waveguide

In chapter 4, we have studied the 3D scattering problem from a rough surface extensively. The next step is to conduct 3D direct numerical of reverberation problems in shallow water waveguide. Getting a rigorous numerical solution would be a major effort since it would need to work with realizations of the roughness surface/bottom, requiring averaging over many roughness realizations. The developed PFFT-BEM method can accomplish this task efficiently. To account for the time dependence of the reverberation, we need to cover the frequency band within the pulse with many continuous wave runs and then using Fourier transform to get the time domain results. These results are important as they would show how well the simplified models used in reverberation modeling actually perform.

Bibliography

J. R. Apel, M. Badiey, C. S. Chiu, S. Finette, R. H. Headrick, J. Kemp, J. F. Lynch, A. E. Newhall, M. H. Orr, B. H. Pasewark, and D. Tielbuerger. An overview of the 1995 SWARM shallow-water internal wave acoustic scattering experiment. *IEEE J. oceanic. Eng.*, 22.3:465–500, 1997.

G. A. Athanassoulis and A. M. Prospathopoulos. Three-dimensional acoustic scattering of a source generated field from a cylindrical island. *J. Acoust. Soc. Am.*, 100.1:206–218, 1996.

O. Axelsson. *Iterative solution methods.* Cambridge university press, 1996.

M. Badiey, B. G. Katsnelson, J. F. Lynch, S. Pereselkov, and W. L. Siegmann. Measurement and modeling of three-dimensional sound intensity variations due to shallow-water internal waves. *J. Acoust. Soc. Am.*, 117.2:613–625, 2005.

S. Balay, S. Abhyankar, M. Adams, J. Brown, P. Brune, K. Buschelman, L. D. Dalcin, V. Eijkhout, W. Gropp, D. Kaushik, and W. S. Knepley. Petsc users manual revision 3.8., 2017. Argonne National Lab, Argonne, IL, United States.

M. S. Ballard. Modeling three-dimensional propagation in a continental shelf environment. *J. Acoust. Soc. Am.*, 131.3:1969–1977, 2012.

M. S. Ballard, B. M. Goldsberry, and M. J. Isakson. Normal mode analysis of three-dimensional propagation over a small-slope cosine shaped hill. *J. Comput. Acoust.*, 23.03:1550005, 2015.

A. Bottero, P. Cristini, D. Komatitsch, and M. Asch. An axisymmetric time-domain spectral-element method for full-wave simulations: Application to ocean acoustics. *J. Acoust. Soc. Am.*, 140.5:3520–3530, 2016.

A. J. Burton and G. F. Miller. The application of integral equation methods to the numerical solution of some exterior boundary-value problems. *Proc. Royal Soc. London A*, 323:201–210, 1971.

K. E. Chen. On a class of preconditioning methods for dense linear systems from boundary elements. *SIAM J. Sci. Comput*, 20.2:856–869, 1998.

M. D. Collins and R. B. Evans. A two-way parabolic equation for acoustic backscattering in the ocean. *J. Acoust. Soc. Am.*, 91.3:1357–1368, 1992.

M. D. Collins, B. E. McDonald, K. D. Heaney, and W. A. Kuperman. Three-dimensional effects in global acoustics. *J. Acoust. Soc. Am.*, 93.3:1567–1575, 1995.

P. Cristini and D. Komatitsch. Some illustrative examples of the use of a spectral-element method in ocean acoustics. *J. Acoust. Soc. Am.*, 131.3:EL229–EL235, 2012.

G. B. Deane and M. J. Buckingham. An analysis of the three-dimensional sound field in a penetrable wedge with a stratified fluid or elastic basement. *J. Acoust. Soc. Am.*, 93.3:1319–1328, 1993.

T. F. Duda. Modeling and forecasting ocean acoustic conditions. *Journal of Marine Research*, 75.3:435–457, 2017.

B. D. Dushaw and J. A. Colosi. Ray tracing for ocean acoustic tomography. No. APL-UW-TM-3-98, Washington Univ. Seattle Applied Phys. Lab, 1998.

L. Godinho, A. Tadeu, and F. J. F. G. Branco. 3D acoustic scattering from an irregular fluid waveguide via the BEM. *Eng. Anal. Boundary Element*, 25.3:443–453, 2001.

S. Grilli, T. Pedersen, and P. Stepanishen. A hybrid boundary element method for shallow water acoustic propagation over an irregular bottom. *Eng. Anal. Boundary Element*, 21.2:131–145, 1998.

P. J. Harris and K. Chen. On efficient preconditioners for iterative solution of a Galerkin boundary element equation for the three-dimensional exterior Helmholtz problem. *J. of Comput. and appl. Math.*, 156.2:303–318, 2003.

R. H. Headrick, J. F. Lynch, J. Kemp, A. E. Newhall, K. Von der Heydt, J. R. Apel, M. Badiey, C. S. Chiu, S. Finette, M. Orr, and B. Pasewark. Acoustic normal mode fluctuation statistics in the 1995 SWARM internal wave scattering experiment. *J. Acoust. Soc. Am.*, 107.1:201–220, 2000.

M. J. Isakson, R. Yarbrough, and N. Chotiros. A finite element model for seafloor roughness scattering. *Proc. of Inter. Symp. on Underwater Reverberation and Clutter. Italy: NURC, La Spezia*, 2008.

M.J. Isakson, B. Goldsberry, and N.P. Chotiros. A three-dimensional, longitudinally-invariant finite element model for acoustic propagation in shallow water waveguides. *J. Acoust. Soc. Am.*, 136.3:EL206–EL211, 2014.

F.B. Jensen, W.A. Kuperman, M.B. Porter, and H. Schmidt. *Computational Ocean Acoustics*. Springer Science and Business Media, 2011.

R. M. Jones, J. P. Riley, and T. M. Georges. HARPO-A versatile three-dimensional hamiltonian ray-tracing program for acoustic waves in an ocean with irregular bottom. Technical report, NOAA, 1986.

S. M. Joshia and M. J. Isakson. Backscattering from a pressure-release rough surface. *J. Acoust. Soc. Am.*, 129.4:2630, 2011.

P. J. Kaczkowski and E. I. Thorsos. Application of the operator expansion method to scattering from one dimensional moderately rough dirichlet random surfaces. *J. Acoust. Soc. Am.*, 96.2:957–972, 1994.

S. Keuchel, K. Vater, and O. V. Estorff. hp fast multipole boundary element method for 3D acoustics. *Int. J. for Numer. Meth. in Eng.*, 110.9:842–861, 2017.

W. A. Kuperman and J. F. Lynch. Shallow-water acoustics. *Physics Today*, 57.10: 55–61, 2004.

D. Lee, M. H. Schultz, and Y. Saad. A three-dimensional wide angle wave equation with vertical density variations. *Computational Acoustics: Ocean-Acoustic Models and Supercomputing*, pages 143–154, 1990.

D. Lee, G. Botseas, and W. L. Siegmann. Examination of three-dimensional effects using a propagation model with azimuth coupling capability (FOR3D). *J. Acoust. Soc. Am.*, 91.6:3192–3202, 1992.

C. Li and Y. Liu. Fully-nonlinear simulation of the hydrodynamics of a floating body in surface waves by a high-order boundary element method. *Proc. of ASME 2015 34th International Conference on Ocean, Offshore and Arctic Engineering*, pages V009T09A001–V009T09A001, 2015.

C. Li and Y. Liu. On the weakly nonlinear seakeeping solution near the critical frequency. *J. Fluid Mech.*, 846:999–1022, 2018.

J. Li, W. Chen, and Z. Fu. A modified dual-level algorithm for large-scale three-dimensional laplace and Helmholtz equation. *Comput. Mech.*, 10:1–15, 2018.

Y. T. Lin. Three-dimensional shallow water acoustics. *Woods Hole Oceanographic Institution Woods Hole United States*, 2016.

Y. T. Lin and T. F. Duda. A higher-order split-step Fourier parabolic-equation sound propagation solution scheme. *J. Acoust. Soc. Am.*, 132.2:EL61–EL67, 2012.

Y. T. Lin, J. M. Collis, and T. F. Duda. A three-dimensional parabolic equation model of sound propagation using higher-order operator splitting and Padè approximants. *J. Acoust. Soc. Am.*, 132.5:EL364–EL370, 2012.

Y. T. Lin, T. F. Duda, and A. E. Newhall. Three-dimensional sound propagation models using the parabolic-equation approximation and the split-step Fourier method. *J. Comput. Acoust.*, 21.01:1250018, 2013.

J. F. Lingevitch, M. D. Collins, M. J. Mills, and R. B. Evan. A two-way parabolic equation that accounts for multiple scattering. *J. Acoust. Soc. Am.*, 112.2:476–480, 2002.

W. Luo and H. Schmidt. Three-dimensional propagation and scattering around a conical seamount. *J. Acoust. Soc. Am.*, 125.1:52–56, 2009.

J. F. Lynch, Y. T. Lin, T. F. Duda, and A. E. Newhall. Acoustic ducting, reflection, refraction, and dispersion by curved nonlinear internal waves in shallow water. *IEEE Journal of Oceanic Engineering*, 35.1:12–27, 2010.

N. Masters and W. Ye. Fast BEM solution for coupled 3D electrostatic and linear elastic problems. *Eng. Anal. Boundary Element*, 28.9:1175–1186, 2004.

A. Pereira, A. Tadeu, L. Godinho, and J. A. F. Santiago. 2.5D BEM modeling of underwater sound scattering in the presence of a slippage interface separating two flat layered regions. *Wave Motion*, 48.8:676–692, 2010.

J. S. Perkins and R. N. Baer. An approximation to the three-dimensional parabolic equation method for acoustic propagation. *J. Acoust. Soc. Am.*, 72.2:515–522, 1982.

J. R. Phillips and J. K. White. A precorrected-FFT method for electrostatic analysis of complicated 3-D structures. *IEEE Trans. Comput. Aided Des. Integr. Circuits Syst.*, 16.10:1059–1072, 1997.

M. B. Porter and H. P. Bucker. Gaussian beam tracing for computing ocean acoustic fields. *J. Acoust. Soc. Am.*, 82.4:1349–1359, 1987.

M.B. Porter. The Bellhop manual and user guide: Preliminary draft, 2011. Heat, Light, and Sound Research, Inc., Tech. Rep.

W. Qu, W. Chen, and C. Zheng. Diagonal form fast multipole singular boundary method applied to the solution of high frequency acoustic radiation and scattering. *Int. J. Numer. Methods in Eng.*, 111.9:803–815, 2017.

B. D. Reeder. Field observation of low-to-mid-frequency acoustic propagation characteristics of an estuarine salt wedge. *J. Acoust. Soc. Am.*, 139.1:21–29, 2016.

S.P. Robinson, P.A. Lepper, and R.A. Haxelwood. Good practice guide for underwater noise measurement, 2014. NPL Good Practice Guide.

Y. Saad and M. H. Schultz. A generalized minimal residual algorithm for solving nonsymmetric linear systems. *SIAM J. Sci. Comput*, 7.3:856–869, 1986.

J. A. F. Santiago and L. C. Wrobel. A boundary element model for underwater acoustics in shallow water. *Comput. Model. Eng. Sci.*, 1.3:73–80, 2000.

H. Schmidt. Safari: Seismo-Acoustic Fast Field Algorithm for Range-Independent environments. User's Guide (No. SACLANTCEN-SR-113), 1988. SACLANT Undersea Research Centre, La Spezia, Italy.

C. R. Sherwood and J. S. Creager. Sedimentary geology of the columbia river estuary. *Progress in Oceanography*, 25:15–79, 1990.

A. A. Shmelev, J. F. Lynch, Y. T. Lin, and H. Schmidt. Three-dimensional coupled mode analysis of internal-wave acoustic ducts. *J. Acoust. Soc. Am.*, 135.5:2497–2512, 2014.

F. Sturm. Numerical study of broadband sound pulse propagation in three-dimensional oceanic waveguides. *J. Acoust. Soc. Am.*, 117.3:1058–1079, 2005.

F. D. Tapperter. *The parabolic approximation method*, pages 224–287. Lecture Notes in Physics. Springer, Berlin, Heidelberg, 1977.

M. I. Taroudakis. A coupled mode formulation for the solution of the Helmholtz equation in water in the presence of a conical seamount. *J. of Comput. Acoust.*, 4.1:101–121, 1996.

J. Thomson, A. R. Horner Devine, S. Zippel, C. Rusch, and W. Geyer. Wave breaking turbulence at the offshore front of the columbia river plume. *Geophysical Research Letters*, 41.4:8987–8993, 2014.

E. I. Thorsos. The validity of the Kirchhoff approximation for rough surface scattering using a Gaussian roughness spectrum. *J. Acoust. Soc. Am.*, 83.1:78–92, 1988.

E. I. Thorsos and S. L. Broschat. An investigation of the small slope approximation for scattering from rough surfaces. Part I. Theory. *J. Acoust. Soc. Am.*, 97.4: 2082–2093, 1995.

E. I. Thorsos and J. R. Darrell. The validity of the perturbation approximation for rough surface scattering using a Gaussian roughness spectrum. *J. Acoust. Soc. Am.*, 86.1:261–277, 1989.

E. I. Thorsos, D. R. Jackson, and K. L. Williams. Modeling of subcritical penetration into sediments due to interface roughness. *J. Acoust. Soc. Am.*, 107.1:263–277, 2000.

J. V. Toporkov, S. A. Ra'id, and G. S. Brown. Issues related to the use of a Gaussian-like incident field for low-grazing-angle scattering. *JOSA A*, 16.1:176–187, 1999.

C. P. Vendhan, G. C. Diwan, and S. K. Bhattacharyya. Finite-element modeling of depth and range dependent acoustic propagation in oceanic waveguides. *J. Acoust. Soc. Am.*, 127.6:3319–3326, 2010.

R. J. Wagner. Shadowing of randomly rough surfaces. *J. Acoust. Soc. Am.*, 41.1: 138–147, 1967.

K. L. Williams, E. I. Thorsos, and W. T. Elam. Examination of coherent surface reflection coefficient (CSRC) approximations in shallow water propagation. *J. Acoust. Soc. Am.*, 16.4:1975–1984, 2004.

T. W. Wu. On computational aspects of the boundary element method for acoustic radiation and scattering in a perfect waveguide. *J. Acoust. Soc. Am.*, 96.6:3733–3743, 1994.

J. Xiao, W. Ye, Y. Cai, and J. Zhang. Precorrected FFT accelerated BEM for large scale transient elastodynamic analysis using frequency domain approach. *Int. J. Numer. Meth Eng.*, 90.1:116–134, 2012.

Z. Xie, R. Matzen, P. Cristini, D. Komatitsch, and R. Martin. A perfectly matched layer for fluid-solid problems: Application to ocean-acoustics simulations with solid ocean bottoms. *J. Acoust. Soc. Am.*, 140.1:165–175, 2016.

C. X. Xu, J. Tang, S. C. Piao, J. Q. Liu, and S. Z. Zhang. Developments of parabolic equation method in the period of 2000-2016. *Chinese Physics B*, 25.12:124315, 2016.

M. Xue, H. Xu, Y. Liu, and D. K. Yue. Computations of fully nonlinear three-dimensional wave wave and wave body interactions. part 1. dynamics of steep three-dimensional waves. *J. Fluid Mech.*, 438:11–39, 2001.

H. Yan and Y. Liu. An efficient high-order boundary element method for nonlinear wave wave and wave body interactions. *J. Comp. Phys.*, 230:402–423, 2011.

Z. Yan and X. Gao. The development of the pFFT accelerated BEM for 3-D acoustic scattering problems based on the burton and miller's integral formulation. *Eng. Anal. Boundary Element*, 37.2:409–418, 2013.

Z. Y. Yan, J. Zhang, and W. Ye. Rapid solution of 3-D oscillatory elastodynamics using the pFFT accelerated BEM. *Eng. Anal. Boundary Element*, 34.11:956–962, 2010a.

Z. Y. Yan, J. Zhangand W. Ye, and T. X. Yu. Numerical characterization of porous solids and performance evaluation of theoretical models via the precorrected-FFT accelerated BEM. *Computer Modeling in Engineering and Sciences (CMES)*, 55.1: 33, 2010b.

D. Zhu and L. B Bjørnø. A three-dimensional, two-way, parabolic equation model for acoustic backscattering in a cylindrical coordinate system. *J. Acoust. Soc. Am.*, 108.3:889–898, 2000.